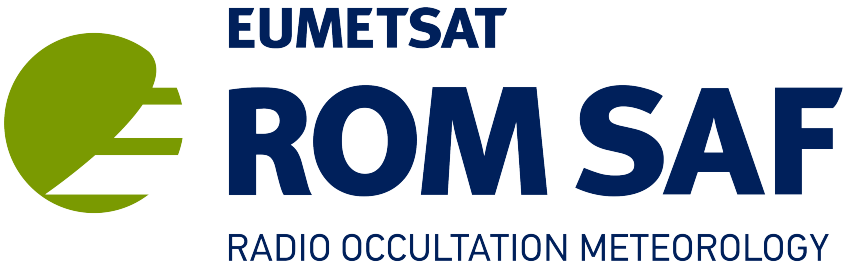

ROM SAF CDOP-3

Visiting Scientist Report 35:

Integration and initial application of ROPP in the Wegener Center reference occultation processing system rOPS

Marc Schwärz

ROM SAF Consortium
Danish Meteorological Institute (DMI)
European Centre for Medium-Range Weather Forecasts (ECMWF)
Institut d'Estudis Espacials de Catalunya (IEEC)
Met Office (UKMO)

Ref: SAF/ROM/DMI/REP/VS/35
Version: 1.1
Date: 10 December 2019

DOCUMENT AUTHOR TABLE

	Author(s)	*Function*	*Date*
Prepared by:	Marc Schwärz	ROM SAF Visiting Scientist	06/12/2019
Reviewed by (Internal):	Johannes K. Nielsen	ROM SAF Project Team	06/12/2019
Approved by:	Sean Healy	ROM SAF Science Coordinator	06/12/2019
Approved by:	Kent B. Lauritsen	ROM SAF Project Manager	10/12/2019

DOCUMENT CHANGE RECORD

Version	*Date*	*By*	*Description*
Version 1.0	6 December 2019	MAS	Final version
Version 1.1	10 December 2019	MAS	Including additional comments from Johannes Nielsen, Sean Healy and Kent Lauritsen

DOCUMENT DISTRIBUTION LIST

This VS report is made available at the ROM SAF website

VS AUTHOR AND DURATION

VS Author
This VS study was carried out by Dr. Marc Schwärz, Wegener Center for Climate and Global Change (WEGC), University of Graz, Graz, Austria
email: marc.schwaerz@uni-graz.at

VS Duration
This VS study was performed during October 2018 to October 2019 at the Wegener Center, University of Graz

ROM SAF

The Radio Occultation Meteorology Satellite Application Facility (ROM SAF) is a decentralised processing center under EUMETSAT which is responsible for operational processing of GRAS radio occultation (RO) data from the Metop satellites and radio occultation data from other missions. The ROM SAF delivers bending angle, refractivity, temperature, pressure, humidity, and other geophysical variables in near real-time for NWP users, as well as reprocessed Climate Data Records (CDRs) and Interim Climate Data Records (ICDRs) for users requiring a higher degree of homogeneity of the RO data sets. The CDRs and ICDRs are further processed into globally gridded monthly-mean data for use in climate monitoring and climate science applications.

The ROM SAF also maintains the Radio Occultation Processing Package (ROPP) which contains software modules that aid users wishing to process, quality-control and assimilate radio occultation data from any radio occultation mission into NWP and other models.

The ROM SAF Leading Entity is the Danish Meteorological Institute (DMI), with Cooperating Entities: i) European Centre for Medium-Range Weather Forecasts (ECMWF) in Reading, United Kingdom, ii) Institut D'Estudis Espacials de Catalunya (IEEC) in Barcelona, Spain, and iii) Met Office in Exeter, United Kingdom. To get access to our products or to read more about the ROM SAF please go to: `http://www.romsaf.org`.

Intellectual Property Rights

All intellectual property rights of the ROM SAF products belong to EUMETSAT. The use of these products is granted to every interested user, free of charge. If you wish to use these products, EUMETSAT's copyright credit must be shown by displaying the words "copyright (year) EUMETSAT" on each of the products used.

List of Contents

Document Change Record 2

Executive Summary 5

1 Introduction 6

2 Description of the datasets 7
2.1 Radio occultation datasets . . . 7
2.2 The radio occultation technique . . . 7
2.2.1 OPSv5.6 RO data . . . 8
2.2.2 GPACv2.3.0 RO data . . . 9
2.3 ECMWF Data . . . 10

3 General validation setup 12
3.1 Collocation between ”Candidate” and ”Reference” profiles . . . 12
3.2 Interpolation to a common vertical grid . . . 12
3.3 Data smoothing for matching data resolution . . . 12

4 Validation Analysis 13
4.1 Refractivity . . . 13
4.2 Dry Temperature . . . 16
4.3 Temperature . . . 18
4.4 Pressure . . . 20
4.5 Specific Humidity . . . 22

5 Summary and Conclusions 23
Acronyms and abbreviations . . . 25

Reference Documents 30

A Median and Mean only – Zoom 30

B Median, Mean, and 10% and 90% Percentiles 50

Executive summary

The WEGC and the ROM SAF are embarking on a closer collaboration through the Federate Activity "ATROMSAF1-FA05" [RD.24], with the overall purpose to improve the ROM SAF data processing and especially its embedded error characterization. The present VS was carried out to support this joint effort.

In the next reprocessing the ROM SAF is planning to use ERA5 data, both as background data for Level 2B products and as validation reference data for Level 1, 2 and 3 products. Since ECMWF and ERA5 users had found that the stratospheric temperatures of ERA5 appear to be biased when compared to ERA-Interim and radiosonde observations, a further analysis of this topic using radio occultation observations was found to be useful.

Along these lines, this study contained an assessment of biases of ERA5 (forecast and analysis), ERA-Interim (analysis) and ECMWF operational data (analysis), and it assessed the potential impact on ROM SAF level 2B offline products. The bias assessment focused on seasonal and latitudinal dependence of biases in ERA5 analysis and forecasts, ERA-Interim, and ECMWF operational analysis datasets.

Key results include the following: In the troposphere it was found that ERA5 (forecast and analysis) perform better than ERA-Interim, compared to two radio occultation datasets (ROM SAF's GPACv2.3.0/CDR v1.0 and WEGC's OPSv5.6) used as reference. At 18 km they both exhibit essentially the same negative bias but, compared to the observational datasets, ERA-Interim handled the stratospheric region better. An interesting finding was that within a large part of the compared height range the ERA5 short-range forecast data exhibited a somewhat smaller bias against the observations than the ERA5 analysis.

The results of this study suggest that the use of the ERA5 forecast data as background for future 1D-Var products of the GPAC/ROPP datasets is approriate. In the relevant parameters (temperature, specific humidity, and pressure) and the relevant tropospheric height range (0 km to 15 km), respectively, it exhibited a better performance than the ERA-Interim analysis (currently ERA-Interim forecast data are used as background dataset for the GPAC/ROPP 1D-Var process in the ROM SAF CDR v1.0).

The suggested changes in the background data setup in combination with changes in the setup of the background covariance matrices will likely lead to an improved tropospheric product within a new GPAC reprocessing dataset. The "ATROMSAF1-FA05" project found promising results in a preliminary study using dynamic background and measurement error covariance matrices, which are included in the ATROMSAF1-FA05 Final Report [RD.35].

1 Introduction

The ROM SAF is planning the use of ERA5 data, both as background data for Level 2B products and as validation reference data for Level 1, 2 and 3 products. This may be more challenging than originally expected, because ECMWF has found that the stratospheric temperatures of ERA5 appear to be somewhat biased when compared to ERA-Interim and radiosonde observations [RD.36]. Therefore this study carries out an assessment of biases of ERA5, ERA-Interim and ECMWF operational data (the two re-analyses and the operational analysis), relative to radio occultation (RO) data, and it assesses the potential impact on ROM SAF level 2B offline products.

The bias assessment focuses on seasonal and latitudinal dependence of biases in ERA5 short-range forecasts and suggest mitigations to be used in ROM SAF offline products. It includes also comparisons with ERA5 analysis, and plots showing relation to ERA-Interim and ECMWF operational analysis. This part of the VS project is an application of ROM SAF's GPAC RO dataset at the WEGC, jointly with the WEGC's OPSv5.6 RO dataset, by which the ROM SAF can benefit from research and development at the WEGC.

Chapter 2 describes the datasets which are inter-compared. In a first part it provides an overview of the RO processing and the differences between OPSv5.6 and GPACv2.3.0/CDR v1.0 (both notations refer to the same dataset), the two RO datasets. The second part focuses on the description of the analysis and reanalysis data. It characterizes the resolution of the model fields utilized in this study as well as the implemented interpolation algorithm. In addition, the main differences between the three model datasets (ERA5, ERA-Interim, ECMWF operational) are outlined.

In chapter 3 the key settings of the validation framework set up at the WEGC are described and chapter 4 provides a thorough presentation of the validation analysis. Finally, chapter 5 gives a summary of this report and provides the main conclusions of the validation study. In the Appendix the details of the comparison analysis are illustrated.

2 Description of the datasets

In this chapter I describe the different datasets used in this comparison study. Different analysis datasets of ECMWF (European Centre for Medium-Range Weather Forecasts) (ECMWF operational analysis, ERA-Interim analysis, and ERA5 analysis and forecast) as well as two RO datasets (OPSv5.6 and GPACv2.3.0) are compared.

2.1 Radio occultation datasets

Even though the RO technique itself is self-calibrating, different data processing schemes yield differences in atmospheric RO data products, which cannot be neglected [RD.2, RD.43, RD.25, RD.16, RD.41, RD.42]. In addition, differences in retrieved products can still result from different datasets used as input data. This is not the case for the data used in this study. Both centers, WEGC and GPAC, use calibrated phase and orbit data from UCAR/CDAAC (University Corporation for Atmospheric Research/COSMIC Data Analysis and Archive Center) for all three satellite missions (FORMOSAT-3/COSMIC, GRACE, and METOP) in the current retrieval version.

2.2 The radio occultation technique

The essential quantity measured by the GNSS RO technique is the change in the phase (and the amplitude) of the signal received at a LEO (low-earth-orbit) satellite. The measured phase change varies as a function of the optical depth of the atmosphere and the movements of both, transmitter and receiver satellite. The relevant phase changes are measured on all transmitted GNSS frequencies (currently: GPS frequencies f_1 = 1575.42 MHz and f_2 = 1227.60 MHz). The heart of the RO measurement system are highly accurate atomic clocks. Depending on the quality of these clocks aboard the LEO satellite, so called ”differencing” techniques have to be applied to correct clock errors. METOP and GRACE have ultra-stable oscillators, i. e. no differencing (zero differencing) is performed. In case of the FORMOSAT-3/COSMIC satellites whose clocks are not that accurate we have to apply the single differencing technique to account for clock errors (c. f. [RD.45, RD.33, RD.32, RD.3]). GNSS transmitter clock errors are estimated by geodetic processing systems.

The next step of the RO retrieval is the calculation of the Doppler shift (the time derivative of the phase) [RD.26, RD.22]. Removing the kinematic contribution to the Doppler shift, i.e., contributions due to the relative motion between GNSS and LEO satellite yields the excess Doppler shift. Together with the precise orbit information (positions and velocities) of both, GNSS and LEO satellite, this enables the calculation of the geometric optics (GO) bending angle α as a function of impact parameter a. The only approximation used in this step is the assumption of local shperical symmetry which is valid after the correction of the oblateness of the Earth. In the lower troposphere the GO approximation collapses. Multipath and diffraction effects become important due to an increase of humidity. In this atmospheric region wave optics (WO) methods have to be applied to derive atmospheric bending angle information [RD.12, RD.18, RD.19, RD.13, RD.40]. To remove the ionospheric contribution of the measured signal the dual-frequency GNSS signal is differenced typically at bending angle level [RD.44, RD.17]. The resulting ionosphere-corrected bending angle represents the cumulative signal due to atmospheric density gradients.

The next step in the RO retrieval chain is the calculation of the refractivity which is performed by applying the Abel transformation [RD.10] on the atmospheric bending angle. Due to the fact that the signal-to-noise ratio of the bending angle decreases with increasing altitude (above about 50 km, depending on the thermal noise of the receiver) the bending angle has to be stabilized at high altitudes. This is achieved by performing an initialization of the bending angle with background information.

Atmospheric refractivity at microwave wavelengths depends on conditions of the dry atmosphere, the moist atmosphere, the ionosphere, and on atmospheric scattering from liquid water or ice crystals. To first order this relationship is provided by the Smith Weintraub formula [RD.38]. In atmospheric regions where moisture is negligible, which holds true for altitudes above 8 km (polar winter) and 14 km (tropics) [RD.11, RD.29], refractivity at microwave wavelengths mainly depends on the density of dry air. The profile of air density in these atmospheric regions can therefore be directly derived from the refractivity profile. Under the assumption of hydrostatic equilibrium, the atmospheric pressure can be derived utilizing the hydrostatic equation and temperature can be approximated using the equation of state for dry air conditions.

Below regions of negligible humidity, i. e. below 8 km (polar winter) and 14 km (tropics), the retrieval of (physical) atmospheric parameter like temperature and humidity requires the usage of background information in order to resolve the wet-dry ambiguity information inherent in refractivity (see e. g., [RD.21, RD.14, RD.20]).

The following two subsections provide an overview on the implementation details for the two RO datasets used in this study. A profound summary of it is provided in [RD.42].

2.2.1 OPSv5.6 RO data

As mentioned above OPSv5.6 data processing uses UCAR/CDAAC orbit and phase data as input. A detailed description of the retrieval steps as well as the quality of the data is provided in [RD.34, RD.1].

Above 7 km to 13 km a geometric optics bending angle retrieval is performed. In the troposphere a CT2 (canonical transformation version 2) (c. f. [RD.13]) is utilized. Both bending angle retrievals are merged within a window of 4.5 km width and a variable center height between 7 km to 13 km. Within this window Gaussian weights were used to get a smooth mixture in the transition from the GO to the WO bending angle. The ionospheric correction is implemented following [RD.44, RD.17]. Below 15 km the ionospheric correction term is extrapolated with a constant low pass filtered L1 - L2 bending angle. The high-pass fraction of the L1 GO bending angle is added again to account for small scale features in the neutral atmosphere.

OPSv5.6 performs a statistical optimization (inverse covariance weighting) of the bending angle above 30 km using operational ECMWF short range forecasts (24 h and 30 h) and on top of it to 120 km MSISE-90. The observation errors are dynamically estimated from the measurement. The observation correlations exhibit an exponential drop off using a correlation length of 1 km. The backround error is set to 15 % of the modeled bending angle. Similar to the observation correlations the model correlations exhibit an exponential drop off but for the model correlations a correlation length of 6 km is used. The Abel integral is im-

plemented following [RD.10] using the statistical optimized bending angle and is performed below 120 km.

The dry air retrieval is implemented using the ideal gas equation i. e., it is assumed that the refractivity is directly proportional to the air density. The hydrostatic integral is initialized at 120 km using MSISE-90 pressure and geopopotential height relative to EGM-96. The dry temperature is obtained using the Smith-Weintraub formula for dry air [RD.38] and the equation of state (ideal gas).

Comparable to the bending angle retrieval the physical parameter retrieval of OPSv5.6 is separated into two parts. Between both parts a sinusoidal transition is performed between 14 km to 16 km. Above 16 km the physical temperature and pressure are calculated using a first order approximation between pressure and dry pressure with fixed background humidity (ECMWF short range forecasts (24 h and 30 h)). Below 14 km the retrieval consists of three steps (c. f. Appendix in [RD.34]):

1. direct retrieval of temperature and pressure using ECMWF short range forecasts for humidity.

2. direct retrieval of humidity and pressure using ECMWF short range forecasts for temperature.

3. statistical optimization of temperature and humidity of step one and two with background temperature and background humidity from ECMWF short range forecasts, background errors from ROPPv6.0 [RD.4], and observational errors following [RD.30]. No error correlations are assumed.

2.2.2 GPACv2.3.0 RO data

The GPACv2.3.0 data used in this study uses UCAR/CDAAC orbit and phase data as input. Detailed description of the data as well as the used software and retrieval algorithms can be found at [RD.28].

Above 25 km a geometric optics bending angle retrieval is performed. Below 20 km a CT2 (canonical transformation version 2) is utilized (c. f. [RD.13]). Between 20 km to 25 km there is a transition from the CT2 bending angle to the geometric optics bending angle. The ionospheric correction is implemented following [RD.44, RD.17]. An extrapolation of the ionospheric corrected bending angle is implemented using a constant L1 - L2 bending angle below a dynamic L2 cutoff height. The transition width is 2 km.

GPACv2.3.0 uses an optimization with dynamic estimation of observation errors [RD.12] and background errors fixed to 50 % of the modled bending angle. The background is based on the BAROCLIM climatology [RD.31]. A best global fit to the data between 40 km to 60 km using a two parameter regression selects the profile from the climatology. No error correlations are assumed. The Abel integral is implemented following [RD.10] using the statistical optimized bending angle and is performed below 150 km.

The dry air retrieval is implemented using the ideal gas equation i. e., it is assumed that the refractivity is directly proportional to the air density. The hydrostatic integral is initialized at 150 km. The upper boundary condition is obtained from the refractivity gradient and

the geopopotential height is relative to EGM-96. The dry temperature is obtained using the Smith-Weintraub formula for dry air [RD.38] and the equation of state (ideal gas).

GPACv2.3.0 data utilizes a 1D-Var algorithm starting from refractivity to perform the moist air retrieval. ERA-Interim forecast data (3 h, 6 h, 9 h, and 12 h) is used as background data. The resulting data is based on the hybrid level grid of ERA-Interim. The state vector contains temperature (on hybrid levels), specific humidity (on hybrid levels), and the surface pressure. The pressure which is compared in the validation analysis in section 4.4 is calculated after [RD.37]. Note that the physical parameters of the GPACv2.3.0 dataset are not merged with the dry parameter data above the troposphere but are used as they are for the full 1D-Var height range.

2.3 ECMWF Data

The datasets used in this study come from three different ECMWF models: ECMWF operational data [RD.7], ERA-Interim data [RD.6, RD.5], and ERA5 data [RD.15, RD.8, RD.9]. From ERA5 analysis and forecast fields are used. For all three models the interpolation strategy to produce the collocated profiles is the same. They are summarized in the following list:

- The interpolation algorithm chooses the time layer of the field which is nearest to the time of the RO event. Using this, the time difference is always smaller or equal to three hours. Four time layer per day are sufficient to sample the diurnal cycle up to the second harmonics (the semi-diurnal variations). Note that for ERA5 6 hourly time layers are used too, although they are available in a 1 hourly temporal resolution. This is done to be comparable to the other models which are used. The forecast are started at the 6 h and 18 h analysis time layer, i. e. 12 h and 18 h forecast fields are used, respectively, to be consistent with the other datasets.

- The spatial interpolation to the geographic location of the event depends on the particular parameter:

  - **temperature**: horizontal: 4-point polynomial (cubic) interpolation adapted by M. E. Gorbunov and A. K. Steiner (for a detailed description c. f. [RD.23]); vertical: natural cubic spline interpolation;

  - **pressure**: horizontal: 4-point polynomial (cubic) interpolation adapted by M. E. Gorbunov and A. K. Steiner (for a detailed description c. f. [RD.23]); vertical: natural cubic spline interpolation; note: the interpolation is performed on the natural logarithm of the values of the particular parameters;

  - **specific humidity**: horizontal: 4-point polynomial (cubic) interpolation adapted by M. E. Gorbunov and A. K. Steiner (for a detailed description c. f. [RD.23]); vertical: linear interpolation;

  - **refractivity**: the refractivity values are calculated out of the interpolated values of interpolated input parameters;

  - **dry density**:the dry density values are retrieved from the interpolated refractivity values under the assumption of the hydrostatic equilibrium;

  - **dry pressure**: dry pressure values are retrieved from the retrieved dry density under the assumption of the hydrostatic equilibrium;
  - **dry temperature**: dry temperature is retrieved from dry pressure and refractivity using the equation of state for dry air conditions;

- The hydrostatic integration to set up the vertical grid of the model fields from the hybrid/model levels was performed using the algorithm described in [RD.37, RD.27].

For all three model fields at a reduced spatial resolution of T42 are used, which corresponds to approximately 300 km. This horizontal resolution is selected to roughly match the natural horizontal resolution of RO profiles, which is approximately 300 km as well. The vertical resolution of the ECMWF operational data is L137 (137 vertical layers; c. f. [RD.6]) which is the same vertical resolution used in ERA5. ERA-Interim used a vertical resolution of L60 [RD.8].

3 General validation setup

In this chapter the key settings used in this validation framework are briefly described.

3.1 Collocation between ”Candidate” and ”Reference” profiles

The collocation procedure for comparing different RO datasets to model fields is relatively simple compared to the validation of different datasets where the crucial thing is to find possible measurements within a limited space time distance from the ”candidate” profile. In the current case an OPSv5.6 and a GPACv2.3.0 profile exhibiting the same occultation ID (i. e. same receiver satellite, same transmitter satellite and same reference time) are selected and the ECMWF fields are interpolated to the space/time location of the RO profile according to the interpolation strategy described in section 2.3.

3.2 Interpolation to a common vertical grid

In order to build the differences between the two profiles of a collocation pair first the data has to be interpolated to a common vertical grid. Depending on the used atmospheric parameter the following interpolation methods were used:

- **temperature**, **dry temperature**, **specific humidity** linear interpolation
- **refractivity**, **pressure**: the logarithm of the atmospheric parameter values is linearly interpolated

3.3 Data smoothing for matching data resolution

To use both the candidate and reference profiles at the same vertical resolution, both are smoothed to the same matching resolution, before computing the validation statistics. For this purpose a Gaussian window of the width w equal to the quadratic difference of the widths of the averaging kernels of the low-resolution data, $w_{\text{low-resolution}}$, and the high-resolution data, $w_{\text{high-resolution}}$, is used based on experience of the remote sensing validation community [RD.39]:

$$w^2 = w^2_{\text{low-resolution}} - w^2_{\text{high-resolution}}. \tag{3.1}$$

Note that for a Gaussian window the FWHM (full width at half maximum) is 2.355σ (with σ as the standard deviation); this is important to implement the Gaussian window properly. Practically speaking, the higher-resolution data are smoothed to the resolution of the lower-resolution data.

According to [RD.22, RD.13] the vertical resolution of RO data is typically about 100 m in the lower troposphere to about 1 km in the stratosphere. [RD.46] claimed that the vertical resolution of RO data is 100 m to 200 m near the tropopause, 500 m in the lower stratosphere at low mid-latitudes and about 1.4 km at 22 km to 27 km altitude. ECMWF level spacing exhibits a vertical resolution of less than 100 m in the lower troposphere and decreases with increasing height (more dens for L137 less for L60; c. f. [RD.6, RD.8]). According to this a mean vertical resolution of 1 km was chosen to smooth the data.

4 Validation Analysis

In this chapter a bias assessment of ERA5 (analysis and forecast), ERA-Interim (analysis), and ECMWF operational data (analysis) with respect to RO data is provided. The bias assessment focuses on seasonal and latitudinal dependence of the systematic differences of the particular datasets among each other.

The structure for all plots in this chapter (Figure 4.1, Figure 4.2, Figure 4.3, Figure 4.4, Figure 4.5) is the same: The top left panel provides the results for January 2014, the top right panel those for April 2014, in the bottom left panel July 2014, and in the bottom right panel October 2014 is shown. This was done to illustrate an overview on the seasonal dependency of the behavior of the biases between the different data sets. The solid lines show the median systematic difference and the dashed lines the mean systematic difference. The red lines show the differences between GPACv2.3.0 and OPSv5.6, the blue line the differences between the operational analysis of ECMWF and OPSv5.6, the green line the differences between ERA-Interim analysis and OPSv5.6, the black line the differences between ERA5 analysis and OPSv5.6, and the dark yellow line the differences between ERA5 forecasts and OPSv5.6. The plots are separated into two parts: The left part exhibits the number of collocated events and the right part the systematic differences.

In the appendix a detailed evaluation which performs a separation into 5 latitude bands – northern hemisphere polar (60°N to 90°N), northern hemisphere mid-latitudes and subtropics (20°N to 60°N), tropics (20°S to 20°N), southern hemisphere mid-latitudes and subtropics (20°S to 60°S), and southern hemisphere polar (60°S to 90°S) – is provided (Appendix A: zoomed plots showing the results between ±1 %; Appendix B: plots also show the 10 % and 90 % percentiles).

4.1 Refractivity

Figure 4.1 shows the global validation results for refractivity. All four months exhibit a very good agreement of the two observational datasets (GPACv2.3.0 and OPSv5.6) up to 40 km. Above this height they start to differ which is a result of of the background models used in the upper air initialization [RD.42, RD.35]. Smaller differences up to about 0.05 % occur in the upper troposphere and at a height of about 17 km to 18 km. The differences in the upper troposphere are rather consistent within all months and latitude bands (except for the tropics where the two datasets seem to be more consistent). The differences around 17 km to 18 km are highest in the tropics within all months. In all other latitude regions GPACv2.3.0 and OPSv5.6 agree well in this height range – if there is a difference then it mainly occurs in the mean but not in the median (c. f. Figure A.1, Figure A.6, Figure A.11, Figure A.16).

The model datasets exhibit larger differences compared to the two observational datasets. Between 12 km and 18 km the bias increases up to 0.25 % and decreases back to about 0.0 % reaching 21 km. In the global view this bias is quite consistent for all seasons/months. It is largest for ERA-Interim and smaller for ERA5 (analysis and forecast) and the operational analysis of ECMWF.

Above about 21 km the model datasets start to differ. ERA-Interim exhibits the best consistency compared to the observational datasets. In January the bias is almost 0.0 % up to 31 km and does not exceed -0.1 % to -0.15 % up to 40 km. In 50 km it exceeds 0.5 % in

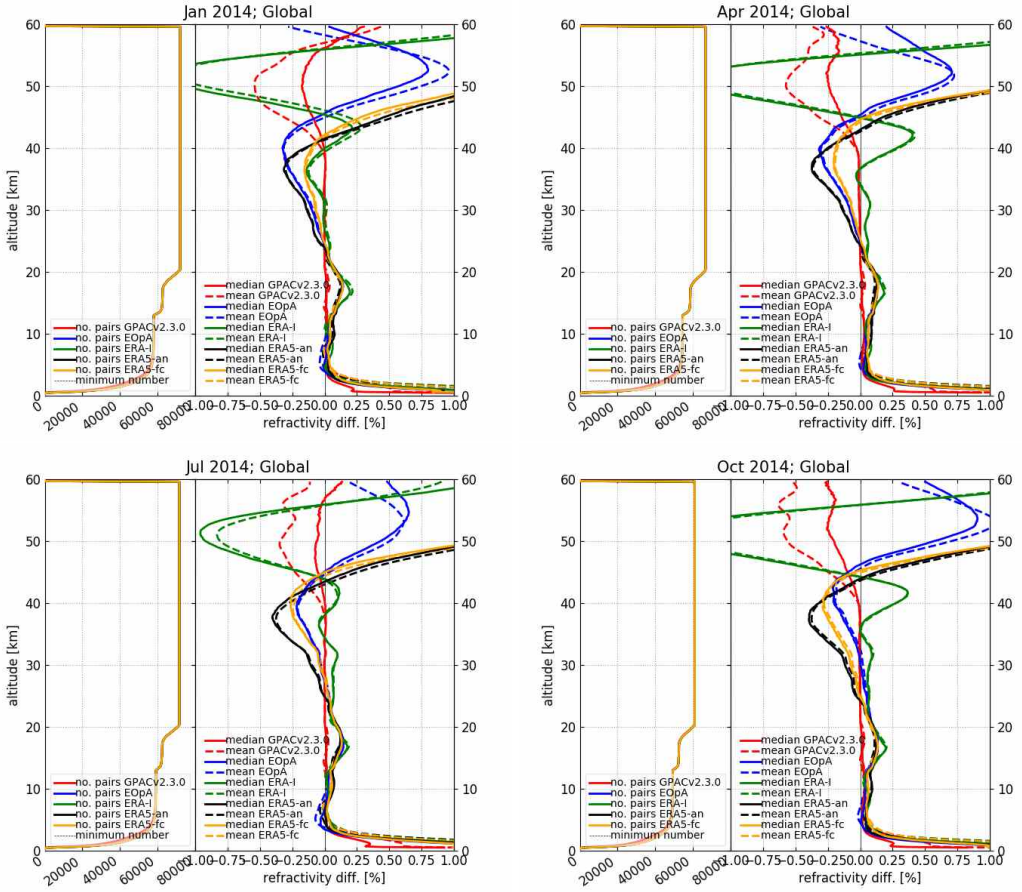

Figure 4.1: *Globally sampled refractivity comparison for January, April, July, and October 2014.*

all months and latitude bands except for July. Compared to ERA-Interim ERA5 analysis and the operational data of ECMWF are more consistent with one another but less consistent with the observational data sets. Up to 40 km the ERA5 forecast lies between the results of ERA-Interim and those of the ERA5 and operational analysis data (in January and April). The operational analysis exhibits an increasing negative bias starting at about 25 km which reaches -0.25 % at about 40 km. In July and October this bias is a little bit smaller. Above that the bias becomes positive reaching 0.75 % at about 50 km – smaller in July and larger in October. In January the ERA5 analysis is smaller than the operational analysis reaching -0.1 % to -0.15 % at about 38 km. In April, July, and October these biases are a little bit larger – largest in October reaching 0.25 %. Above 45 km the ERA5 analysis strongly starts to increase exceeding 1 % at 50 km. The ERA5 forecast dataset also exhibits an increasing negative bias reaching its maximum (0.15 % in January, 0.2 % in April and >=0.25 % in July and October) between 38 km and 40 km. This bias is smaller than the bias for the ERA5 analysis and the operational data of ECMWF in January and April and lies between the ERA5 analysis and the operational data in July and October. Note that in this height region the ERA5 forecast data always exhibits a smaller bias than the ERA5 analysis compared to the observational datasets.

The zonal separation of the validation is shown in the appendix (c. f. Figure A.1, Figure A.6, Figure A.11, Figure A.16). We can see that the larger bias of ERA-Interim at about 18 km

arises mainly from the tropics and to smaller parts from the mid-latitude subtropical regions which seem to contain parts of the events exhibiting the tropical structure. ERA5 (analysis and forecast) as well as the operational analysis of ECMWF are in a quite good agreement with the observational datasets in the tropics up to about 20 km. The polar regions exhibit a bulk offset of all three analysis datasets as well as the forecast dataset of about 0.2 % between 12 km to 25 km. An exception is ERA-Interim in the southern polar region where it matches the observations quite well. Above that the ERA-Interim analysis on the one hand and the ERA5 and the operational analysis at the other hand start to show the same features as described in the global view.

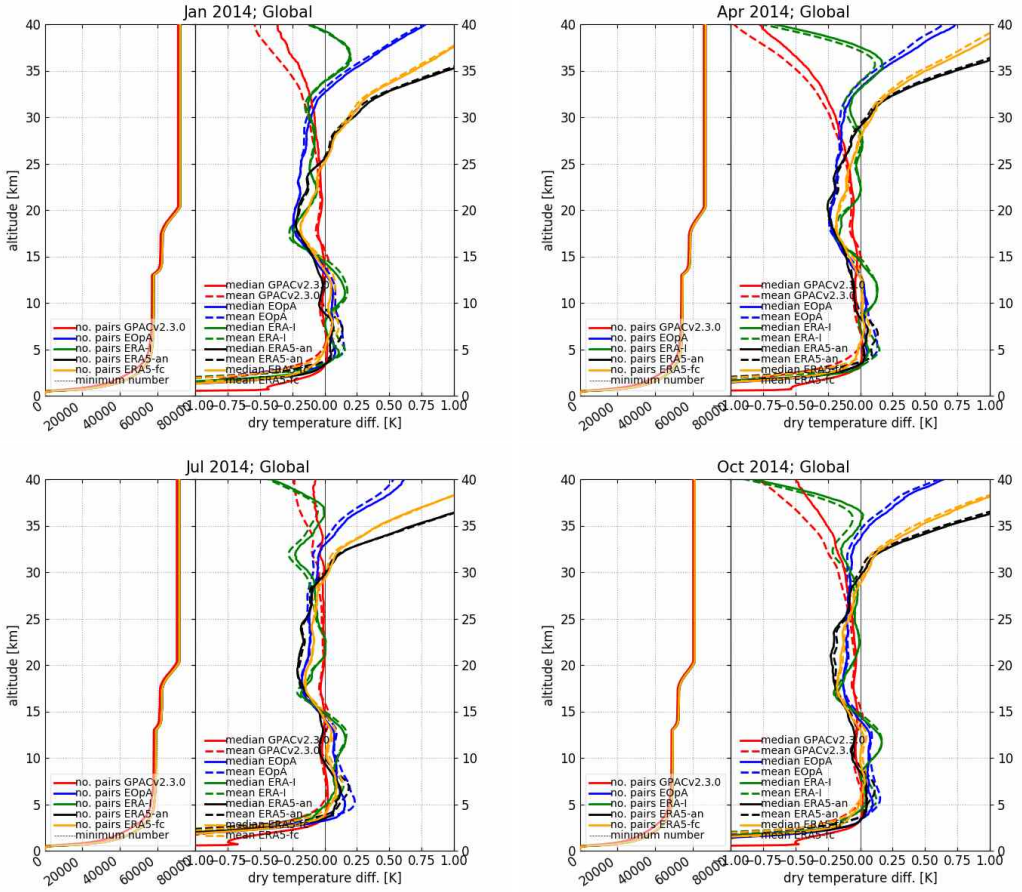

Figure 4.2: *Globally sampled dry temperature comparison for January, April, July, and October 2014.*

4.2 Dry Temperature

Figure 4.2 shows the global validation results for dry temperature. Comparable to the refractivity results all four months exhibit a very good agreement of the two observational datasets (GPACv2.3.0 and OPSv5.6) above about 3 km to 4 km. But in contrast to the refractivity this consistency reach up to about 25 km to 30 km (due to hydrostatic integral). At about 27 km the difference in dry temperature exceeds -0.1 K and reaches 0.25 K at about 35 km. This is true for January, April and October. In July the bias of the median stays within about 0.1 K up to 40 km which is comparable to the refractivity results where the consistency between the two observational data sets reaches up to 55 km.

As can be seen in the validation results of refractivity the model datasets exhibit larger differences compared to the two observational datasets. In the global view ERA-Interim and the operational analysis show an offset of about 0.1 K to 0.15 K at 4.5 km in January which is not present in April and October. In July only the operational analysis shows this offset. This feature cannot be seen in the ERA5 analysis. Between 6 km to 13 km ERA5 and the operational analysis have a more or less constant bias of 0.1 K throughout all months. On the other hand ERA-Interim exhibits a changing bias between 0 K and 0.2 K in this height range which is largest at about 12 km to 13 km. This feature can be seen more or less distinct in all months. Between 5 km to 13 km the ERA5 forecast dataset exhibits a slightly changing bias

of about 0.05 K in January and July. In April and October ERA5 forecast data shows almost no bias against the observational datasets.

An additional stronger bias of about -0.25 K can be found at 18 km for all three analysis datasets. The ERA5 forecast data shows this bias too, but not that distinct. Above this height the operational analysis keeps this (slightly decreasing) negative bias up to about 30 km to 35 km and then starts to exhibit an increasing positive bias above, reaching 0.5 K to 0.75 k at 40 km. ERA-Interim sticks a little bit closer to the observational datasets between 20 km and 30 km. Above 18 km the ERA5 analysis exhibits a decreasing negative bias up to 25 km and then builds up an increasing positive offset compared to the observations which exceeds 1 K between 35 km and 40 km. The ERA5 forecast dataset shows a smaller negative bias than the ERA5 analysis data between above 18 km up to about 25 km to 30 km. Above about 30 km (25 km in January) the sign of the bias changes. Above that height the bias of ERA5 forecast data is smaller or equal than the bias of ERA5 analysis data.

The zonal separation of the dry temperature validation is shown in the appendix (c. f. Figure A.2, Figure A.7, Figure A.12, Figure A.17). We can see that the very prominent negative bias at 18 km which is most distinct in ERA-Interim comes mostly from contributions from the tropics. In addition the offset of the model datasets at about 5 km can also be found most prominently in the tropics. On a closer examination we can see that ERA5 sticks best to the observational datasets in this height range. The ERA5 forecast dataset does not show any particular abnormalities compared to the global view.

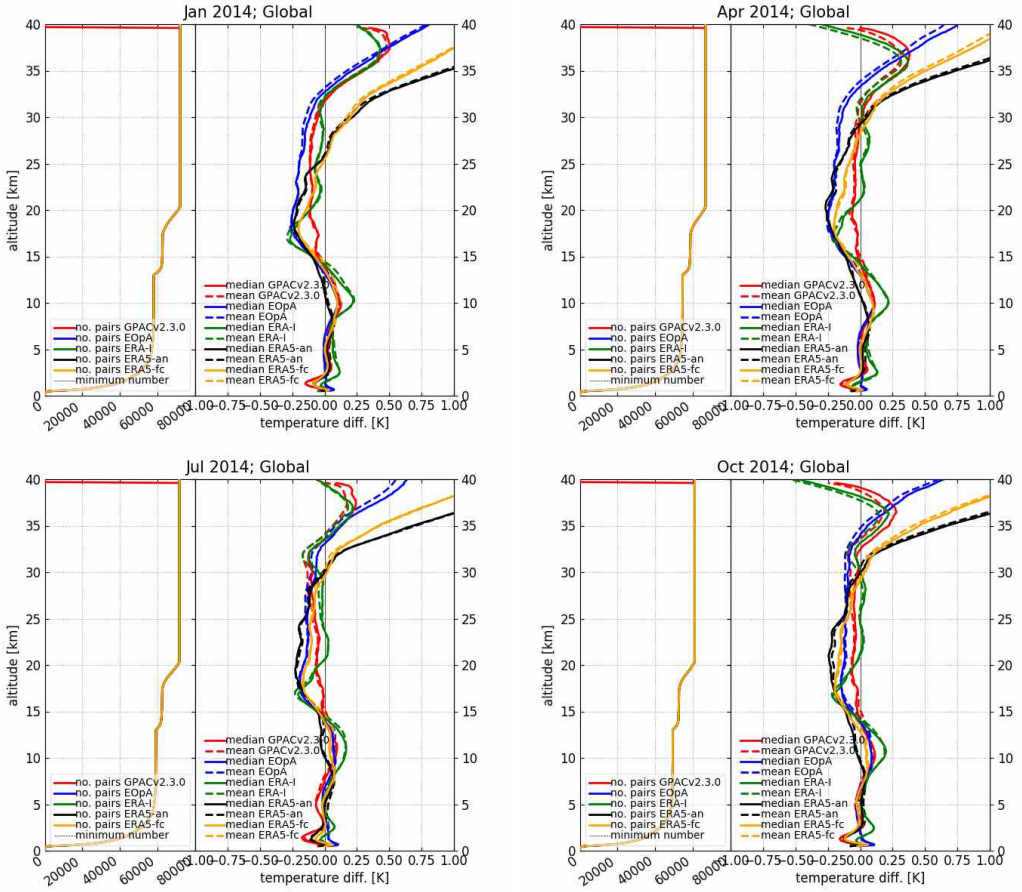

Figure 4.3: *Globally sampled temperature comparison for January, April, July, and October 2014.*

4.3 Temperature

Figure 4.3 shows the global validation results for temperature. As mentioned in the data description part (c. f. subsection 2.2.2) GPACv2.3.0 temperature (like pressure and specific humidity) is not a pure measurement product but contains background data from short term ERA-Interim forecasts in the whole height range which is shown. On the other hand OPSv5.6 performs a merge with the dry parameters (dry temperature and dry pressure) between 14 km to 16 km. Above 16 km OPSv5.6 is more or less equal to the dry parameter results (apart from a small dry-to-moist offset which is always smaller than 0.02 K).

This results in a larger offset between the two measurement datasets. In the lowest part of the troposphere (lowest 2 km) GPACv2.3.0 exhibits a negative systematic difference of about 0.2 K compared to OPSv5.6 throughout all month. Above that up to about 30 km both observational datasets are equal within an uncertainty range of about ±0.1 K except at about 10 km for all months and in January where this is exceeded a little bit. Above 30 km GPACv2.3.0 temperature follows more or less the temperature of ERA-Interim.

Regarding the results of the model dataset it can be said that above about 15 km the structure of the validation results for temperature against OPSv5.6 are comparable to the results of dry temperature. Below that height the results differ. In general it can be said that between 3 km to 15 km GPACv2.3.0, the operational analysis, the ERA5 analysis, and the ERA5 forecasts

agree quite well (within about ±0.1 K). In contrast to that ERA-Interim exhibits larger offsets – 0.1 K to 0.15 K compared to the other analysis datasets and almost 0.25 K compared to OPSv5.6 at about 10 km. Between 3 km to 7 km the operational analysis is rather similar to OPSv5.6 (OPSv5.6 uses operational forecasts as background data for its moist air retrieval).

The zonal separation of the temperature validation is shown in the appendix (c. f. Figure A.3, Figure A.8, Figure A.13, Figure A.18). Like in the global view the results between temperature and dry temperature are comparable above about 15 km. An interesting aspect is that in the polar summer bin (60°S to 90°S in January and 60°N to 90°N in July) GPACv2.3.0 follows the ERA-Interim results quite strongly. The same thing is true in the tropics in January below 15 km. In April, July, and October GPACv2.3.0 does not fully follow the ERA-Interim results – the bias of ERA-Interim compared to OPSv5.6 and also to ERA5 and the operational analysis is too large to be removed by the 1D-Var process. The ERA5 forecast dataset does not show any particular abnormalities compared to the global view.

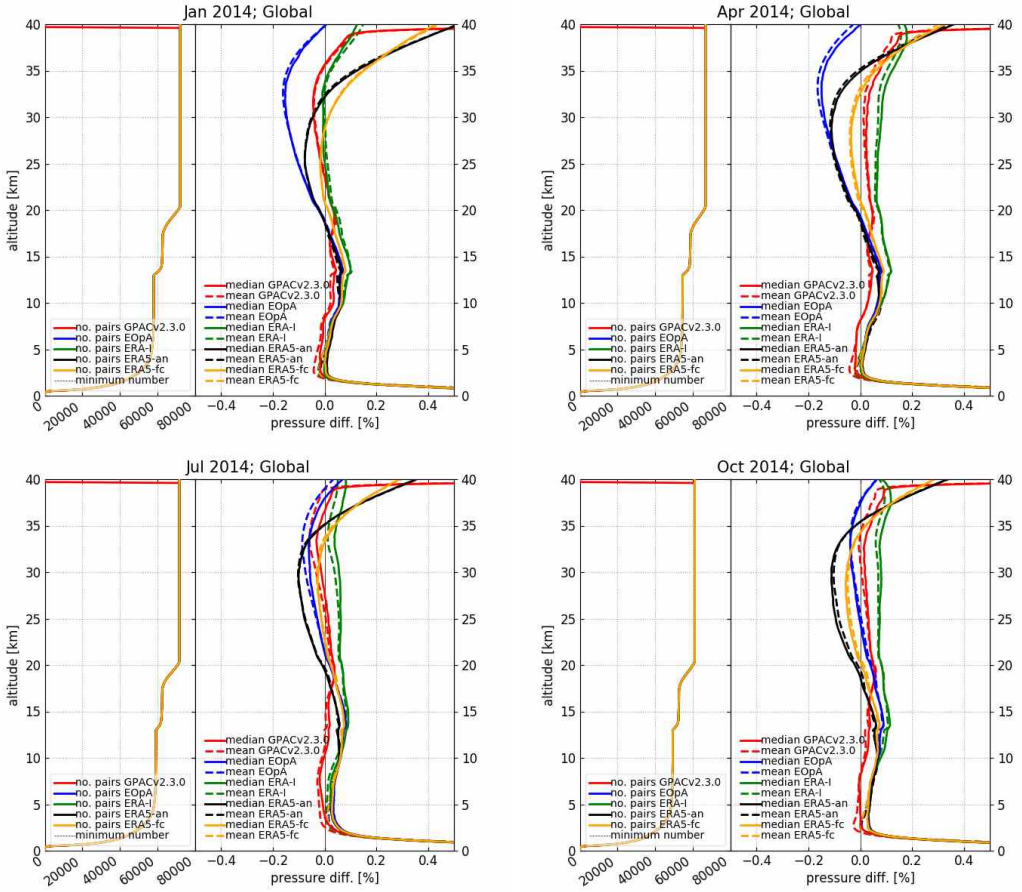

Figure 4.4: *Globally sampled pressure comparison for January, April, July, and October 2014.*

4.4 Pressure

Figure 4.4 shows the global validation results for pressure. As mentioned in the data description part (c. f. subsection 2.2.2) GPACv2.3.0 pressure (like temperature and specific humidity) is not a pure measurement product but contains background data from short term ERA-Interim forecasts in the whole height range which is shown. The two observational datasets and the three reanalysis datasets (analysis and forecast) agree within ±0.1 % between 2 km to 35 km. The operational analysis exhibits a larger offset in January and April but stays within the range of the other datasets in July and October. GPACv2.3.0 exhibits a good improvement throughout all months and in most of the zonal bins compared to ERA-Interim.

The zonal separation of the pressure validation is shown in the appendix (c. f. Figure A.4, Figure A.9, Figure A.14, Figure A.19). Inspecting them more carefully one can see that in the polar bins, especially in the southern polar bin the six datasets disagree strongest above 15 km. They exhibit different vertical behavior compared to OPSv5.6 for the different months. below 15 km the polar summer bin (60°S to 90°S in January and 60°N to 90°N in July) exhibits an interesting feature: OPSv5.6 shows a kink against all other datasets at about 10 km (about 0.2 % in January between 60°S to 90°S for the operational analysis and ERA5 (forecast and analysis); GPACv2.3.0 and ERA-Interim also exhibit this feature but do not

show it that strong; in July between 60°N to 90°N for all four model datasets; GPACv2.3.0 does not show it that strong).

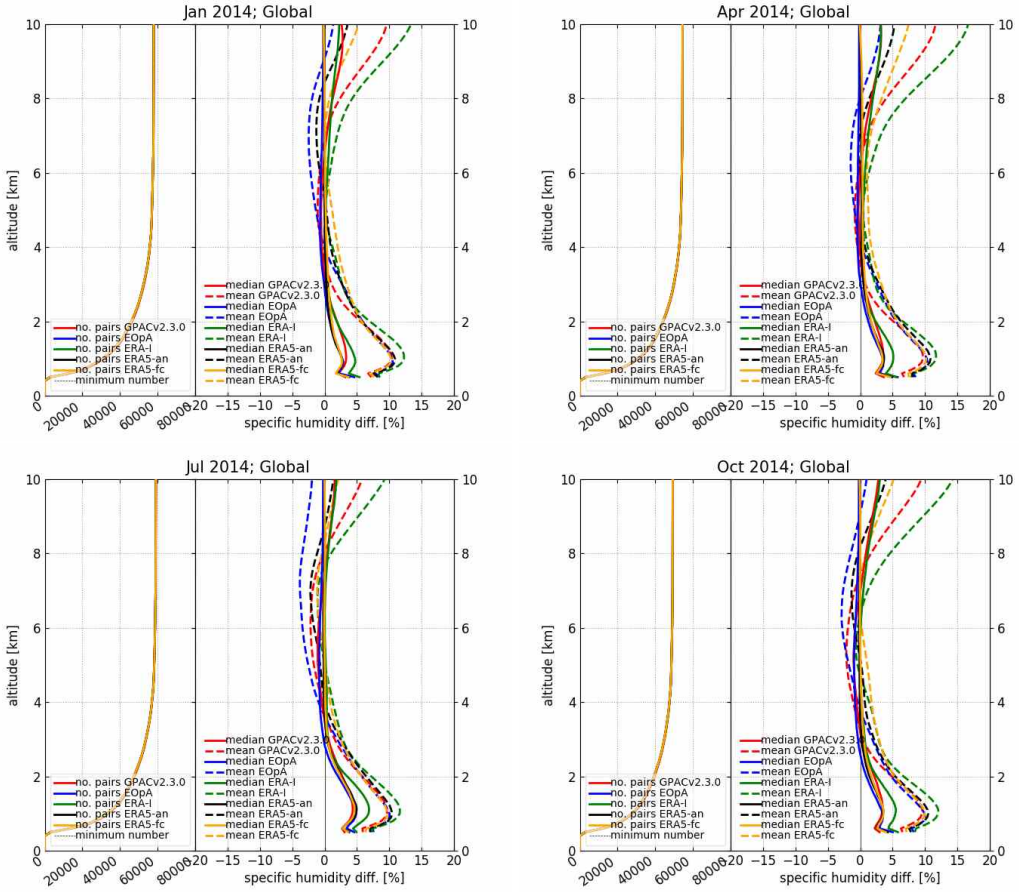

Figure 4.5: *Globally sampled specific humidity comparison for January, April, July, and October 2014.*

4.5 Specific Humidity

Figure 4.5 shows the global validation results for specific humidity. As mentioned in the data description part (c. f. subsection 2.2.2) GPACv2.3.0 specific humidity (like temperature and pressure) is not a pure measurement product but contains background data from short term ERA-Interim forecasts in the whole height range which is shown. All six datasets agree within 5 % in the median differences over the plotted height range for all month. Between 3 km to 7 km the differences are almost 0.0 %. Above that GPACv2.3.0 and ERA-Interim exhibit an increasing offset up to about 3 % at 10 km compared to OPSv5.6, ERA5 analysis and forecast and the operational analysis – the bias between the latter three datasets stays almost 0.0 %.

The zonal separation of the validation is shown in the appendix (c. f. Figure A.5, Figure A.10, Figure A.15, Figure A.20). Inspecting these results more closely we can identify that the differences between median and mean in the global validation results between surface and about 2 km to 3 km result from the tropical bin (and to a minor extent form the respective mid-latitude and sub-tropical summer bins). To a certain extent the differences above about 7 km are a result of the tropics too. In the case of ERA-Interim and GPACv2.3.0 there are additional contributions from the polar bins too, especially from January, April, and October.

5 Summary and Conclusions

This study carried out an assessment of biases of ERA5 (analysis and forecast), ERA-Interim (analysis) and ECMWF operational data (analysis), and it assessed the potential impact of its use as background data on ROM SAF level 2B offline products. The bias assessment focused on seasonal and latitudinal dependence of biases in ERA5 analysis and forecasts, ERA-Interim, and ECMWF operational analysis datasets.

Chapter 2 described the datasets, which were inter-compared in this study. In a first part it provided an overview of the RO processing and the differences between WEGC's OPSv5.6 and ROM SAF's GPACv2.3.0 datasets, the two RO datasets used as reference for the evaluations. The second part focused on the description of the model data. It characterized the resolution of the analysis/forecast fields used as well as the implemented interpolation algorithm. In addition, the main differences between the three (re-)analyses (ERA5, ERA-Interim, ECMWF operational) have been outlined.

In chapter 3 the key settings of the validation framework set up at the WEGC were described and chapter 4 provided a thorough presentation of the validation analysis.

Summarizing the outcome of this study we found:

- **Refractivity**: The two observational RO datasets OPSv5.6 and GPACv2.3.0 used as reference are in very good agreement up to 40 km. Above that height they start to differ due to the different background models used in the high-altitude initialization. The (re-)analysis datasets are within ±0.3 % compared to the RO datasets up to 40 km. Up to 12 km (re-)analyses and RO are in good agreement. The bias of the (re-)analyses exhibit a positive peak at about 18 km. ERA5 analysis and forecast as well as the operational analysis of ECMWF show an additional peak at about 38 km to 40 km. The ERA5 forecast data exhibit a smaller bias compared to the RO reference data almost for the full height range.

- **Dry temperature**: The results for dry temperature are comparable to those of refractivity except that the height range of very good agreement between the two RO datasets decreases to about 25 km to 30 km. The (re-)analysis datasets and the RO datasets are consistent within 0.25 K up to about 30 km (note that these re-/analyses assimilated RO data during the test months). Comparable to the refractivity results, the ERA5 forecast dataset exhibits a somewhat smaller bias throughout the shown height range, except between about 10 km to 15 km in January and July.

- **Temperature**: All datasets which have been compared in this study are within a range of about 0.25 K up to 30 km (except in January where this consistency is valid only up to about 27 km, due to an increasing bias of ERA5 analysis and forecast datasets). Comparable to the refractivity and dry temperature, results for ERA5 forecast data match the observations better than the ERA5 analysis data in a large part of the shown altitude range.

- **Pressure**: The two observational datasets and the two reanalysis datasets agree within ±0.1 % between 3 km and 35 km.

- **Specific humidity**: All six inter-compared datasets agree within 5 % in the median

differences over the relevant tropospheric height range for all months (January, April, July, September). Between 3 km to 7 km the differences are close to 0.0 %. Above that, GPACv2.3.0 and ERA-Interim exhibit an increasing offset, up to about 3 % at 10 km, compared to the other four datasets (OPSv5.6, ERA5 analysis and forecast, and ECMWF operational) – the bias between the latter four datasets stays close to 0.0 %.

Overall the results of the study strongly suggest to use the ERA5 forecast data as background for future 1D-Var products of GPAC/ROPP datasets. In the relevant parameters (temperature, specific humidity, and pressure) and the relevant tropospheric height range (0 km to 15 km), respectively, it exhibited a better performance than the ERA-Interim analysis (currently ERA-Interim forecast data are used as background dataset for the ROPP 1D-Var process). It has to be noted that the GPAC/ROPP 1D-Var effects the geopotential heights at all altitude levels. For that reason the tropospheric retrieval results are not necessarily independent from potential stratospheric biases.

The suggested changes in the background data setup in combination with changes in the setup of the background covariance matrices (the ATROMSAF1-FA05 project found promising results in a preliminary study using dynamic background and measurement error covariance matrices; see [RD.35]) will likely lead to an improved tropospheric product within a new GPAC reprocessing upcoming in 2020.

Acknowledgments

The author thanks J. Nielsen (DMI), K. Lauritsen (DMI), and G. Kirchengast (WEGC) for support and advice throughout this VS study and during the VS report finalization. In addition the author wants to thank J. Danzer (WEGC) for supporting with proofreading of a draft-final version of the report. Access to the GPACv2.3.0 dataset was provided by the ROM SAF, and access to ERA5, ERA-Interim, and ECMWF operational (re-)analysis and forecast fields was provided by ECMWF Reading, UK.

Acronyms and abbreviations

AN	analysis
ATROMSAF	Austrian Federated Activity with the EUMETSAT/ROM SAF Consortium during the CDOP-3 First-half Period
BAROCLIM	Bending Angle Radio Occultation Climatology
CDAAC	COSMIC Data Analysis and Archive Center
COSMIC	Constellation Observing System for Meteorology, Ionosphere, and Climate
CDOP	Continuous Development and Operations Phase
CT2	Canonical Transformation Version 2
DMI	Danish Meteorological Institute
ECMWF	European Centre for Medium-Range Weather Forecasts
EGM96	Earth Gravitational Model 1996
EOpA	ECMWF Operational Analysis
ERA	ECMWF Re-Analysis
FA	Federated Activity
FC	forecast
FORMOSAT-3	Formosa Satellite mission-3
GNSS	Global Navigation Satellite System
GO	Geometric Optics
GPAC	GNSS Processing and Archiving Center
GPS	Global Positioning System
GRACE	Gravity Recovery and Climate Experiment
LEO	low earth orbit
METOP	Meteorological Operational satellite series
MSISE-90	1990 Extended Mass Spectrometer and Incoherent Scatter Radar atmospheric model
OPS	Occultation Processing System
RO	Radio Occultation
ROM SAF	Radio Occultation Meteorology Satellite Application Facility
UCAR	University Corporation for Atmospheric Research
VS	Visiting Scientist
WEGC	Wegener Center
WO	Wave Optics

Reference Documents

[RD.1] Angerer, B., Ladstädter, F., Scherllin-Pirscher, B., Schwärz, M., Steiner, A. K., Foelsche, U., and Kirchengast, G., Quality aspects of the WEGC multi-satellite GPS radio occultation record OPSv5.6, *Atmos. Meas. Tech.*, *10*, 4845–4863, 2017.

[RD.2] Ao, C. O., Schreiner, W. S., and Wickert, J., First report on the CHAMP radio occultation intercomparison study, Jpl publication 03-016, JPL, 2003.

[RD.3] Bai, W.-H., Liu, C.-L., Meng, X.-G., Sun, Y.-Q., Kirchengast, G., Du, Q.-F., Wang, X.-Y., Yang, G.-L., Liao, M., Yang, Z.-D., Zhao, D.-Y., Xia, J.-M., Cai, Y.-R., Liu, L.-J., and Wang, D.-W., Evaluation of atmospheric profiles derived from single- and zero-difference excess phase processing of BeiDou System radio occultation data of the FY-3C GNOS mission, *Atmos. Meas. Tech.*, in submission (OPAC-IROWG 2016 Special Issue), 2017.

[RD.4] Culverwell, I., The radio occultation processing package (ROPP) user guide, part II: Forward model and 1D–Var modules, version 6.0, Tech. rep., GRAS SAF, ref: SAF/ GRAS/ METO/ UG/ ROPP/003, 2011.

[RD.5] Dee, D. P., Uppala, S. M., Simmons, A. J., Berrisford, P., Poli, P., Kobayashi, S., Andrae, U., Balmaseda, M. A., Balsamo, G., Bauer, P., Bechtold, P., Beljaars, A. C. M., van de Berg, L., Bidlot, J., Bormann, N., Delsol, C., Dragani, R., Fuentes, M., Geer, A. J., Haimberger, L., Healy, S. B., Hersbach, H., Hólm, E. V., Isaksen, L., Kållberg, P., Köhler, M., Matricardi, M., McNally, A. P., Monge-Sanz, B. M., Morcrette, J.-J., Park, B.-K., Peubey, C., de Rosnay, P., Tavolato, C., Thépaut, J.-N., and Vitart, F., The ERA-Interim reanalysis: configuration and performance of the data assimilation system, *Quart. J. Roy. Meteor. Soc.*, *137*, 553–597, 2011.

[RD.6] ECMWF, IFS Documentation CY36R1, URL `https://www.ecmwf.int/en/publications/search?solrsort=ts_biblio_year%20desc&secondary_title=%22IFS%20Documentation%20CY36R1%22`, 2010.

[RD.7] ECMWF, IFS Documentation CY40R1, URL `https://www.ecmwf.int/en/publications/search/?solrsort=sort_label%20asc&secondary_title=%22IFS%20Documentation%20CY40R1%22`, 2014.

[RD.8] ECMWF, IFS Documentation CY41R2, URL `https://www.ecmwf.int/en/publications/search/?solrsort=sort_label%20asc&secondary_title=%22IFS%20Documentation%20CY41R2%22`, 2016.

[RD.9] ECMWF, ERA-5 Documentation, URL `https://confluence.ecmwf.int/display/CKB/ERA5+data+documentation`, 2019.

[RD.10] Fjeldbo, G., Kliore, A. J., and Eshleman, V. R., The neutral atmosphere of Venus as studied with the Mariner V radio occultation experiments, *The Astronomical Journal*, *76*, 123–140, 1971.

[RD.11] Foelsche, U., Borsche, M., Steiner, A. K., Gobiet, A., Pirscher, B., Kirchengast, G., Wickert, J., and Schmidt, T., Observing upper troposphere-lower stratosphere

climate with radio occultation data from the CHAMP satellite, *Climate Dyn.*, *31*, 49–65, 2008.

[RD.12] Gorbunov, M. E., Canonical transform method for processing radio occultation data in the lower troposphere, *Radio Sci.*, *37*, 2002.

[RD.13] Gorbunov, M. E., Benzon, H.-H., Jensen, A. S., Lohmann, M. S., and Nielsen, A. S., Comparative analysis of radio occultation processing approaches based on Fourier integral operators, *Radio Sci.*, *39*, 2004.

[RD.14] Healy, S. B. and Eyre, J. R., Retrieving temperature, water vapour and surface pressure information from refractive-index profiles derived by radio occultation: A simulation study, *Quart. J. Roy. Meteor. Soc.*, *126*, 1661–1683, 2000.

[RD.15] Hersbach, H., Bell, B., Berrisford, P., Horányi, A., Sabater, J. M., Nicolas, J., Radu, R., Schepers, D., Simmons, A., Soci, C., and Dee, D., Global reanalysis: goodbye ERA-Interim, hello ERA5, *ECMWF Newsletter*, *159*, 17–24, 2019.

[RD.16] Ho, S.-P., Hunt, D., Steiner, A. K., Mannucci, A. J., Kirchengast, G., Gleisner, H., Heise, S., von Engeln, A., Marquardt, C., Sokolovskiy, S., Schreiner, W., Scherllin-Pirscher, B., Ao, C., Wickert, J., Syndergaard, S., Lauritsen, K., Leroy, S., Kursinski, E. R., Kuo, Y.-H., Foelsche, U., Schmidt, T., and Gorbunov, M., Reproducibility of GPS radio occultation data for climate monitoring: Profile-to-profile intercomparison of CHAMP climate records 2002 to 2008 from six data centers, *J. Geophys. Res.*, *117*, 2012.

[RD.17] Hocke, K., Igarashi, K., and Tsuda, T., High-resolution profiling of layered structures in the lower stratosphere by GPS occultation, *Geophys. Res. Lett.*, *30*, 2003.

[RD.18] Jensen, A. S., Lohmann, M. S., Benzon, H.-H., and Nielsen, A. S., Full spectrum inversion of radio occultation signals, *Radio Sci.*, *38*, 2003.

[RD.19] Jensen, A. S., Lohmann, M. S., Nielsen, A. S., and Benzon, H.-H., Geometrical optics phase matching of radio occultation signals, *Radio Sci.*, *39*, 2004.

[RD.20] Kursinski, E. R. and Gebhardt, T., A Method to Deconvolve Errors in GPS RO-Derived Water Vapor Histograms, *J. Atmos. Oceanic Technol.*, *31*, 2606–2628, 2014.

[RD.21] Kursinski, E. R., Hajj, G. A., Bertiger, W. I., Leroy, S. S., Meehan, T. K., Romans, L. J., Schofield, J. T., McCleese, D. J., Melbourne, W. G., Thornton, C. L., Yunck, T. P., Eyre, J. R., and Nagatani, R. N., Initial results of radio occultation observations of Earth's atmosphere using the Global Positioning System, *Science*, *271*, 1107–1110, 1996.

[RD.22] Kursinski, E. R., Hajj, G. A., Schofield, J. T., Linfield, R. P., and Hardy, K. R., Observing Earth's atmosphere with radio occultation measurements using the Global Positioning System, *J. Geophys. Res.*, *102*, 23 429–23 465, 1997.

[RD.23] Lackner, B. C., Steiner, A. K., Kirchengast, G., and Hegerl, G. C., Atmospheric climate change detection by radio occultation data using a fingerprinting method,

J. Climate, *24*, 5275–5291, 2011.

[RD.24] Lauritsen, K., Structural uncertainty and error characterisation of ROM SAF profile and gridded products, ROM SAF CDOP-3 Federated activity proposal No. 05, ROM SAF, ref: SAF/ROM/DMI/MGT/FA05/001, 2017.

[RD.25] Löscher, A., Lauritsen, K. B., and Sørensen, M., The GRAS SAF radio occultation processing intercomparison project ROPIC, in *New Horizons in Occultation Research: Studies in Atmosphere and Climate*, edited by A. K. Steiner, B. Pirscher, U. Foelsche, and G. Kirchengast, pp. 49–62, Springer-Verlag, Berlin, Heidelberg, 2009.

[RD.26] Melbourne, W. G., Davis, E. S., Duncan, C. B., Hajj, G. A., Hardy, K. R., Kursinski, E. R., Meehan, T. K., Young, L. E., and Yunck, T. P., The application of spaceborne GPS to atmospheric limb sounding and global change monitoring, Tech. rep., Jet Propulsion Laboratory, NASA, Pasadena, California, USA, 1994.

[RD.27] Nielsen, J. K., Algorithm theoretical baseline document: Level 2B and 2C 1D-Var products, ROM SAF CDOP-3, ROM SAF, URL `http://www.romsaf.org)`, ref: SAF/ROM/DMI/ALG/1DVAR/002, 2018.

[RD.28] ROM SAF, ROM SAF Product Archive, URL `http://www.romsaf.org/product_archive.php`, 2019.

[RD.29] Scherllin-Pirscher, B., Kirchengast, G., Steiner, A. K., Kuo, Y.-H., and Foelsche, U., Quantifying uncertainty in climatological fields from GPS radio occultation: an empirical-analytical error model, *Atmos. Meas. Tech.*, *4*, 2019–2034, 2011.

[RD.30] Scherllin-Pirscher, B., Steiner, A. K., Kirchengast, G., Kuo, Y.-H., and Foelsche, U., Empirical analysis and modeling of errors of atmospheric profiles from GPS radio occultation, *Atmos. Meas. Tech.*, *4*, 1875–1890, 2011.

[RD.31] Scherllin-Pirscher, B., Syndergaard, S., Foelsche, U., and Lauritsen, K. B., Generation of a bending angle radio occultation climatology (BAROCLIM) and its use in radio occultation retrievals, *Atmos. Meas. Tech.*, *8*, 109–124, 2015.

[RD.32] Schreiner, W., Kuo, Y.-H., Ho, S.-P., Sokolovskiy, S., and Hunt, D., Use of GNSS radio occultation data for climate applications, URL `http://www.cosmic.ucar.edu/groupAct/references/WCRP-2011-Schreiner-Final.pdf`, World Climate Research Program Conference, 24–28 October 2011: Denver, Colorado U.S.A, 2011.

[RD.33] Schreiner, W. S., Rocken, C., Sokolovskiy, S., and Hunt, D., Quality assessment of COSMIC/FORMOSAT-3 GPS radio occultation data derived from single- and double-difference atmospheric excess phase processing, *GPS Solut.*, *14*, 13–22, 2010.

[RD.34] Schwärz, M., Kirchengast, G., Scherllin-Pirscher, B., Schwarz, J., Ladstädter, F., and Angerer, B., Multi-mission validation by satellite radio occultation – extension project, Final report for ESA/ESRIN No. 01/2016, WEGC, University of Graz, Austria, 2016.

[RD.35] Schwärz, M., Proschek, V., Ladstädter, F., Wappis, E., and Kirchengast, G., Austrian Federated Activity with the EUMETSAT ROM SAF consortium during the CDOP-3 first-half period—structural uncertainty and error characterization of ROM SAF profile and gridded products, Technical report for FFG and ROM SAF No. 01/2019, WEGC, University of Graz, Austria, 2019.

[RD.36] Simmons, A., ERA5, presentation given at the 5th International Conference on Reanalysis (ICR5), 13-17 November 2017, 2017.

[RD.37] Simmons, A. J. and Burridge, D. M., An energy and angular-momentum conserving vertical finite-difference scheme and hybrid vertical coordinates, *Mon. Wea. Rev.*, *109*, 758–766, 1981.

[RD.38] Smith, E. and Weintraub, S., The constants in the equation for atmospheric refractive index at radio frequencies, *Proc. IRE*, *41*, 1035–1037, 1953.

[RD.39] Sofieva, V. and Dalaudier, F., Recommendations for validation of high-resolution temperature profiles, Technical note, 2010.

[RD.40] Sokolovskiy, S., Rocken, C., Hunt, D., Schreiner, W., Johnson, J., Masters, D., and Esterhuizen, S., GPS profiling of the lower troposphere from space: Inversion and demodulation of the open-loop radio occultation signals, *Geophys. Res. Lett.*, *33*, 2006.

[RD.41] Steiner, A. K., Hunt, D., Ho, S.-P., Kirchengast, G., Mannucci, A. J., Scherllin-Pirscher, B., Gleisner, H., von Engeln, A., Schmidt, T., Ao, C., Leroy, S. S., Kursinski, E. R., Foelsche, U., Gorbunov, M., Heise, S., Kuo, Y.-H., Lauritsen, K. B., Marquardt, C., Rocken, C., Schreiner, W., Sokolovskiy, S., Syndergaard, S., and Wickert, J., Quantification of structural uncertainty in climate data records from GPS radio occultation, *Atmos. Chem. Phys.*, *13*, 1469–1484, 2013.

[RD.42] Steiner, A. K., Ladstädter, F., Ao, C. O., Gleisner, H., Ho, S.-P., Hunt, D., Schmidt, T., Foelsche, U., Kirchengast, G., Kuo, Y.-H., Lauritsen, K. B., Mannucci, A. J., Nielsen, J. K., Schreiner, W., Schwärz, M., Sokolovskiy, S., Syndergaard, S., and Wickert, J., Consistency and structural uncertainty of multi-mission GPS radio occultation records, 2019.

[RD.43] von Engeln, A., A first test of climate monitoring with radio occultation instruments: Comparing two processing centers, *Geophys. Res. Lett.*, *33*, 2006.

[RD.44] Vorob'ev, V. V. and Krasil'nikova, T. G., Estimation of the accuracy of the atmospheric refractive index recovery from Doppler shift measurements at frequencies used in the NAVSTAR system, *Izv. Atmos. Ocean. Phys.*, *29*, 602–609, 1994.

[RD.45] Wickert, J., Das CHAMP-Radiooccultationsexperiment: Algorithmen, Prozessierungssystem und erste Ergebnisse, Scientific Tech Rep STR02/07, GeoForschungsZentrum Potsdam, 2002.

[RD.46] Zeng, Z., Sokolovskiy, S., Schreiner, W., and Hunt, D., Representation of vertical atmospheric structures by radio occultation observations in the utls: comparison to high resolution radiosonde profiles, *J. Atmos. Oceanic Technol.*, *36*, 655–670, 2019.

A Median and Mean only – Zoom

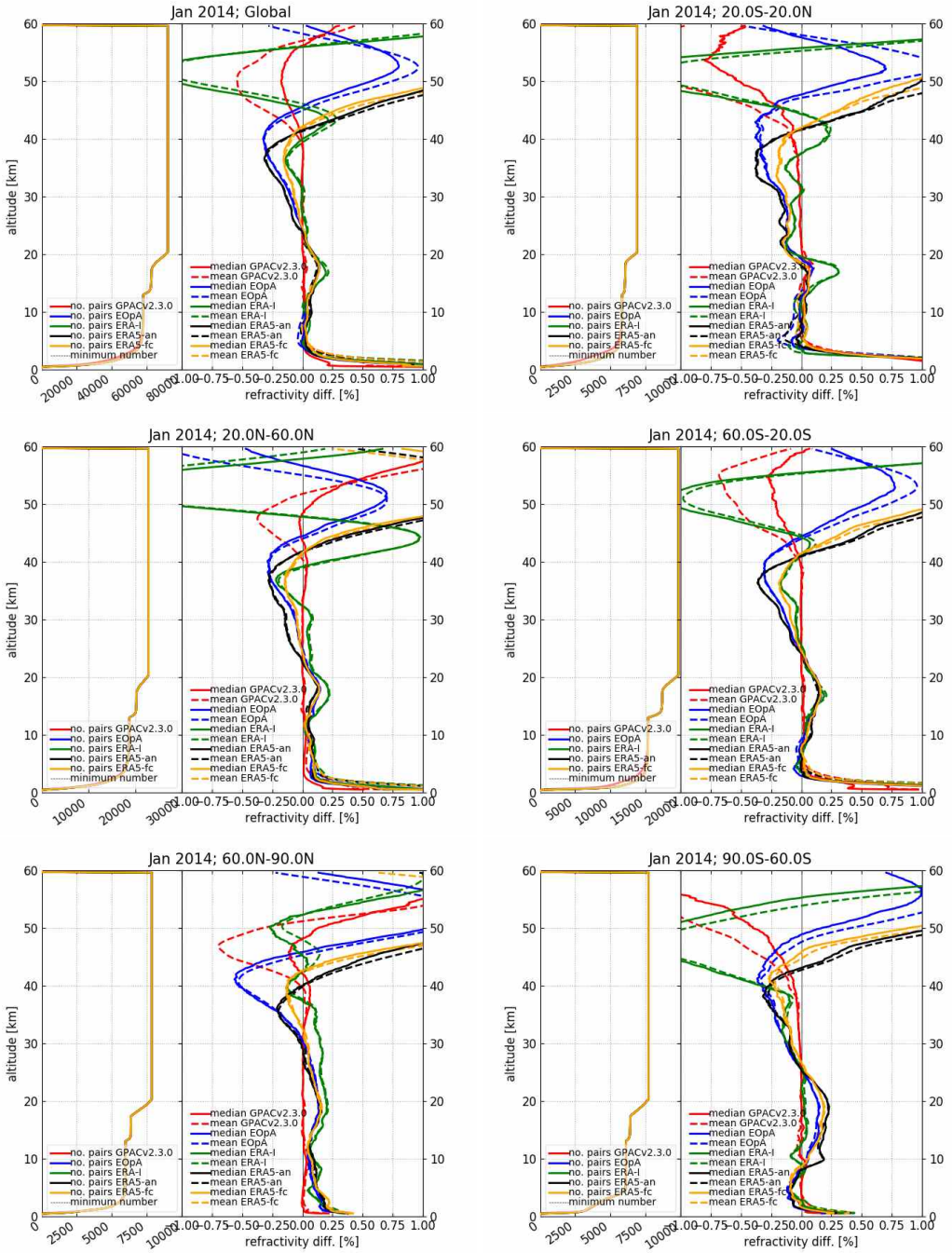

Figure A.1: *Refractivity comparison for January 2014; top left panel: global; top right: tropics (20°S to 20°N); middle left: northern hemisphere mid-latitudes and subtropics (20°N to 60°N); middle right: southern hemisphere mid-latitudes and subtropics (20°S to 60°S); bottom left: northern hemisphere polar (60°N to 90°N); bottom right: southern hemisphere polar (60°S to 90°S)*

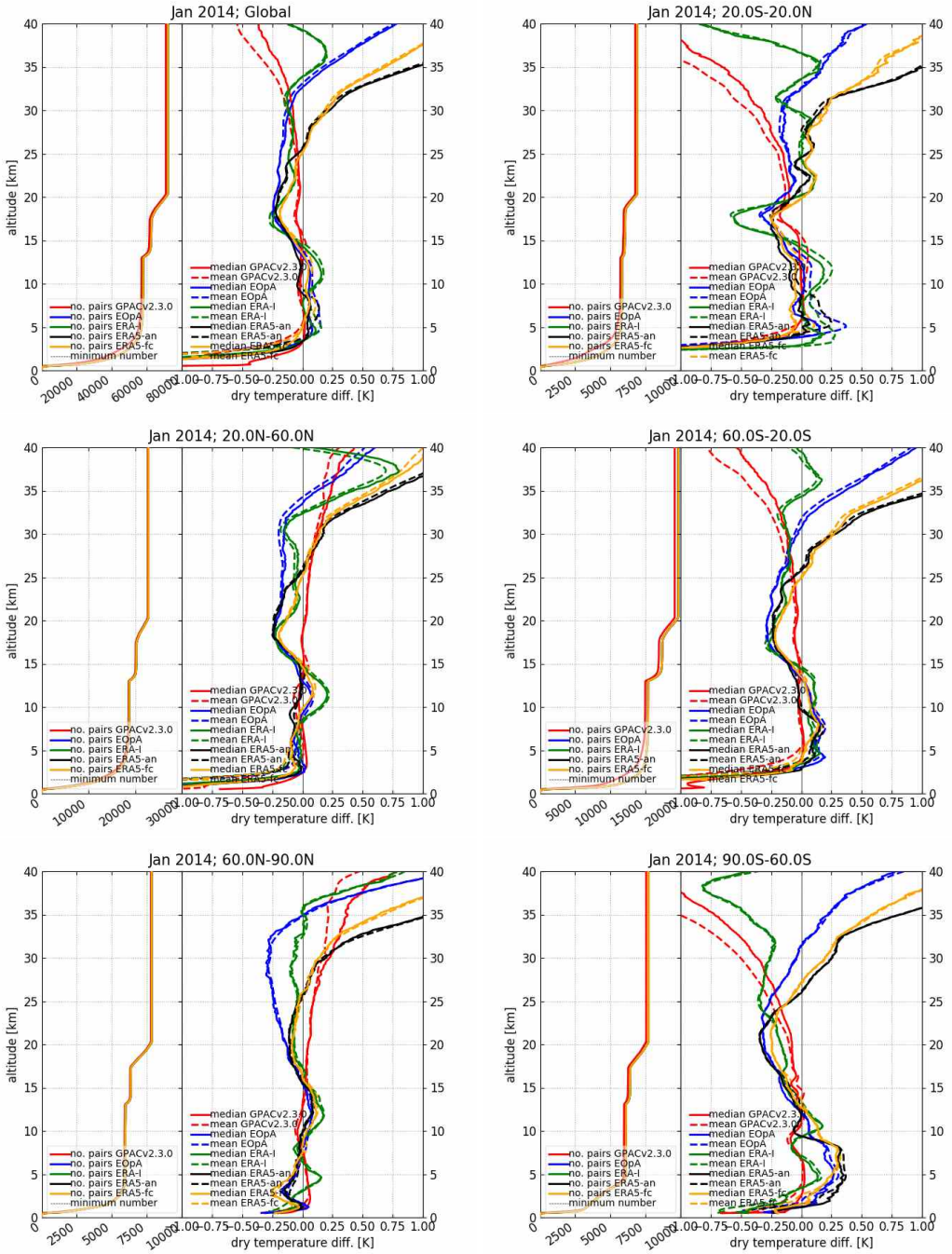

Figure A.2: *Dry temperature comparison for January 2014; top left panel: global; top right: tropics (20°S to 20°N); middle left: northern hemisphere mid-latitudes and subtropics (20°N to 60°N); middle right: southern hemisphere mid-latitudes and subtropics (20°S to 60°S); bottom left: northern hemisphere polar (60°N to 90°N); bottom right: southern hemisphere polar (60°S to 90°S)*

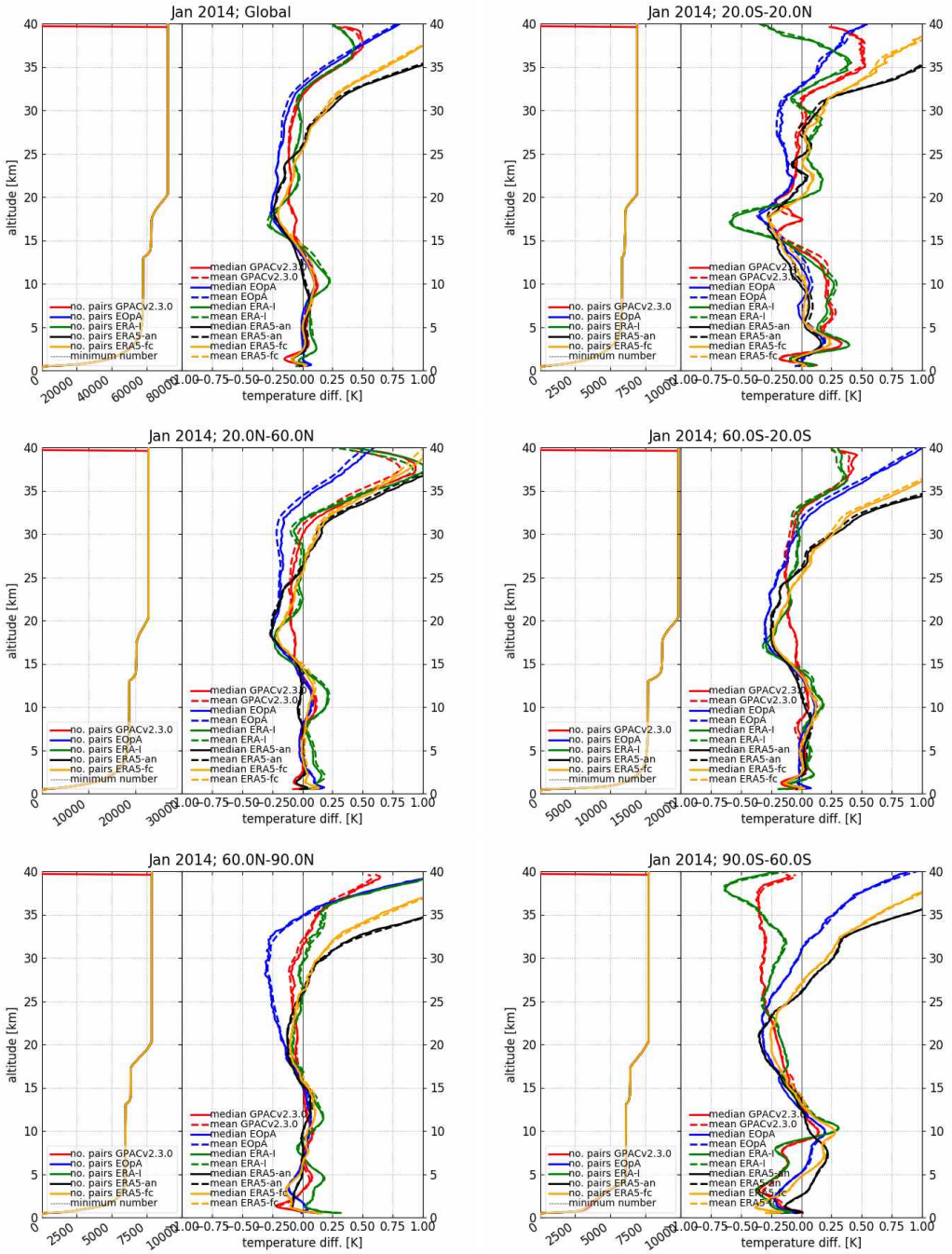

Figure A.3: *Temperature comparison for January 2014; top left panel: global; top right: tropics (20°S to 20°N); middle left: northern hemisphere mid-latitudes and subtropics (20°N to 60°N); middle right: southern hemisphere mid-latitudes and subtropics (20°S to 60°S); bottom left: northern hemisphere polar (60°N to 90°N); bottom right: southern hemisphere polar (60°S to 90°S)*

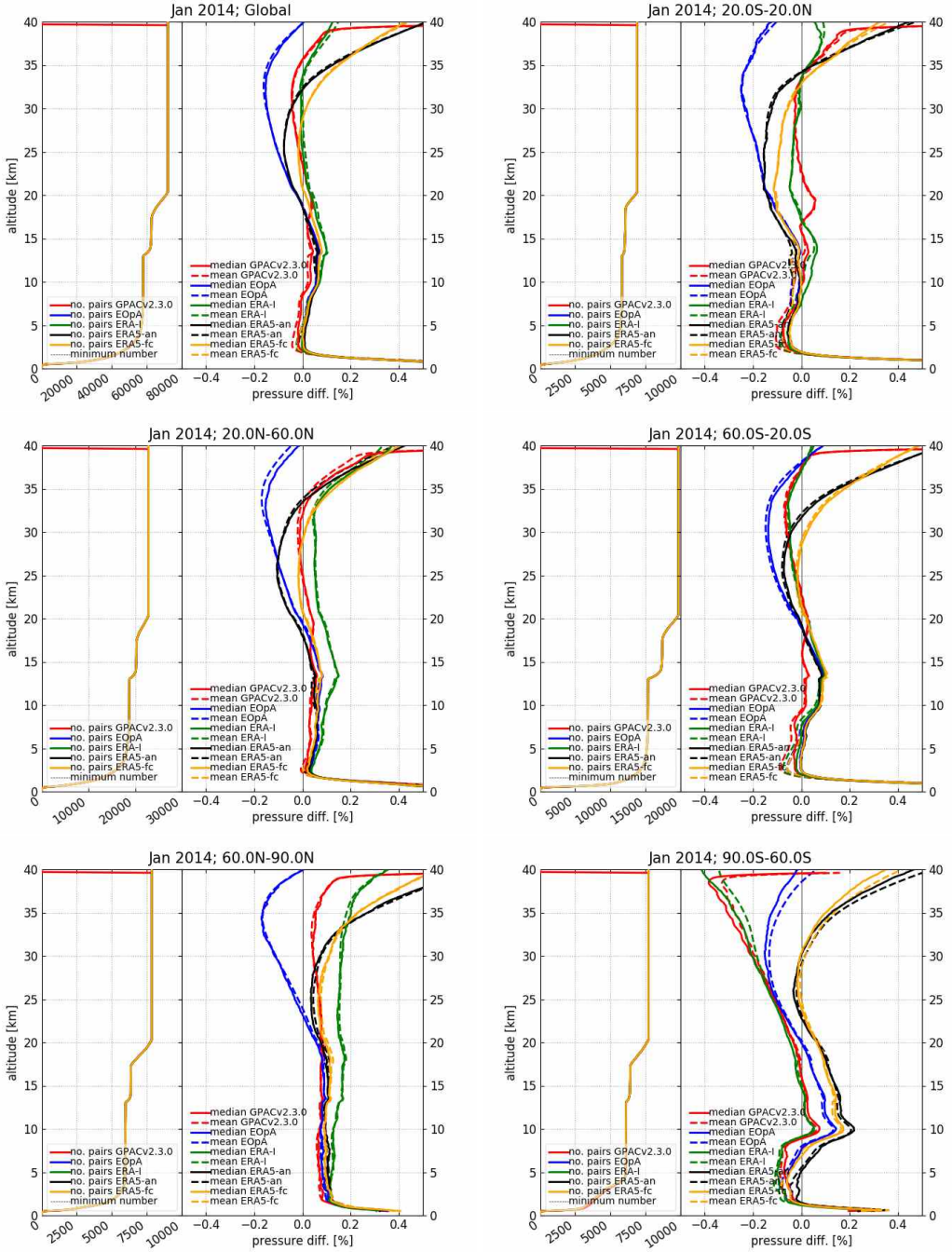

Figure A.4: *Pressure comparison for January 2014; top left panel: global; top right: tropics (20°S to 20°N); middle left: northern hemisphere mid-latitudes and subtropics (20°N to 60°N); middle right: southern hemisphere mid-latitudes and subtropics (20°S to 60°S); bottom left: northern hemisphere polar (60°N to 90°N); bottom right: southern hemisphere polar (60°S to 90°S)*

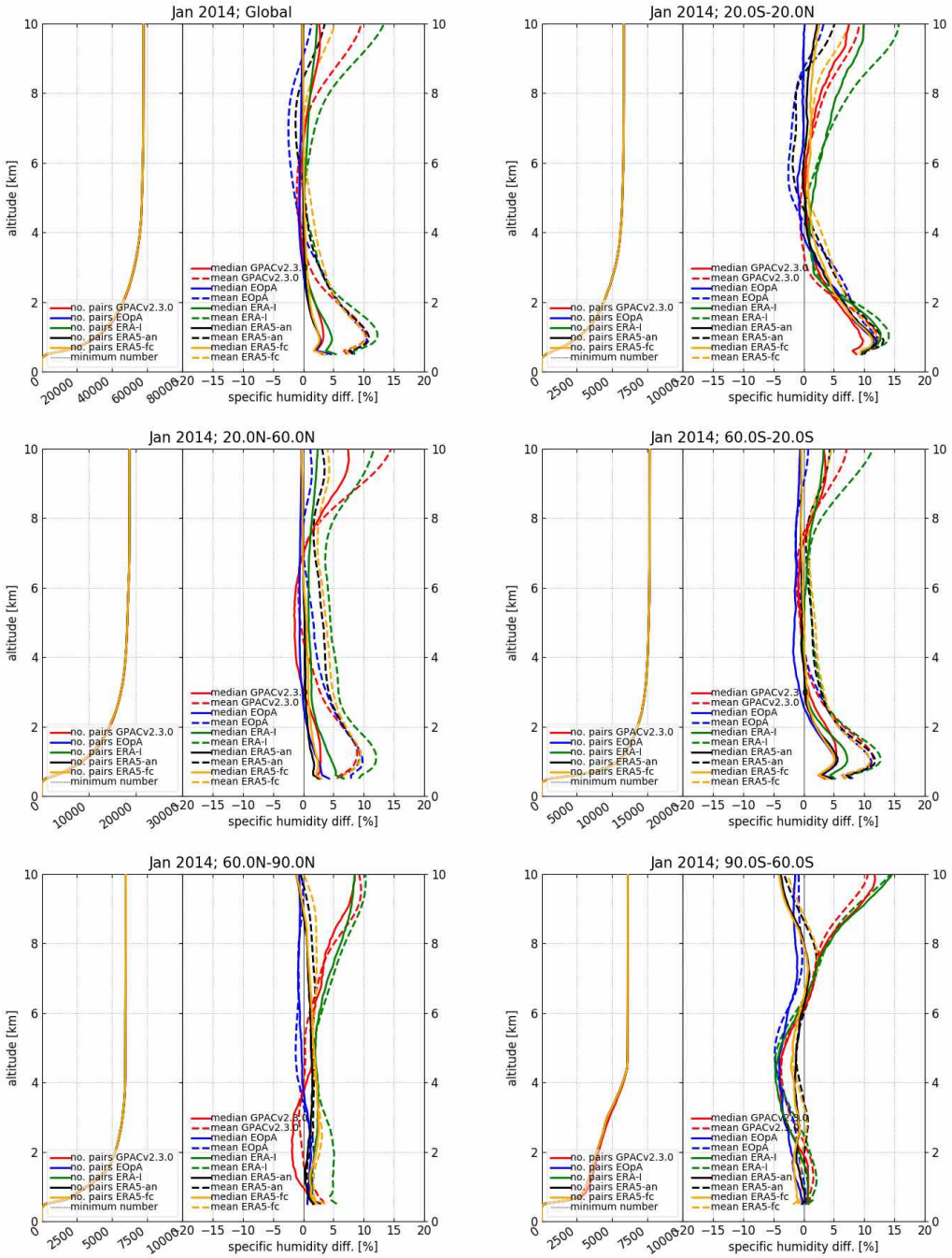

Figure A.5: *Specific humidity comparison for January 2014; top left panel: global; top right: tropics (20°S to 20°N); middle left: northern hemisphere mid-latitudes and subtropics (20°N to 60°N); middle right: southern hemisphere mid-latitudes and subtropics (20°S to 60°S); bottom left: northern hemisphere polar (60°N to 90°N); bottom right: southern hemisphere polar (60°S to 90°S)*

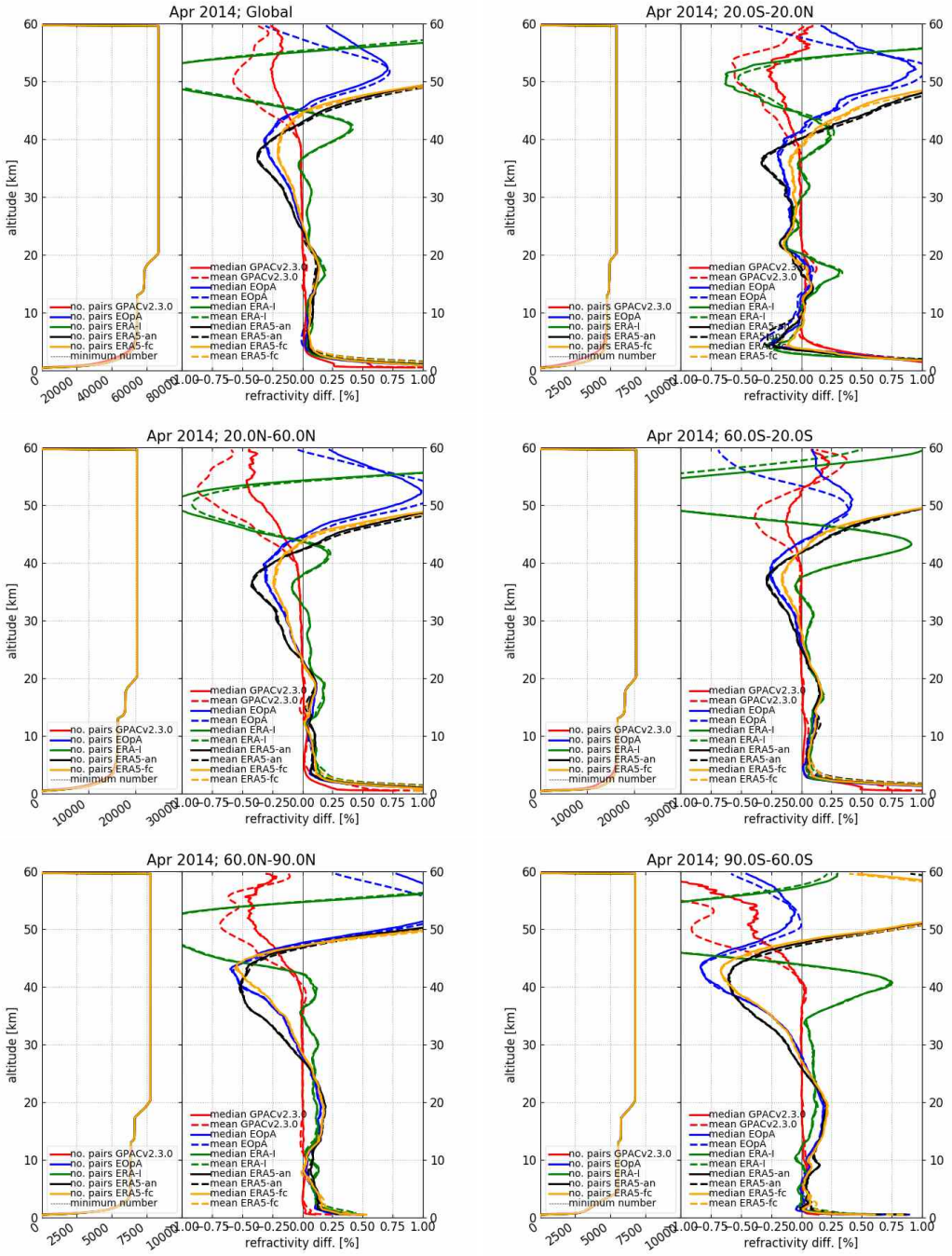

Figure A.6: *Refractivity comparison for April 2014; top left panel: global; top right: tropics (20°S to 20°N); middle left: northern hemisphere mid-latitudes and subtropics (20°N to 60°N); middle right: southern hemisphere mid-latitudes and subtropics (20°S to 60°S); bottom left: northern hemisphere polar (60°N to 90°N); bottom right: southern hemisphere polar (60°S to 90°S)*

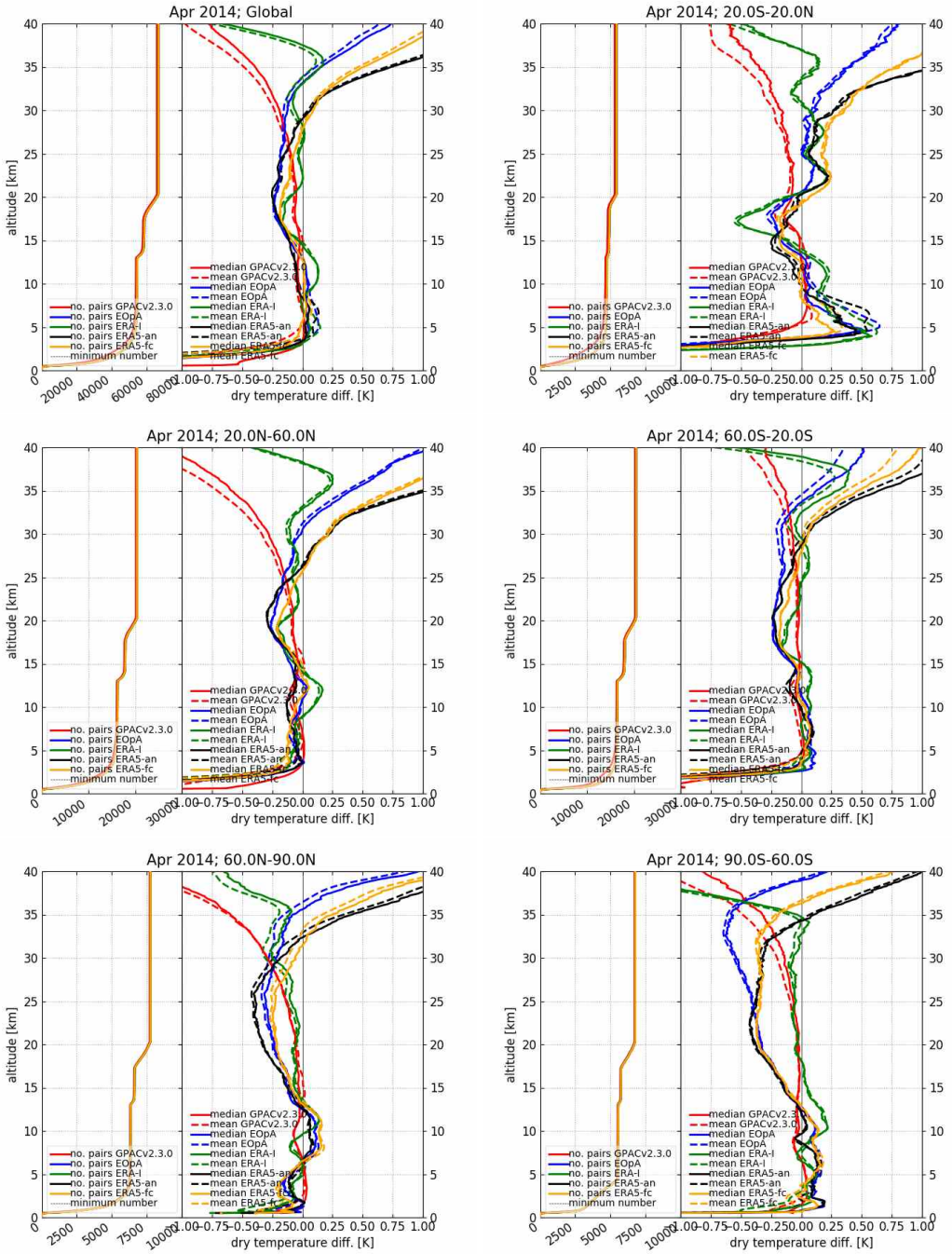

Figure A.7: *Dry temperature comparison for April 2014; top left panel: global; top right: tropics (20°S to 20°N); middle left: northern hemisphere mid-latitudes and subtropics (20°N to 60°N); middle right: southern hemisphere mid-latitudes and subtropics (20°S to 60°S); bottom left: northern hemisphere polar (60°N to 90°N); bottom right: southern hemisphere polar (60°S to 90°S)*

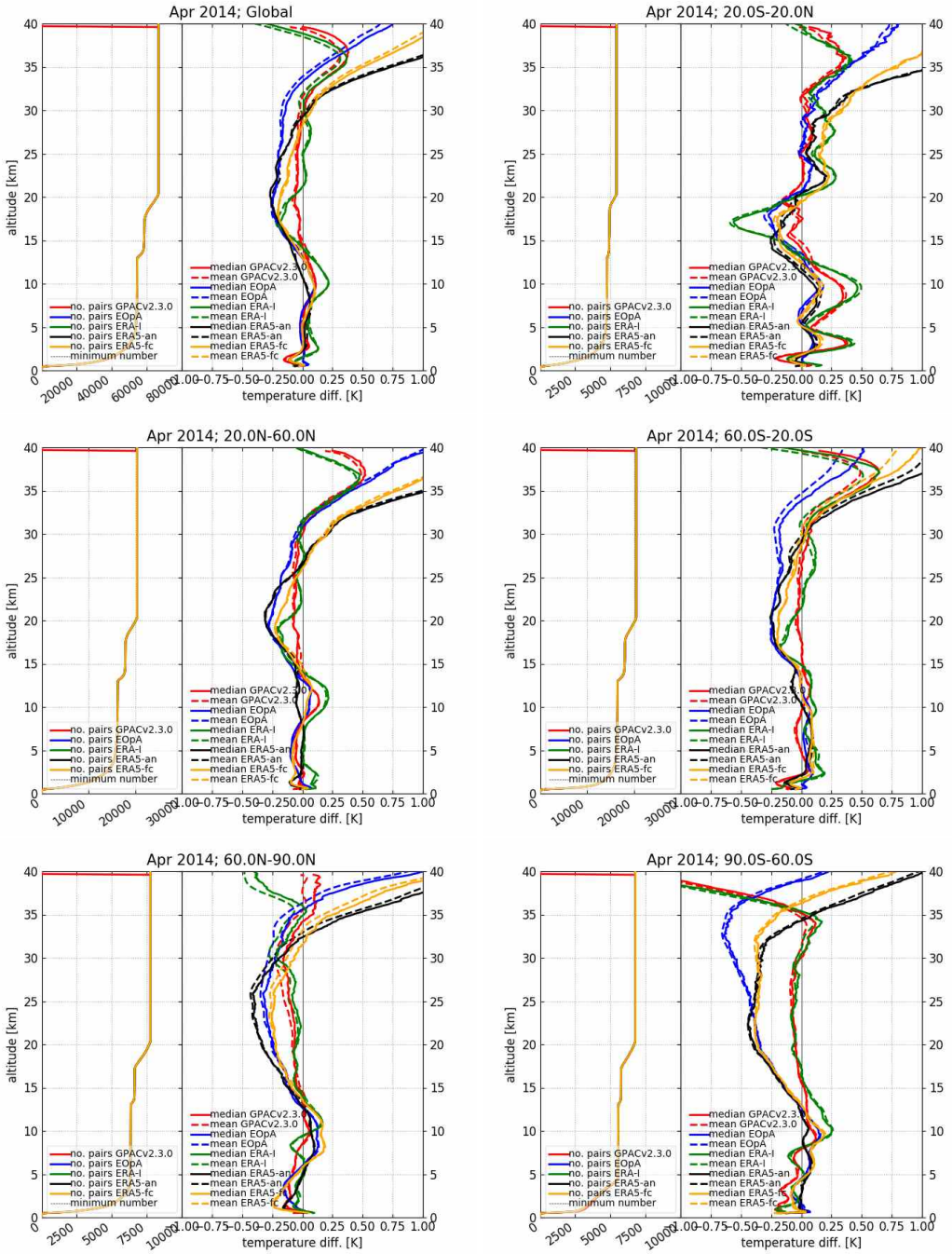

Figure A.8: *Temperature comparison for April 2014; top left panel: global; top right: tropics (20°S to 20°N); middle left: northern hemisphere mid-latitudes and subtropics (20°N to 60°N); middle right: southern hemisphere mid-latitudes and subtropics (20°S to 60°S); bottom left: northern hemisphere polar (60°N to 90°N); bottom right: southern hemisphere polar (60°S to 90°S)*

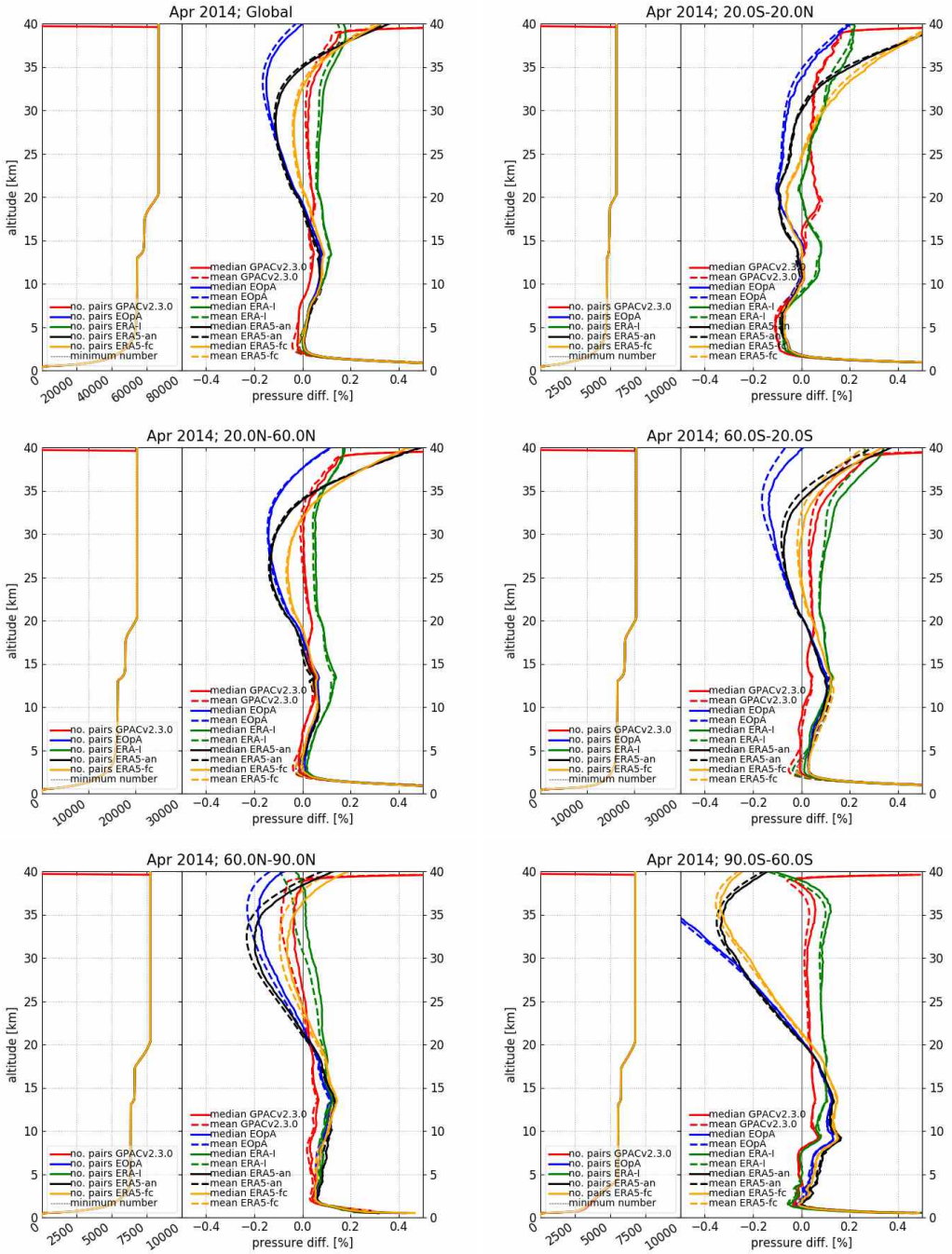

Figure A.9: *Pressure comparison for April 2014; top left panel: global; top right: tropics (20°S to 20°N); middle left: northern hemisphere mid-latitudes and subtropics (20°N to 60°N); middle right: southern hemisphere mid-latitudes and subtropics (20°S to 60°S); bottom left: northern hemisphere polar (60°N to 90°N); bottom right: southern hemisphere polar (60°S to 90°S)*

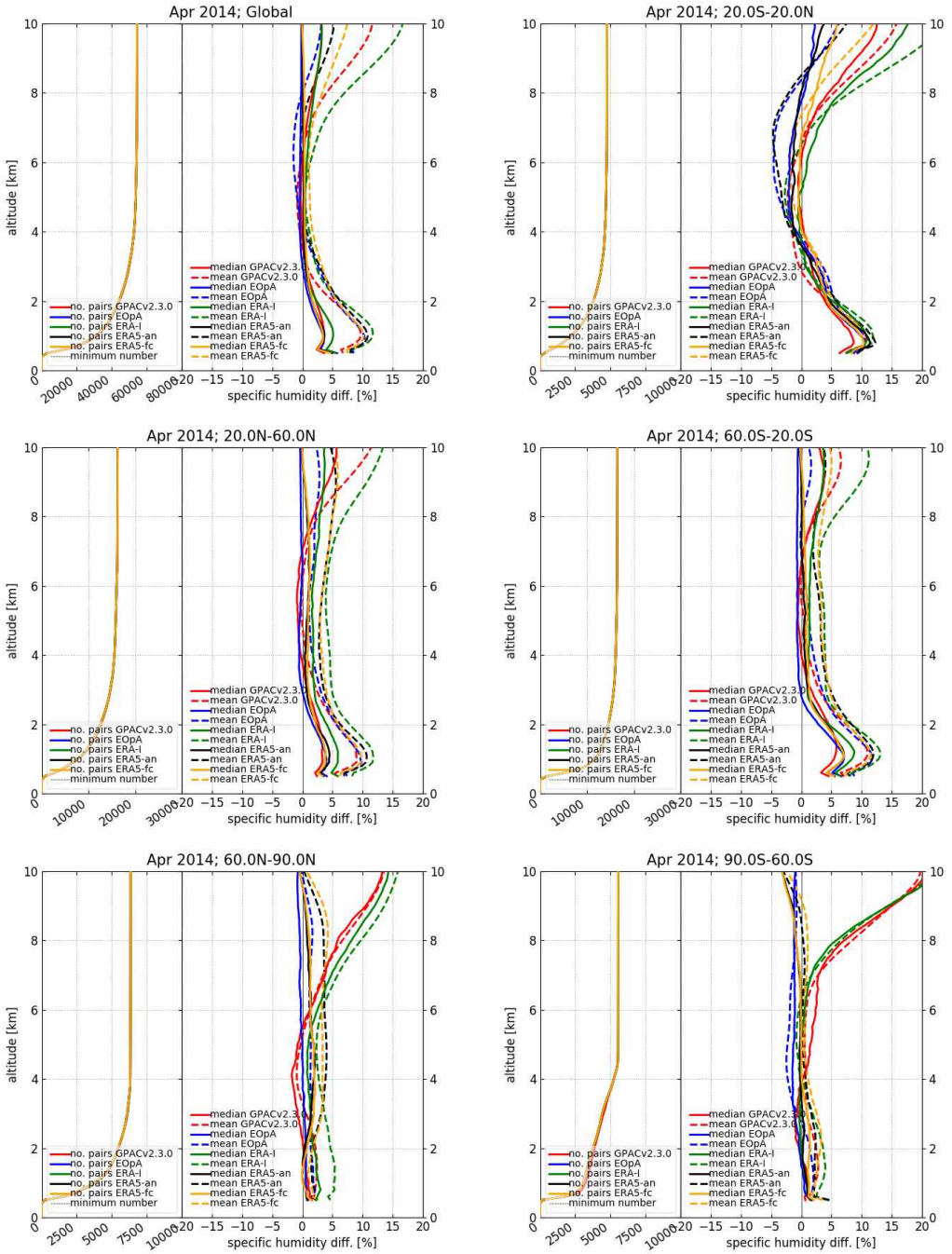

Figure A.10: *Specific humidity comparison for April 2014; top left panel: global; top right: tropics (20°S to 20°N); middle left: northern hemisphere mid-latitudes and subtropics (20°N to 60°N); middle right: southern hemisphere mid-latitudes and subtropics (20°S to 60°S); bottom left: northern hemisphere polar (60°N to 90°N); bottom right: southern hemisphere polar (60°S to 90°S)*

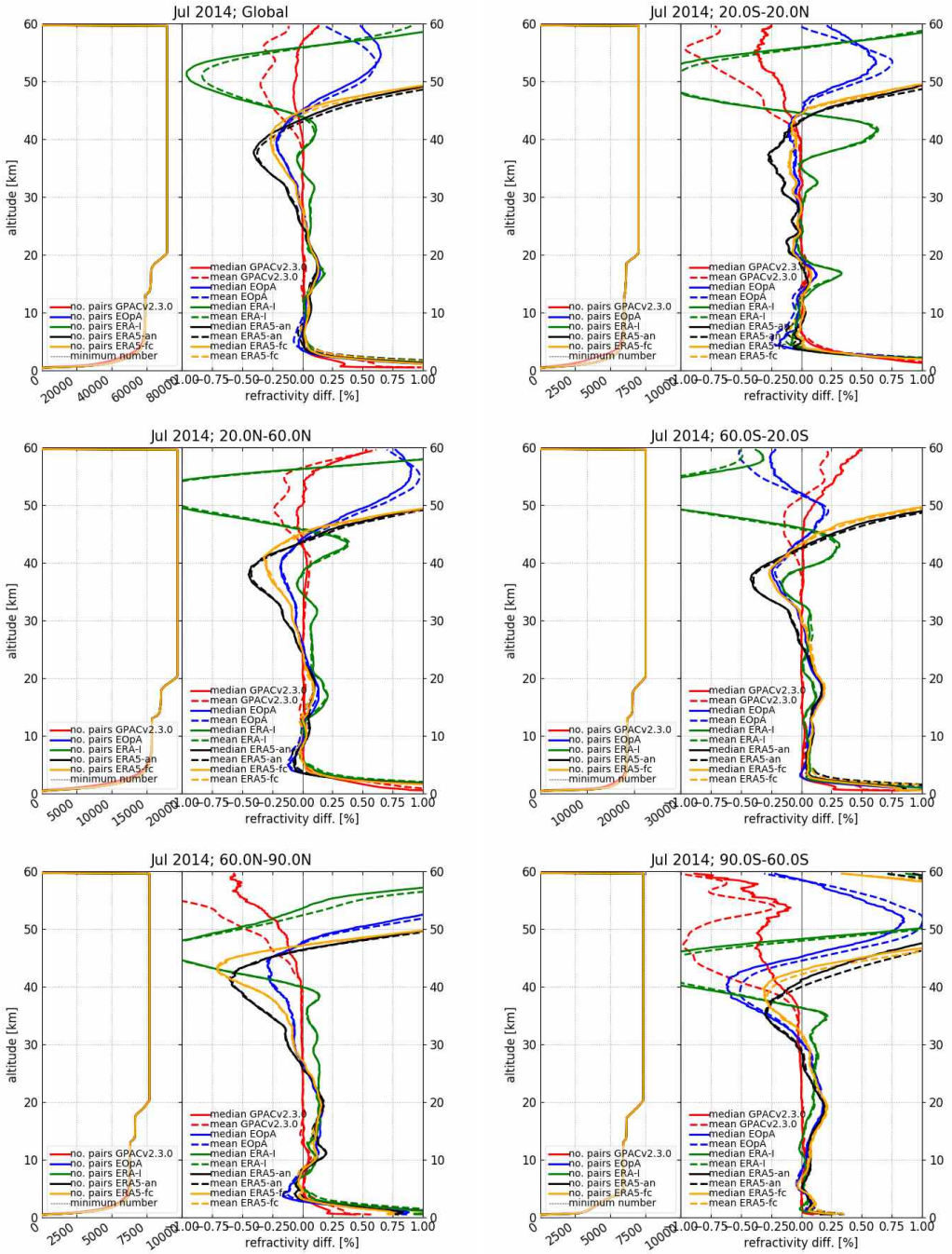

Figure A.11: *Refractivity comparison for July 2014; top left panel: global; top right: tropics (20°S to 20°N); middle left: northern hemisphere mid-latitudes and subtropics (20°N to 60°N); middle right: southern hemisphere mid-latitudes and subtropics (20°S to 60°S); bottom left: northern hemisphere polar (60°N to 90°N); bottom right: southern hemisphere polar (60°S to 90°S)*

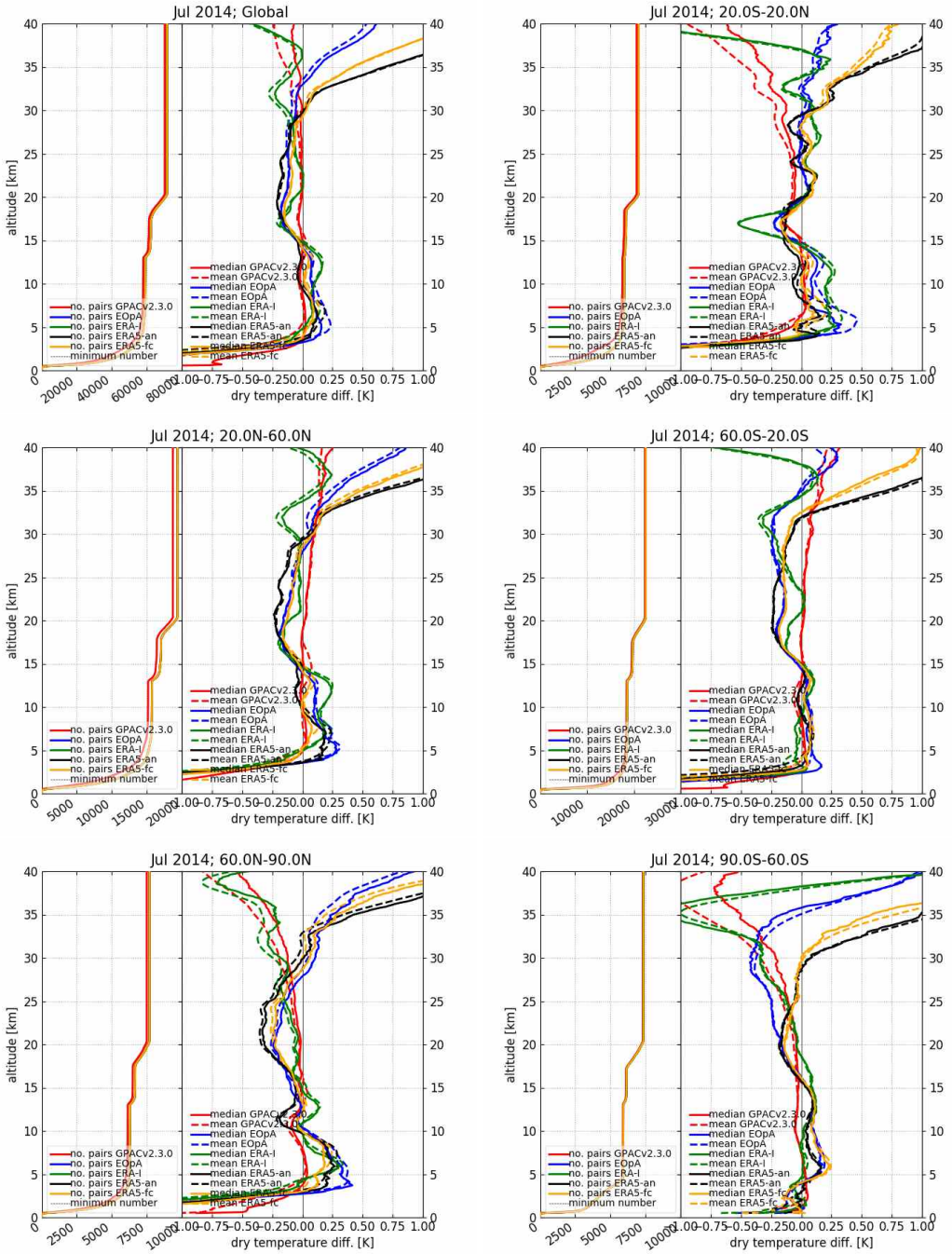

Figure A.12: *Dry temperature comparison for July 2014; top left panel: global; top right: tropics (20°S to 20°N); middle left: northern hemisphere mid-latitudes and subtropics (20°N to 60°N); middle right: southern hemisphere mid-latitudes and subtropics (20°S to 60°S); bottom left: northern hemisphere polar (60°N to 90°N); bottom right: southern hemisphere polar (60°S to 90°S)*

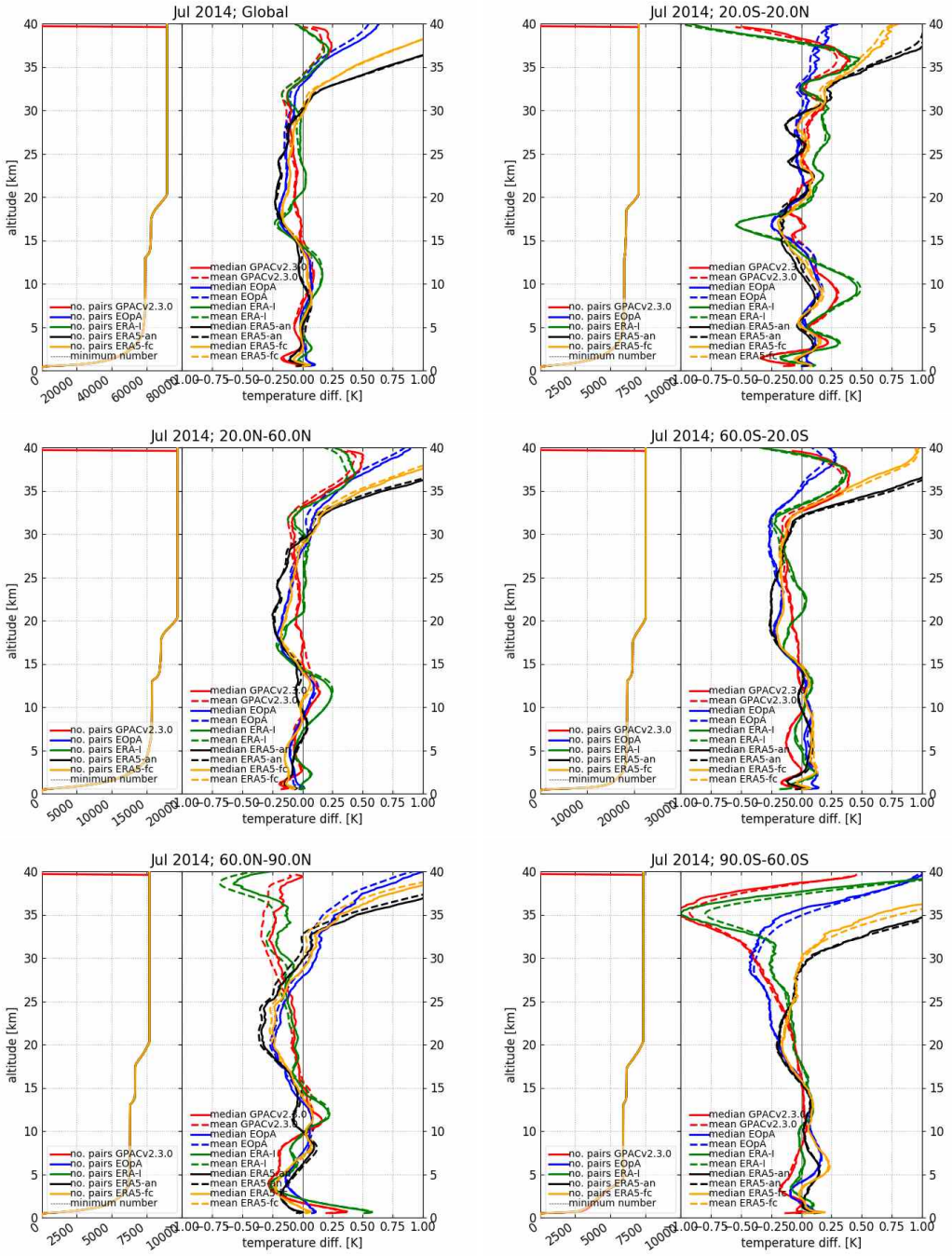

Figure A.13: *Temperature comparison for July 2014; top left panel: global; top right: tropics (20°S to 20°N); middle left: northern hemisphere mid-latitudes and subtropics (20°N to 60°N); middle right: southern hemisphere mid-latitudes and subtropics (20°S to 60°S); bottom left: northern hemisphere polar (60°N to 90°N); bottom right: southern hemisphere polar (60°S to 90°S)*

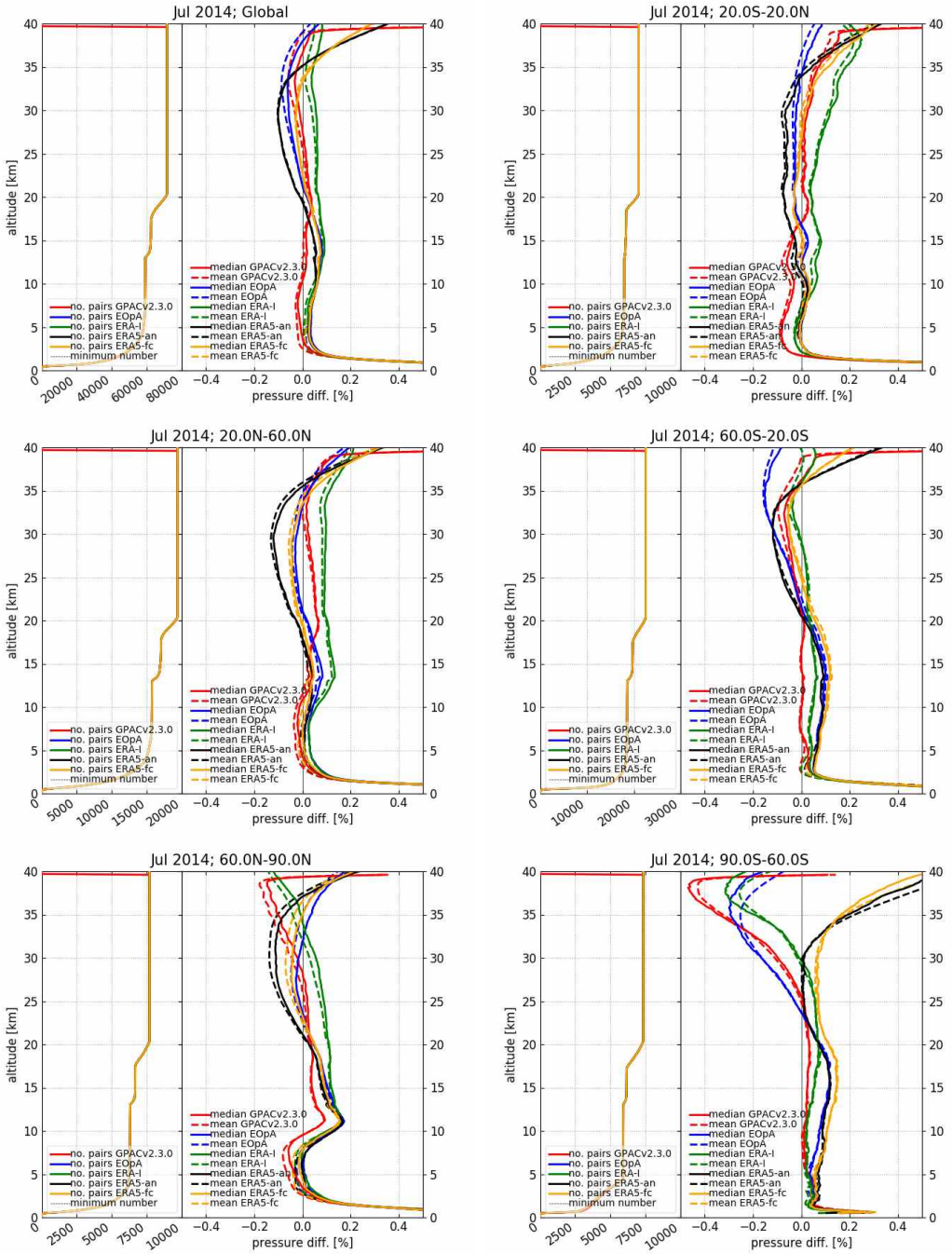

Figure A.14: *Pressure comparison for July 2014; top left panel: global; top right: tropics (20°S to 20°N); middle left: northern hemisphere mid-latitudes and subtropics (20°N to 60°N); middle right: southern hemisphere mid-latitudes and subtropics (20°S to 60°S); bottom left: northern hemisphere polar (60°N to 90°N); bottom right: southern hemisphere polar (60°S to 90°S)*

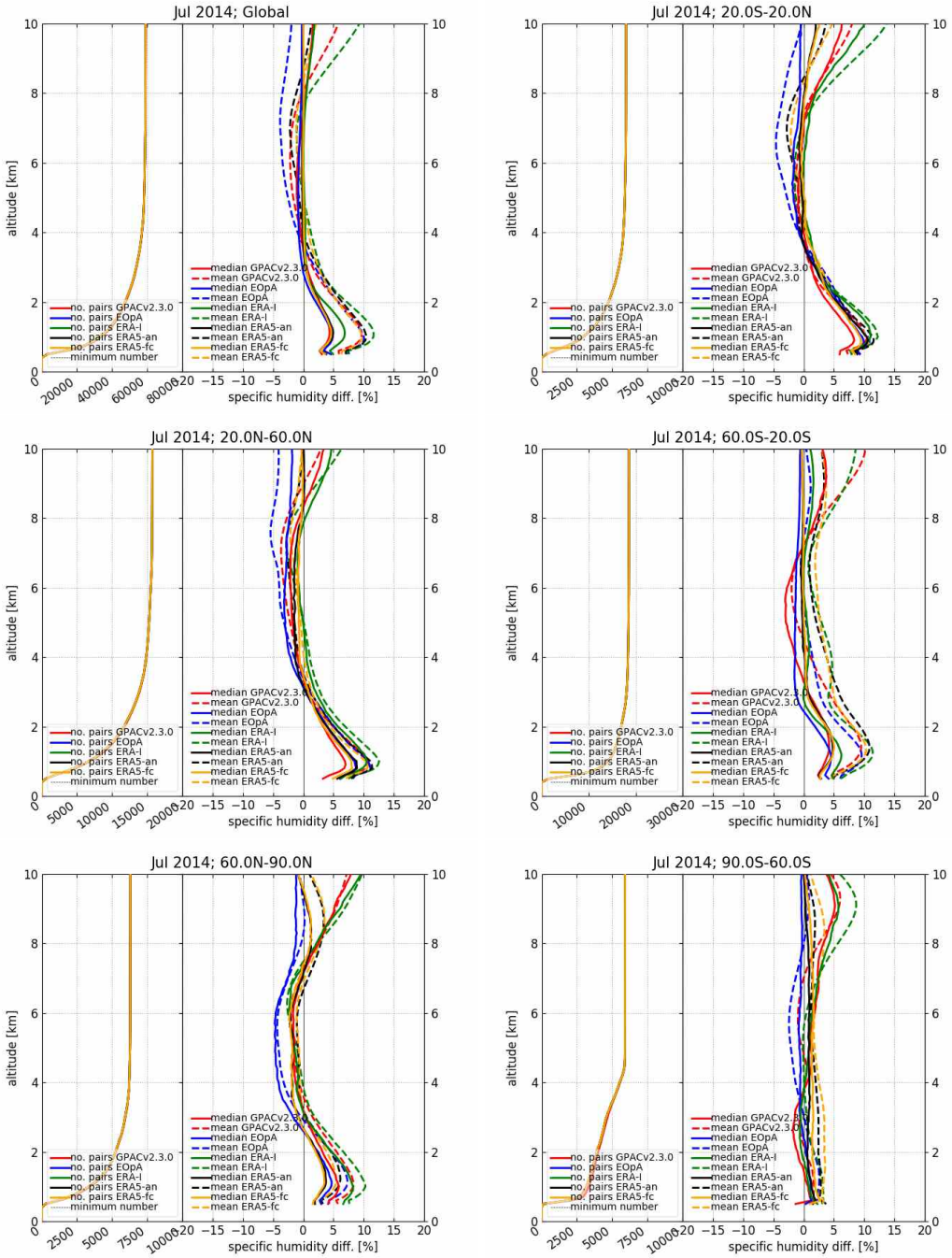

Figure A.15: *Specific humidity comparison for July 2014; top left panel: global; top right: tropics (20°S to 20°N); middle left: northern hemisphere mid-latitudes and subtropics (20°N to 60°N); middle right: southern hemisphere mid-latitudes and subtropics (20°S to 60°S); bottom left: northern hemisphere polar (60°N to 90°N); bottom right: southern hemisphere polar (60°S to 90°S)*

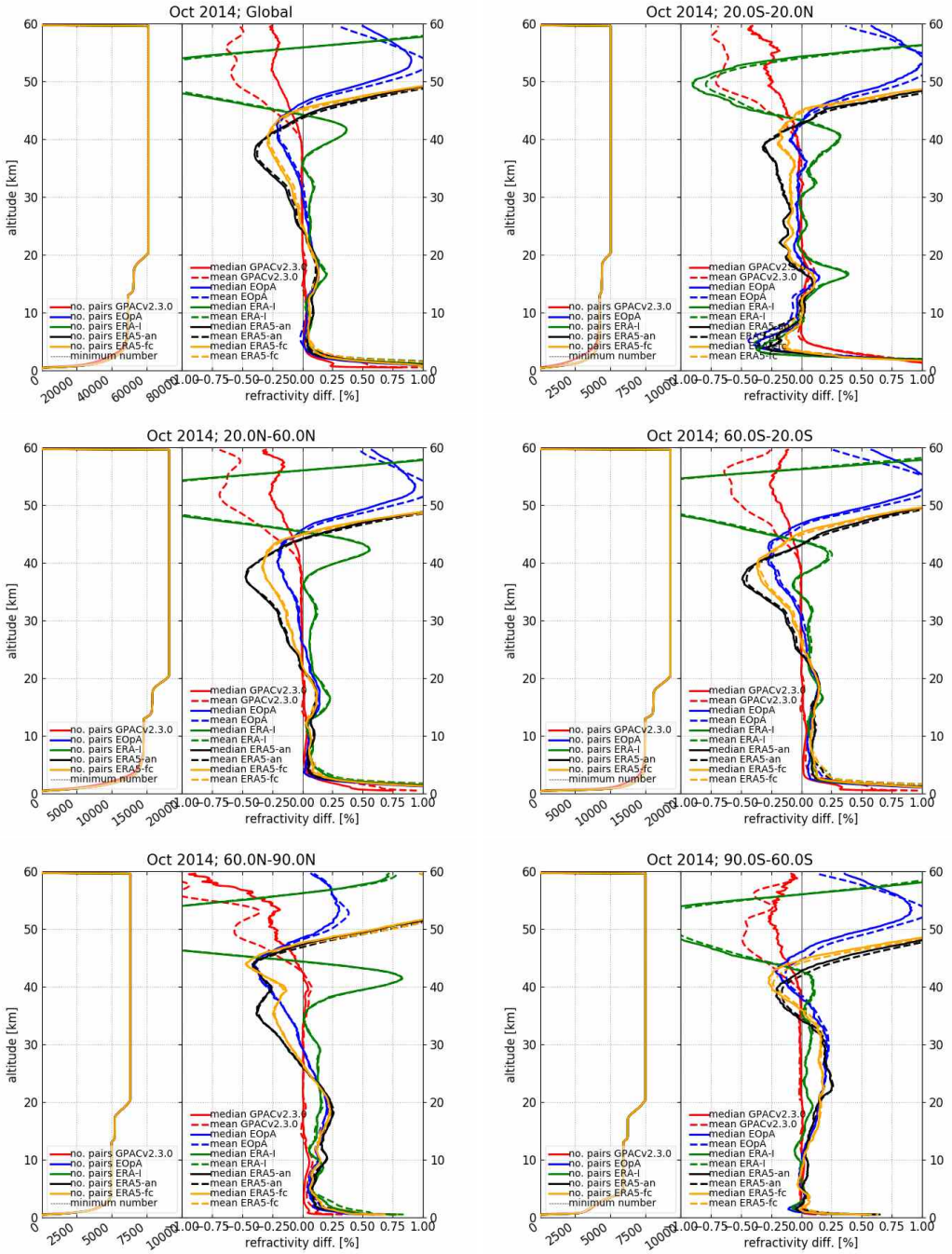

Figure A.16: *Refractivity comparison for October 2014; top left panel: global; top right: tropics (20°S to 20°N); middle left: northern hemisphere mid-latitudes and subtropics (20°N to 60°N); middle right: southern hemisphere mid-latitudes and subtropics (20°S to 60°S); bottom left: northern hemisphere polar (60°N to 90°N); bottom right: southern hemisphere polar (60°S to 90°S)*

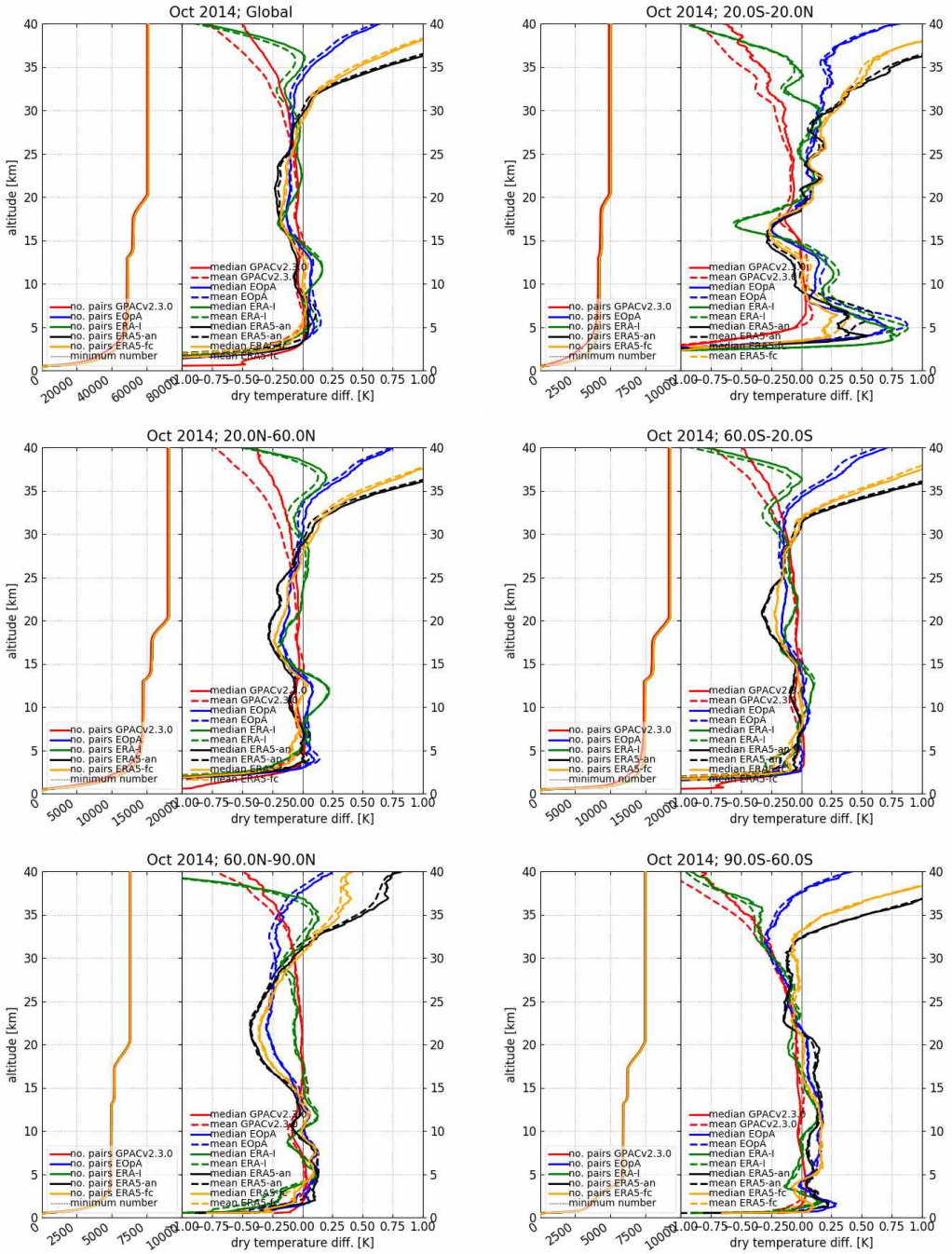

Figure A.17: *Dry temperature comparison for October 2014; top left panel: global; top right: tropics (20°S to 20°N); middle left: northern hemisphere mid-latitudes and subtropics (20°N to 60°N); middle right: southern hemisphere mid-latitudes and subtropics (20°S to 60°S); bottom left: northern hemisphere polar (60°N to 90°N); bottom right: southern hemisphere polar (60°S to 90°S)*

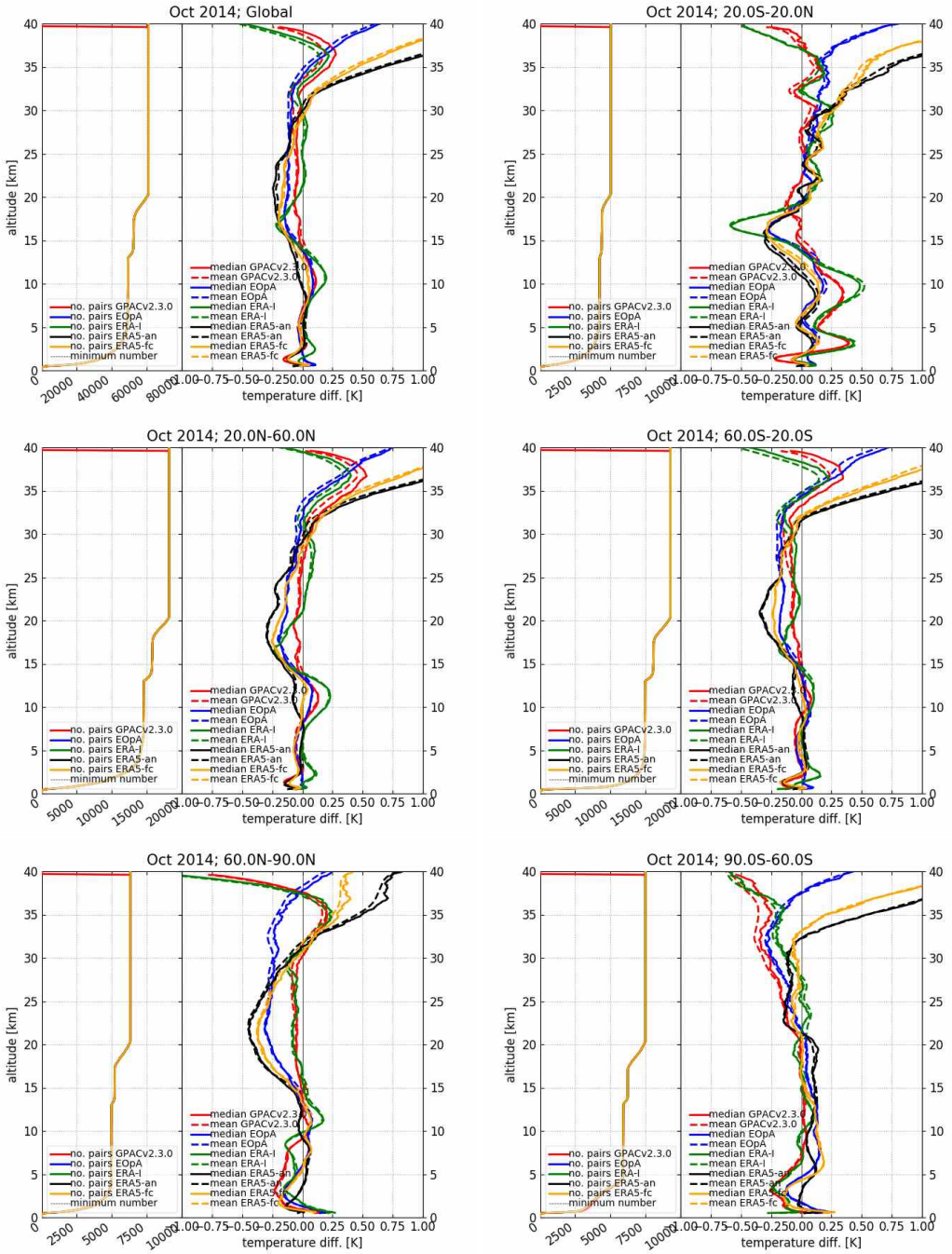

Figure A.18: *Temperature comparison for October 2014; top left panel: global; top right: tropics (20°S to 20°N); middle left: northern hemisphere mid-latitudes and subtropics (20°N to 60°N); middle right: southern hemisphere mid-latitudes and subtropics (20°S to 60°S); bottom left: northern hemisphere polar (60°N to 90°N); bottom right: southern hemisphere polar (60°S to 90°S)*

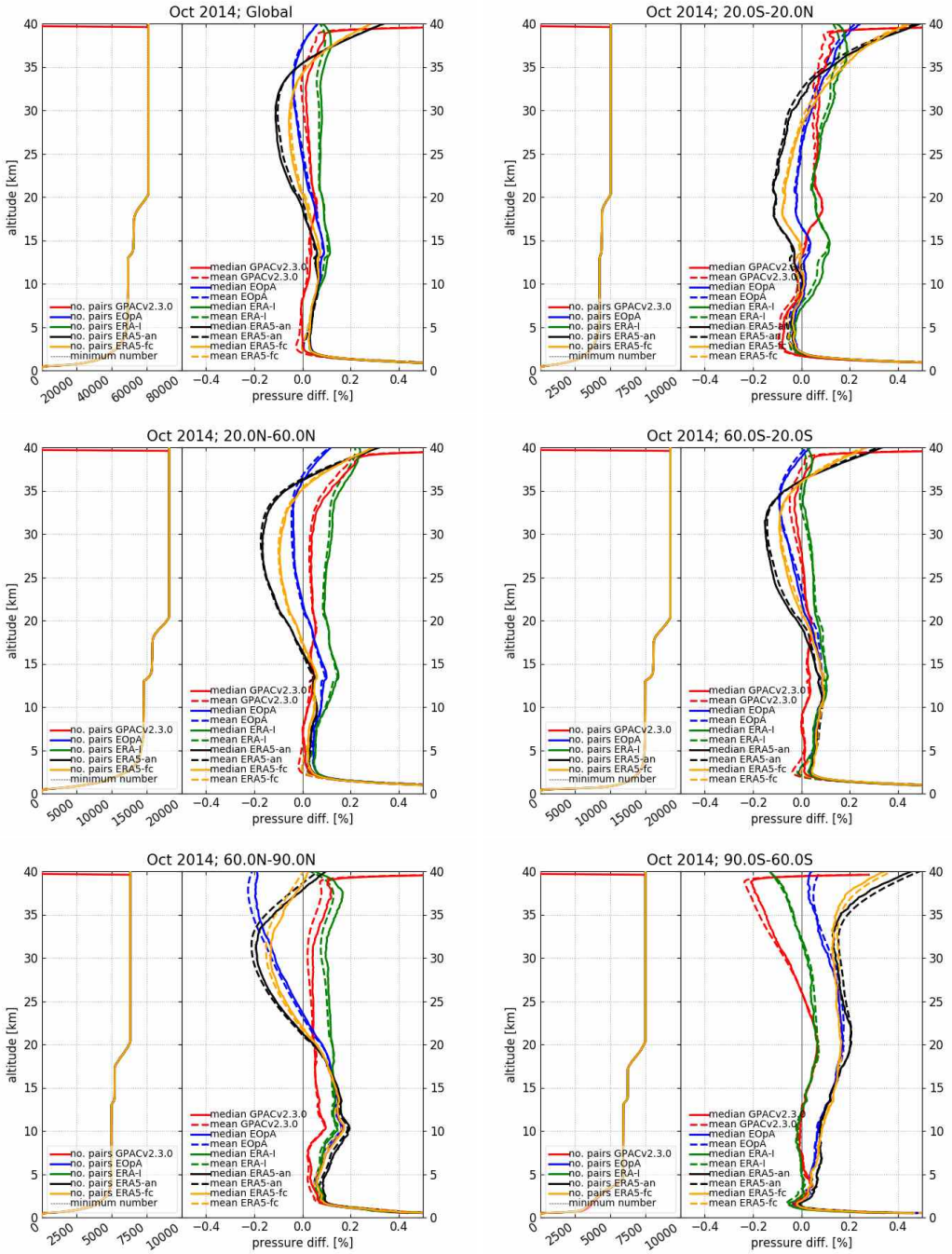

Figure A.19: *Pressure comparison for October 2014; top left panel: global; top right: tropics (20°S to 20°N); middle left: northern hemisphere mid-latitudes and subtropics (20°N to 60°N); middle right: southern hemisphere mid-latitudes and subtropics (20°S to 60°S); bottom left: northern hemisphere polar (60°N to 90°N); bottom right: southern hemisphere polar (60°S to 90°S)*

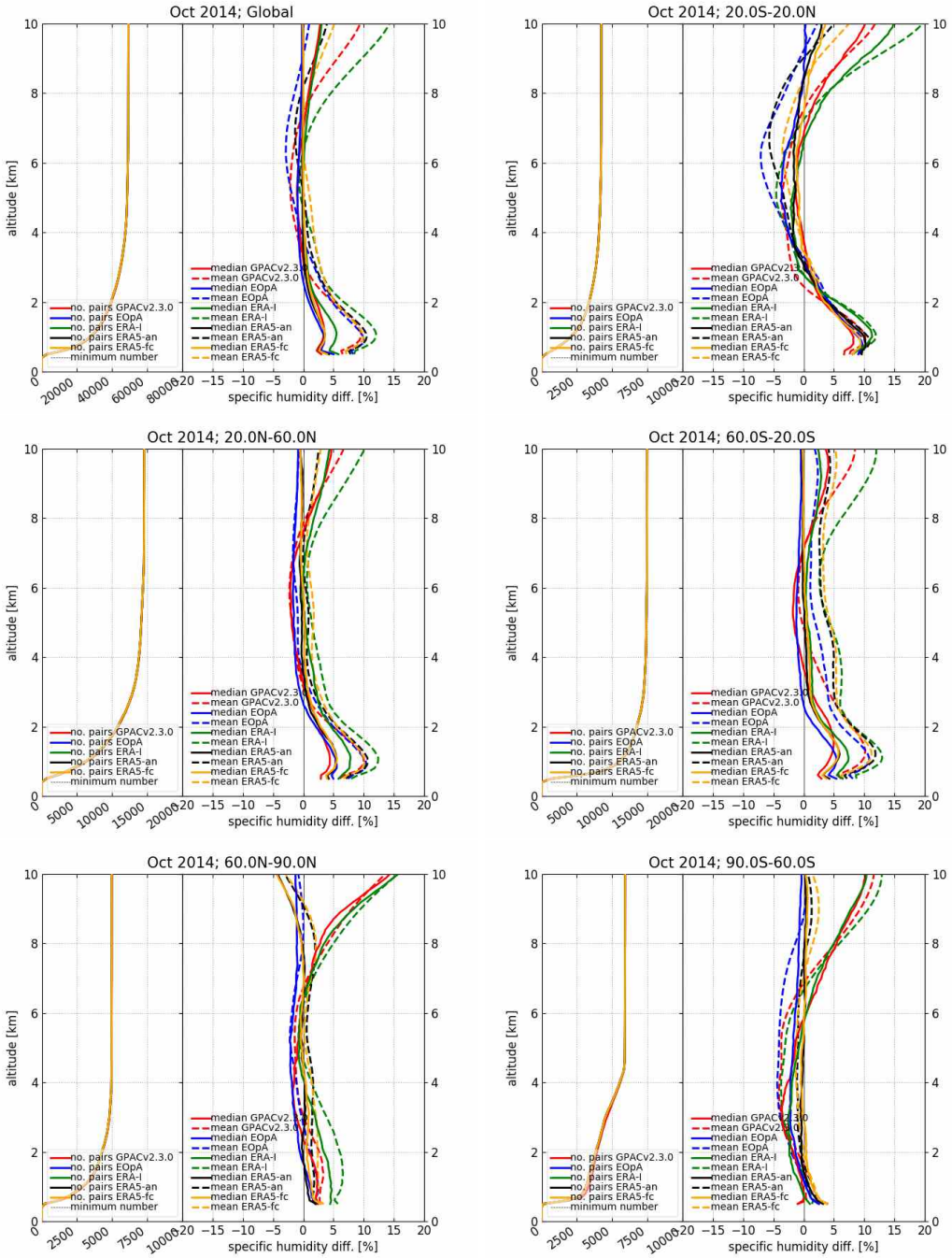

Figure A.20: *Specific humidity comparison for October 2014; top left panel: global; top right: tropics (20°S to 20°N); middle left: northern hemisphere mid-latitudes and subtropics (20°N to 60°N); middle right: southern hemisphere mid-latitudes and subtropics (20°S to 60°S); bottom left: northern hemisphere polar (60°N to 90°N); bottom right: southern hemisphere polar (60°S to 90°S)*

B Median, Mean, and 10% and 90% Percentiles

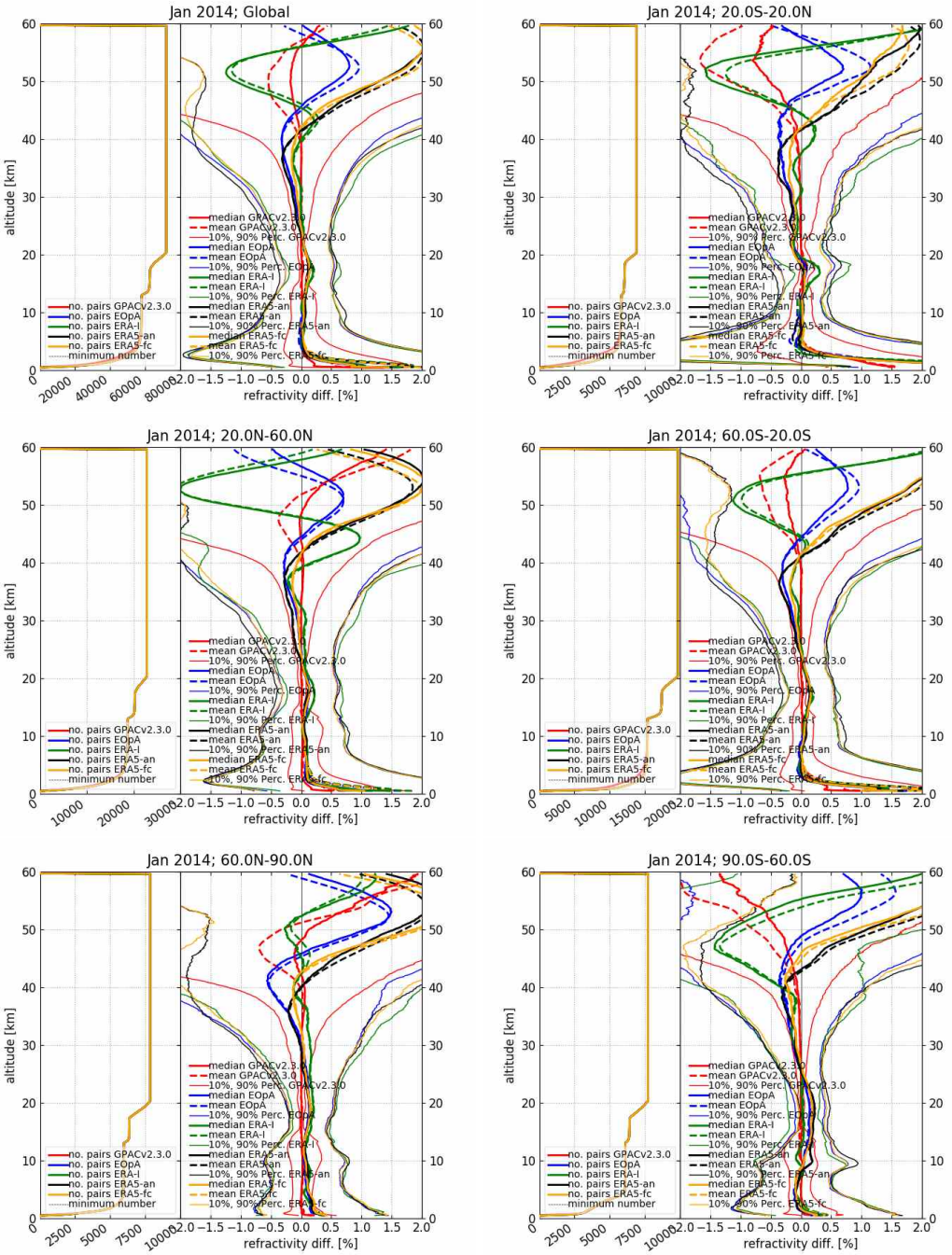

Figure B.1: *Refractivity comparison for January 2014; top left panel: global; top right: tropics (20°S to 20°N); middle left: northern hemisphere mid-latitudes and subtropics (20°N to 60°N); middle right: southern hemisphere mid-latitudes and subtropics (20°S to 60°S); bottom left: northern hemisphere polar (60°N to 90°N); bottom right: southern hemisphere polar (60°S to 90°S)*

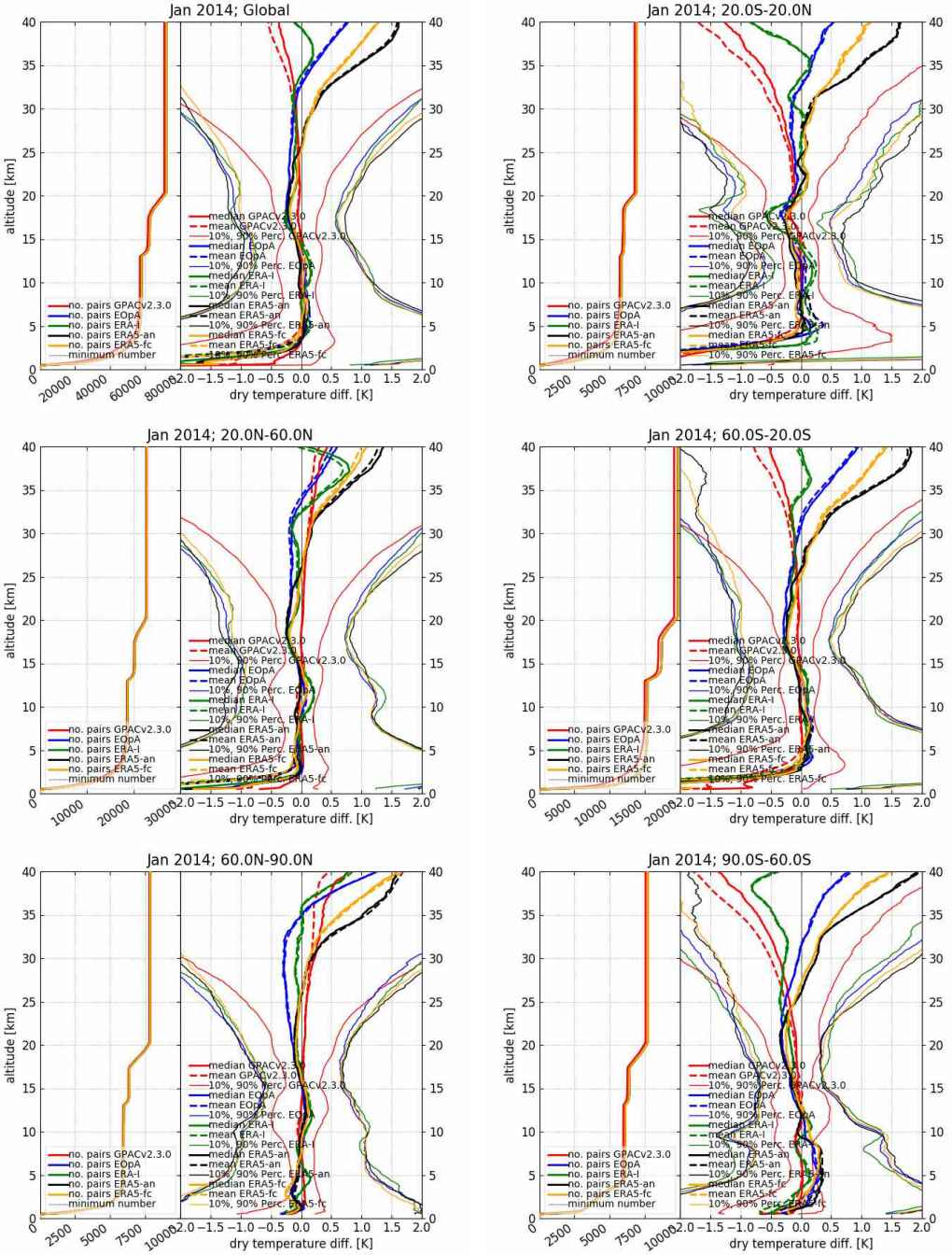

Figure B.2: *Dry temperature comparison for January 2014; top left panel: global; top right: tropics (20°S to 20°N); middle left: northern hemisphere mid-latitudes and subtropics (20°N to 60°N); middle right: southern hemisphere mid-latitudes and subtropics (20°S to 60°S); bottom left: northern hemisphere polar (60°N to 90°N); bottom right: southern hemisphere polar (60°S to 90°S)*

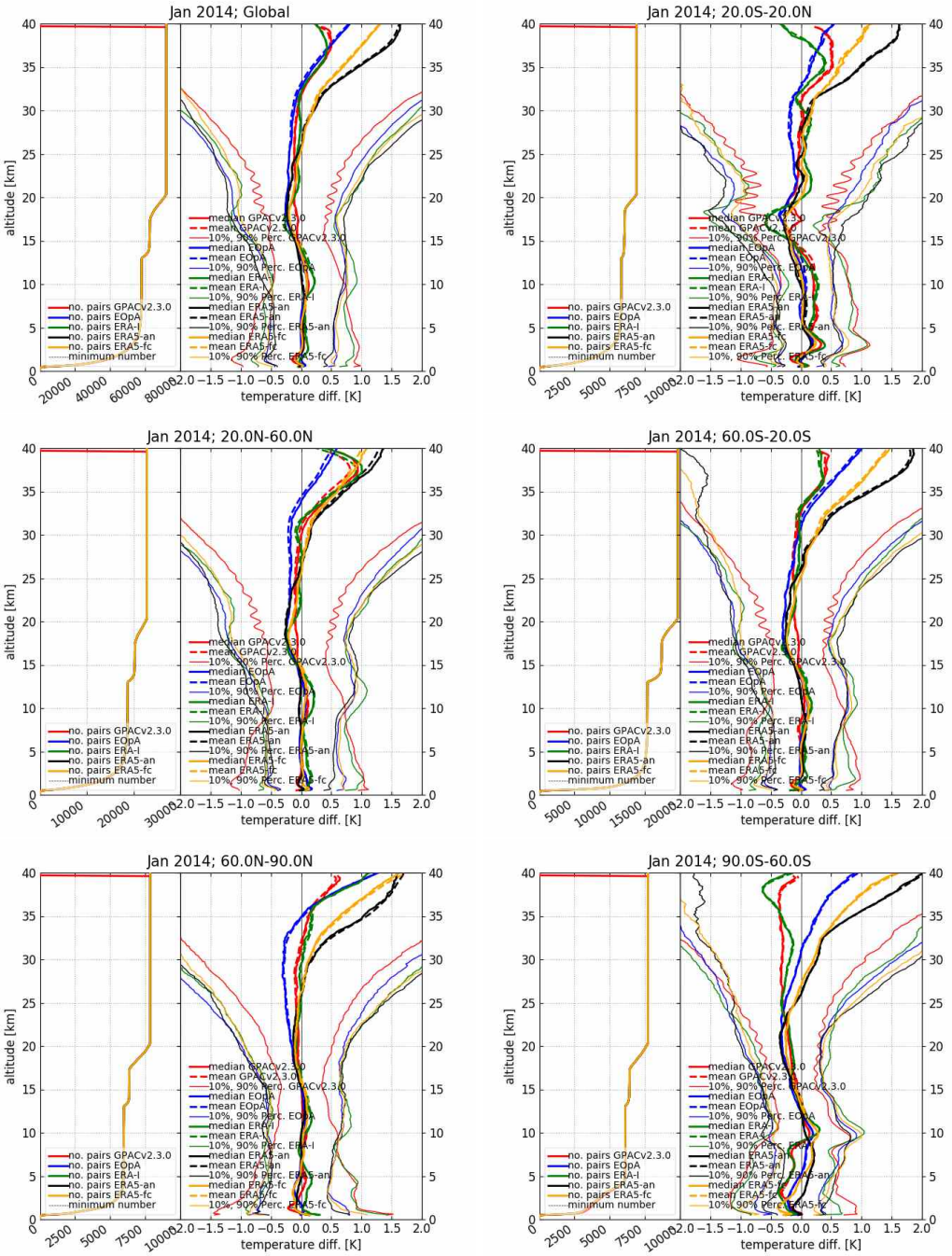

Figure B.3: *Temperature comparison for January 2014; top left panel: global; top right: tropics (20°S to 20°N); middle left: northern hemisphere mid-latitudes and subtropics (20°N to 60°N); middle right: southern hemisphere mid-latitudes and subtropics (20°S to 60°S); bottom left: northern hemisphere polar (60°N to 90°N); bottom right: southern hemisphere polar (60°S to 90°S)*

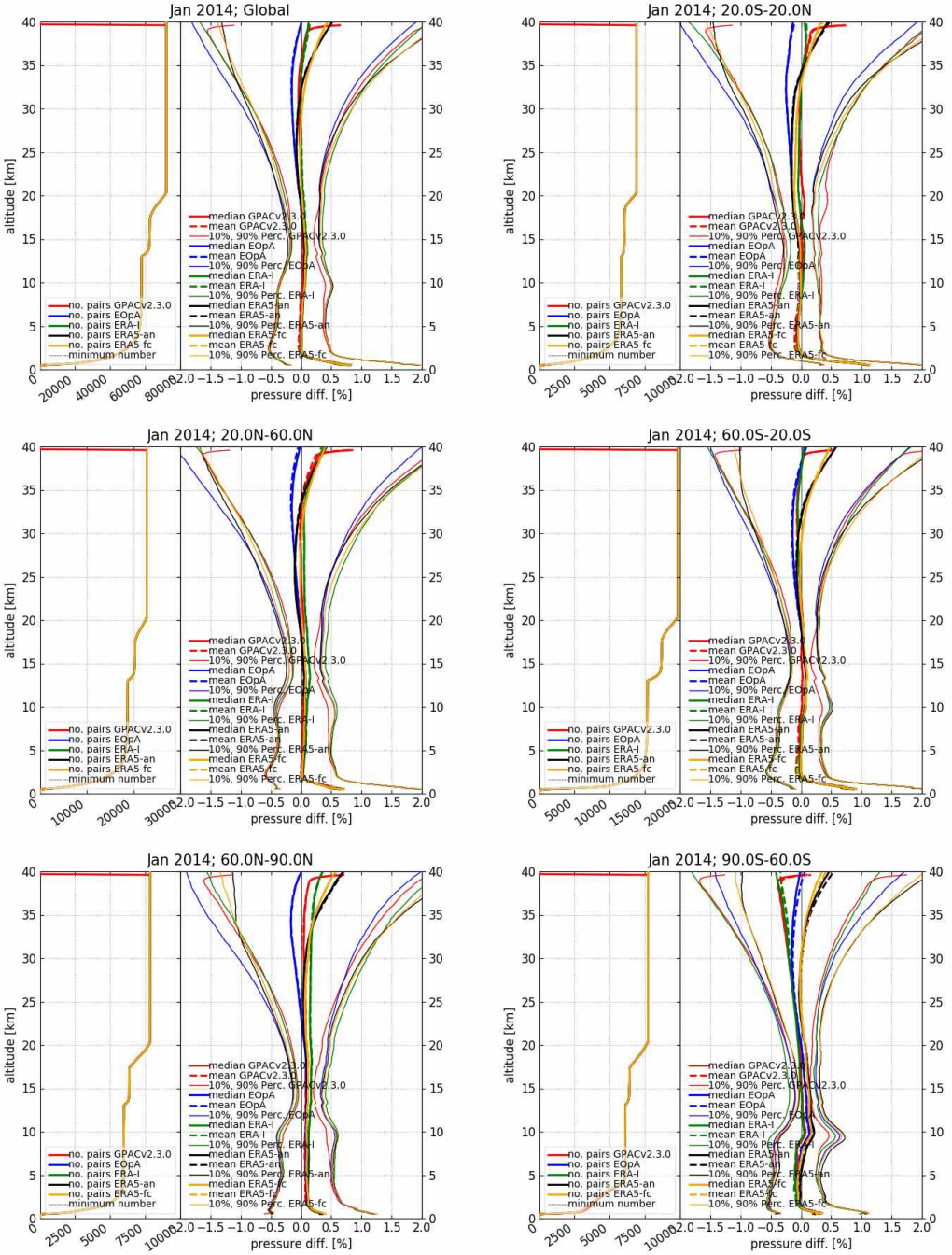

Figure B.4: *Pressure comparison for January 2014; top left panel: global; top right: tropics (20°S to 20°N); middle left: northern hemisphere mid-latitudes and subtropics (20°N to 60°N); middle right: southern hemisphere mid-latitudes and subtropics (20°S to 60°S); bottom left: northern hemisphere polar (60°N to 90°N); bottom right: southern hemisphere polar (60°S to 90°S)*

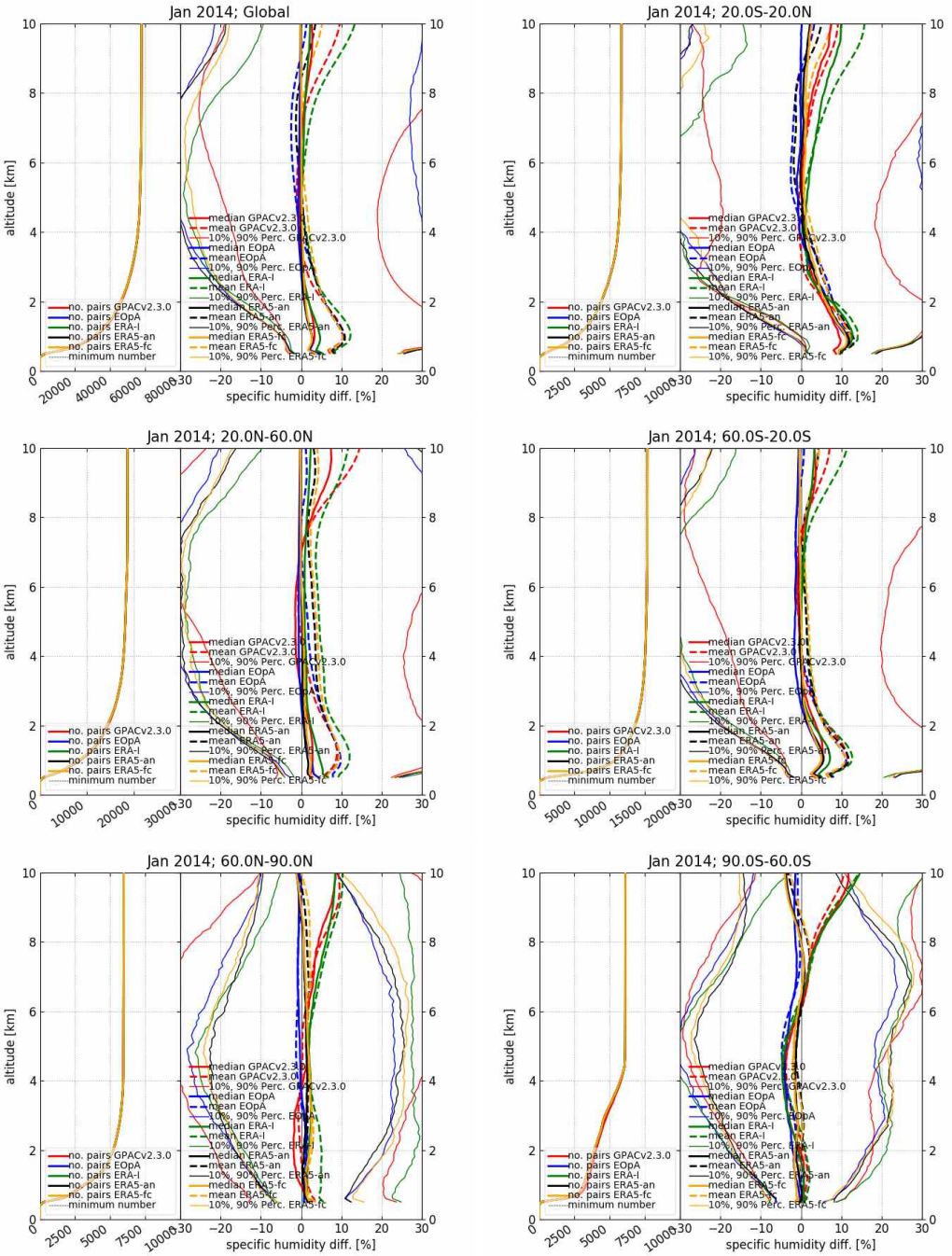

Figure B.5: *Specific humidity comparison for January 2014; top left panel: global; top right: tropics (20°S to 20°N); middle left: northern hemisphere mid-latitudes and subtropics (20°N to 60°N); middle right: southern hemisphere mid-latitudes and subtropics (20°S to 60°S); bottom left: northern hemisphere polar (60°N to 90°N); bottom right: southern hemisphere polar (60°S to 90°S)*

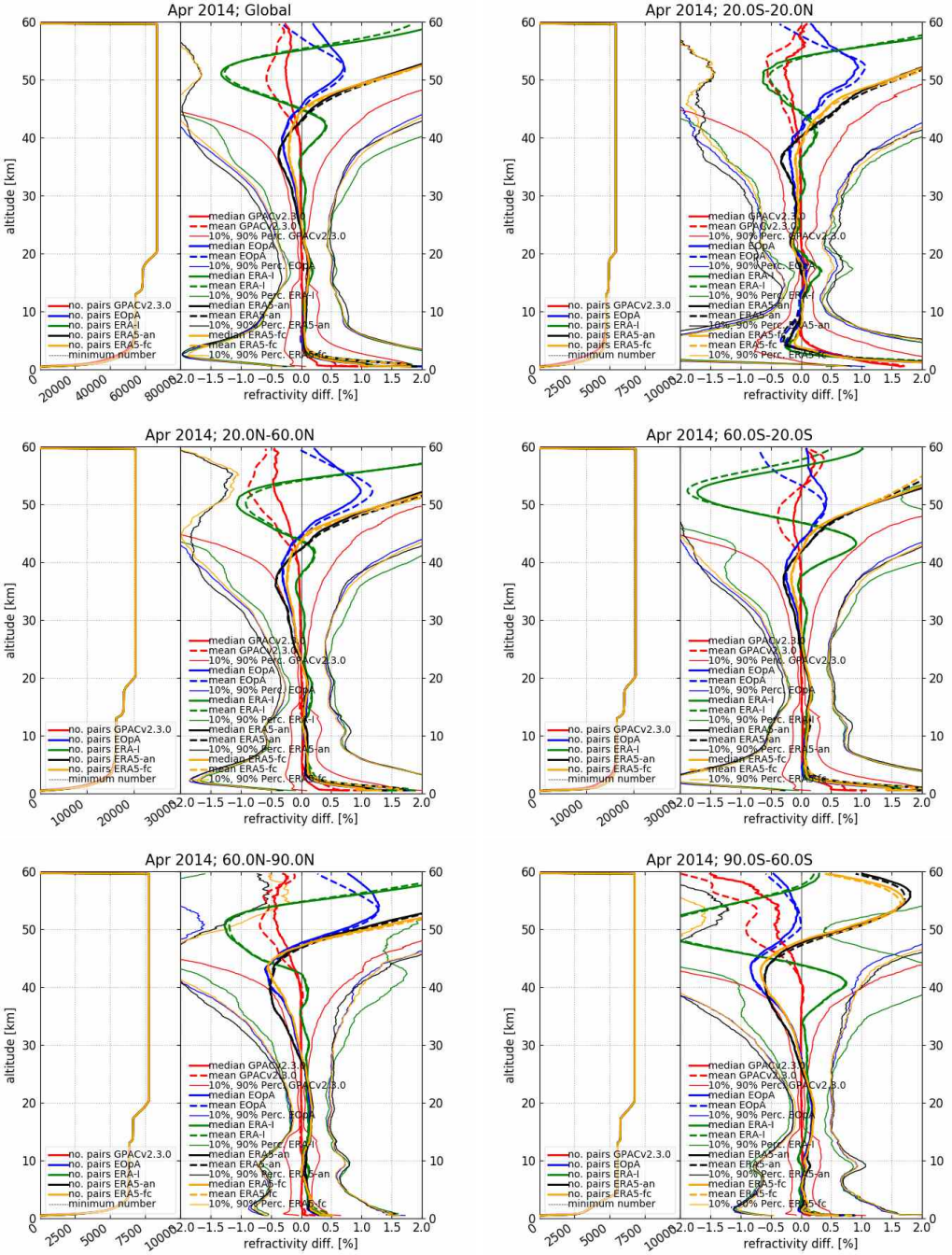

Figure B.6: *Refractivity comparison for April 2014; top left panel: global; top right: tropics (20°S to 20°N); middle left: northern hemisphere mid-latitudes and subtropics (20°N to 60°N); middle right: southern hemisphere mid-latitudes and subtropics (20°S to 60°S); bottom left: northern hemisphere polar (60°N to 90°N); bottom right: southern hemisphere polar (60°S to 90°S)*

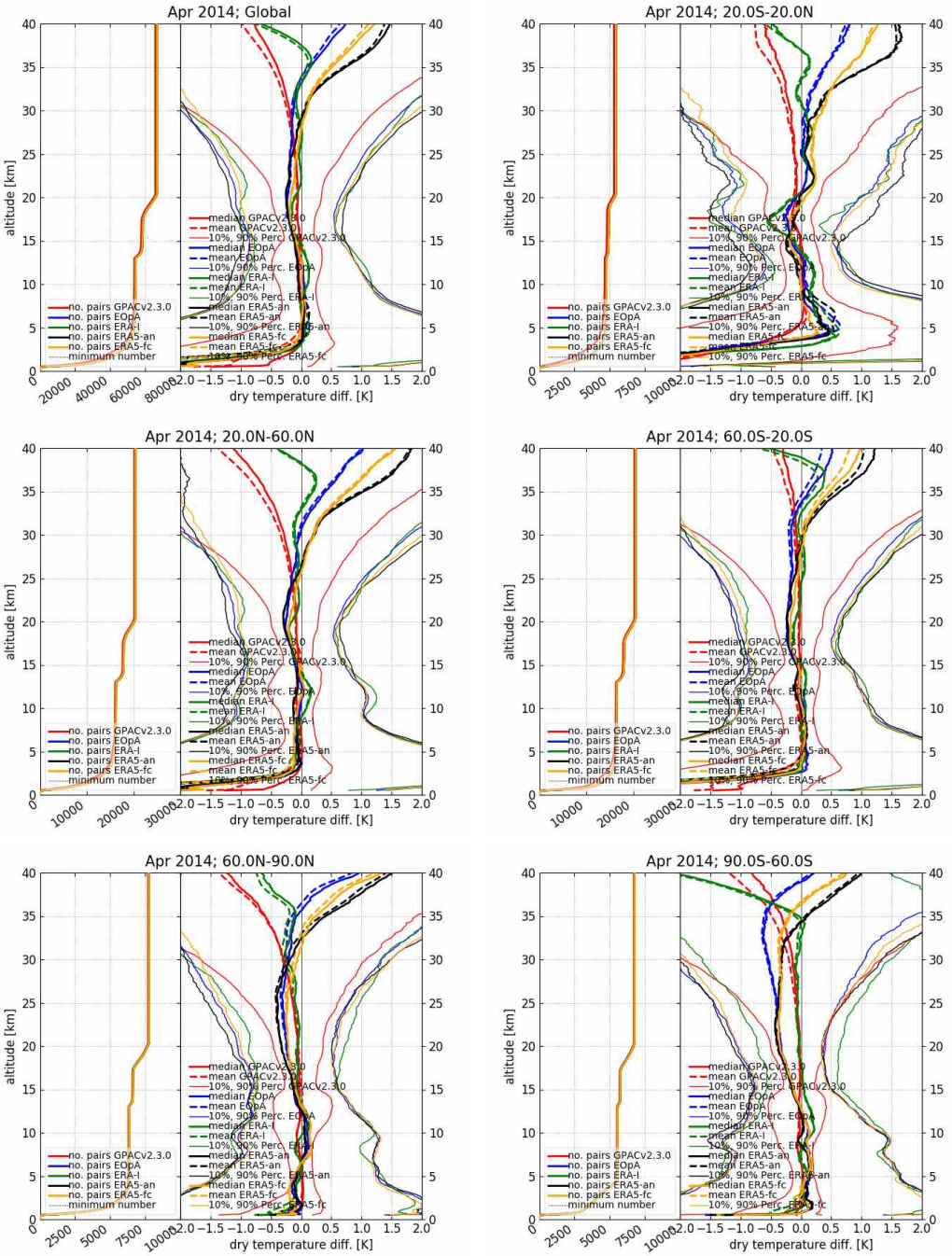

Figure B.7: *Dry temperature comparison for April 2014; top left panel: global; top right: tropics (20°S to 20°N); middle left: northern hemisphere mid-latitudes and subtropics (20°N to 60°N); middle right: southern hemisphere mid-latitudes and subtropics (20°S to 60°S); bottom left: northern hemisphere polar (60°N to 90°N); bottom right: southern hemisphere polar (60°S to 90°S)*

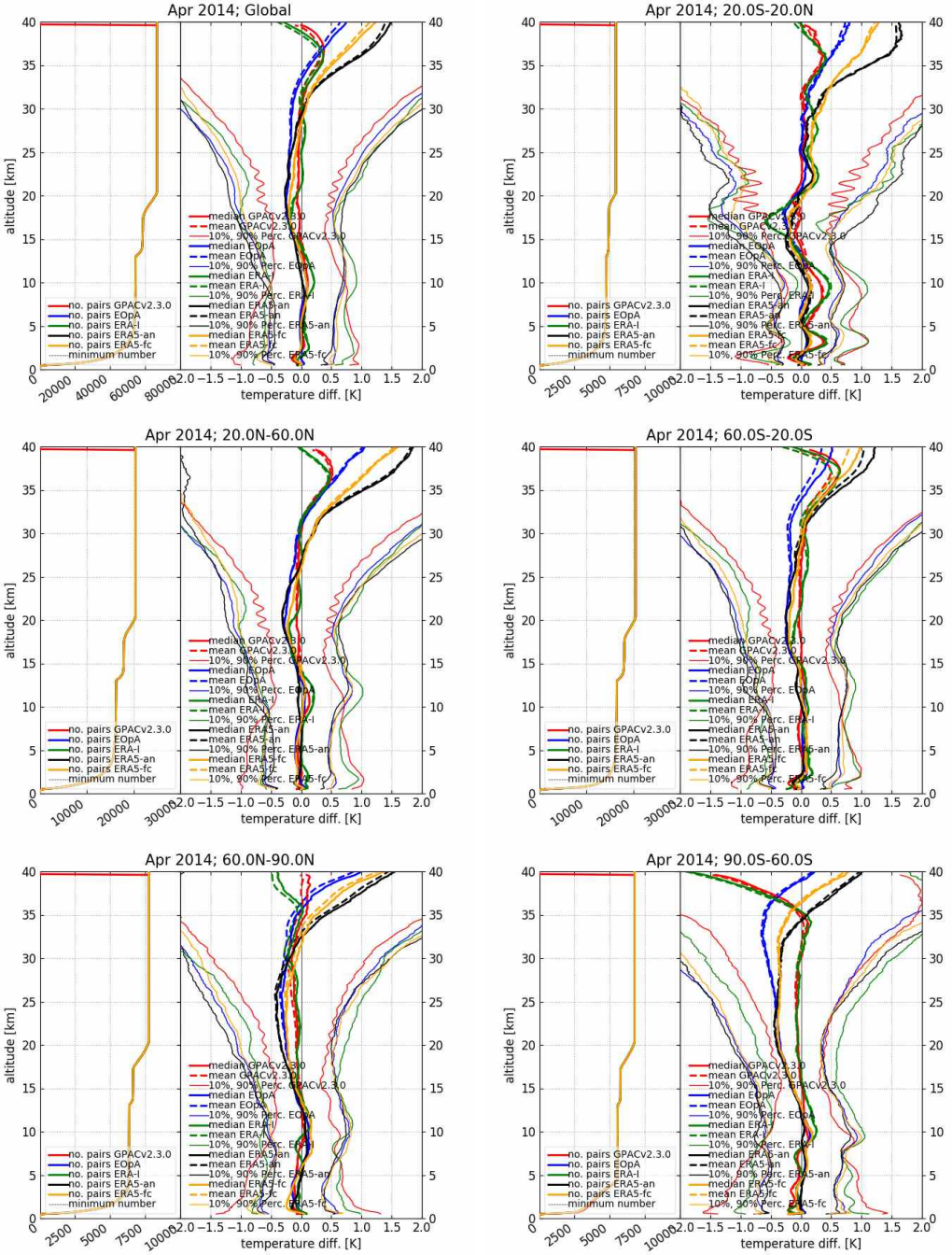

Figure B.8: *Temperature comparison for April 2014; top left panel: global; top right: tropics (20°S to 20°N); middle left: northern hemisphere mid-latitudes and subtropics (20°N to 60°N); middle right: southern hemisphere mid-latitudes and subtropics (20°S to 60°S); bottom left: northern hemisphere polar (60°N to 90°N); bottom right: southern hemisphere polar (60°S to 90°S)*

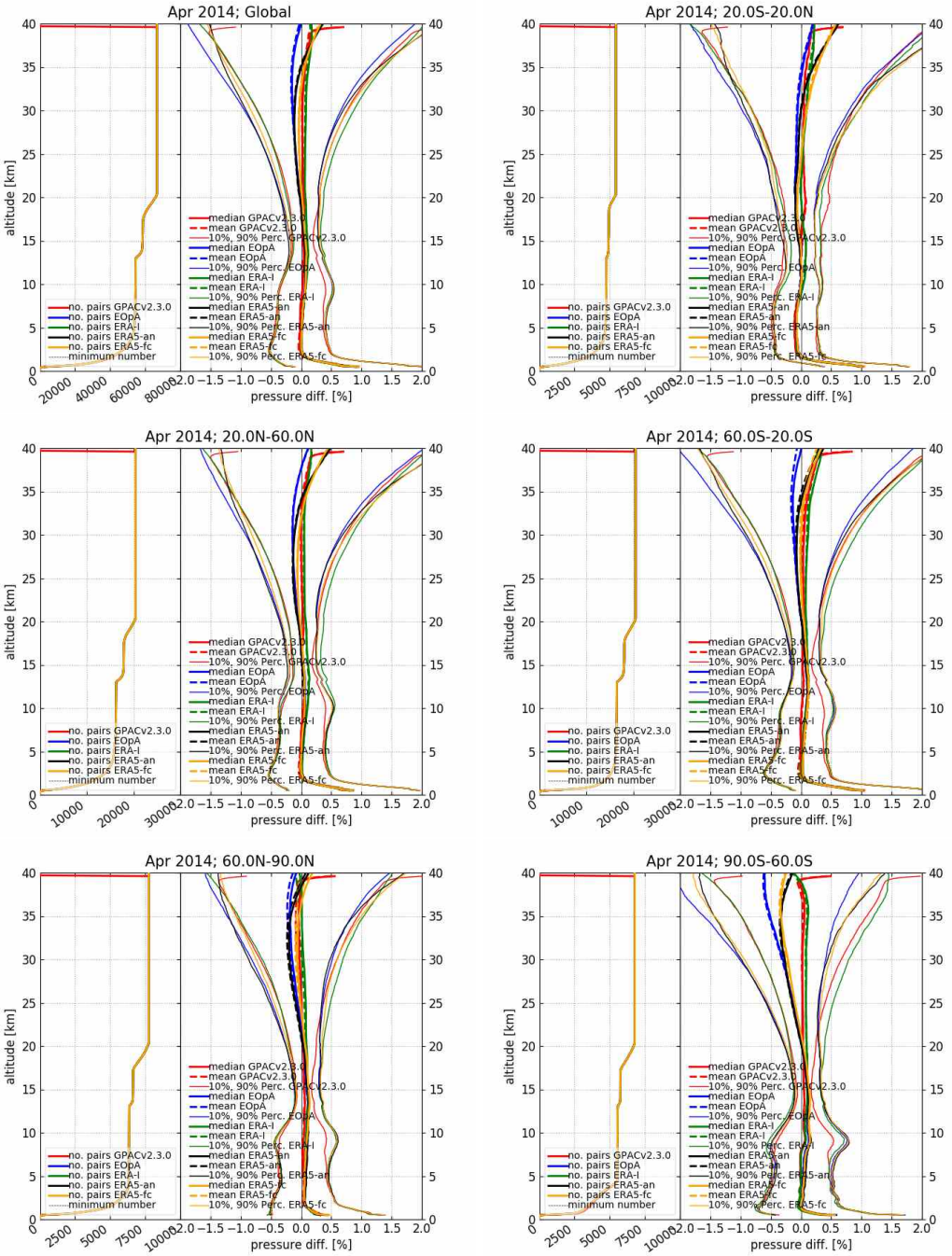

Figure B.9: *Pressure comparison for April 2014; top left panel: global; top right: tropics (20°S to 20°N); middle left: northern hemisphere mid-latitudes and subtropics (20°N to 60°N); middle right: southern hemisphere mid-latitudes and subtropics (20°S to 60°S); bottom left: northern hemisphere polar (60°N to 90°N); bottom right: southern hemisphere polar (60°S to 90°S)*

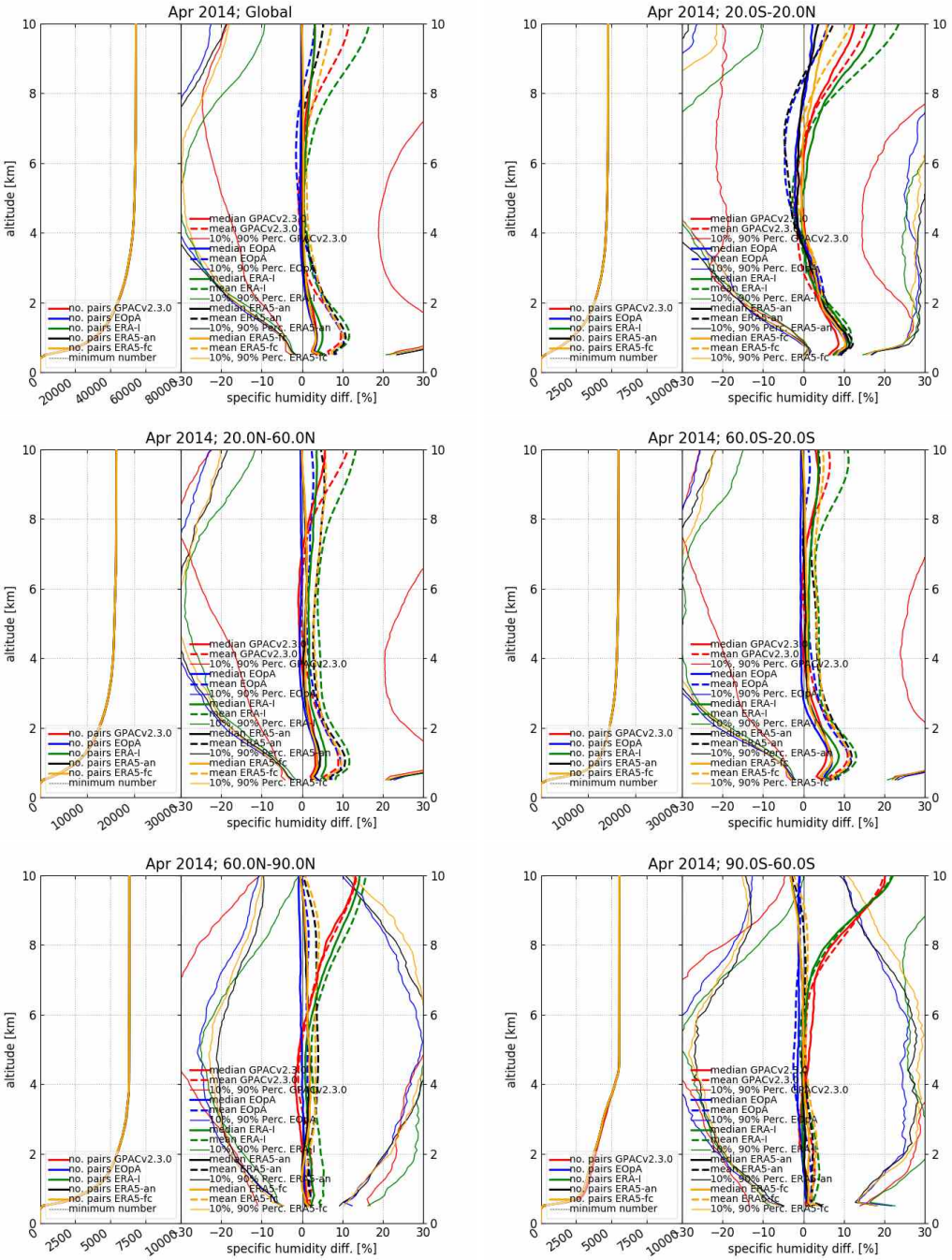

Figure B.10: *Specific humidity comparison for April 2014; top left panel: global; top right: tropics (20°S to 20°N); middle left: northern hemisphere mid-latitudes and subtropics (20°N to 60°N); middle right: southern hemisphere mid-latitudes and subtropics (20°S to 60°S); bottom left: northern hemisphere polar (60°N to 90°N); bottom right: southern hemisphere polar (60°S to 90°S)*

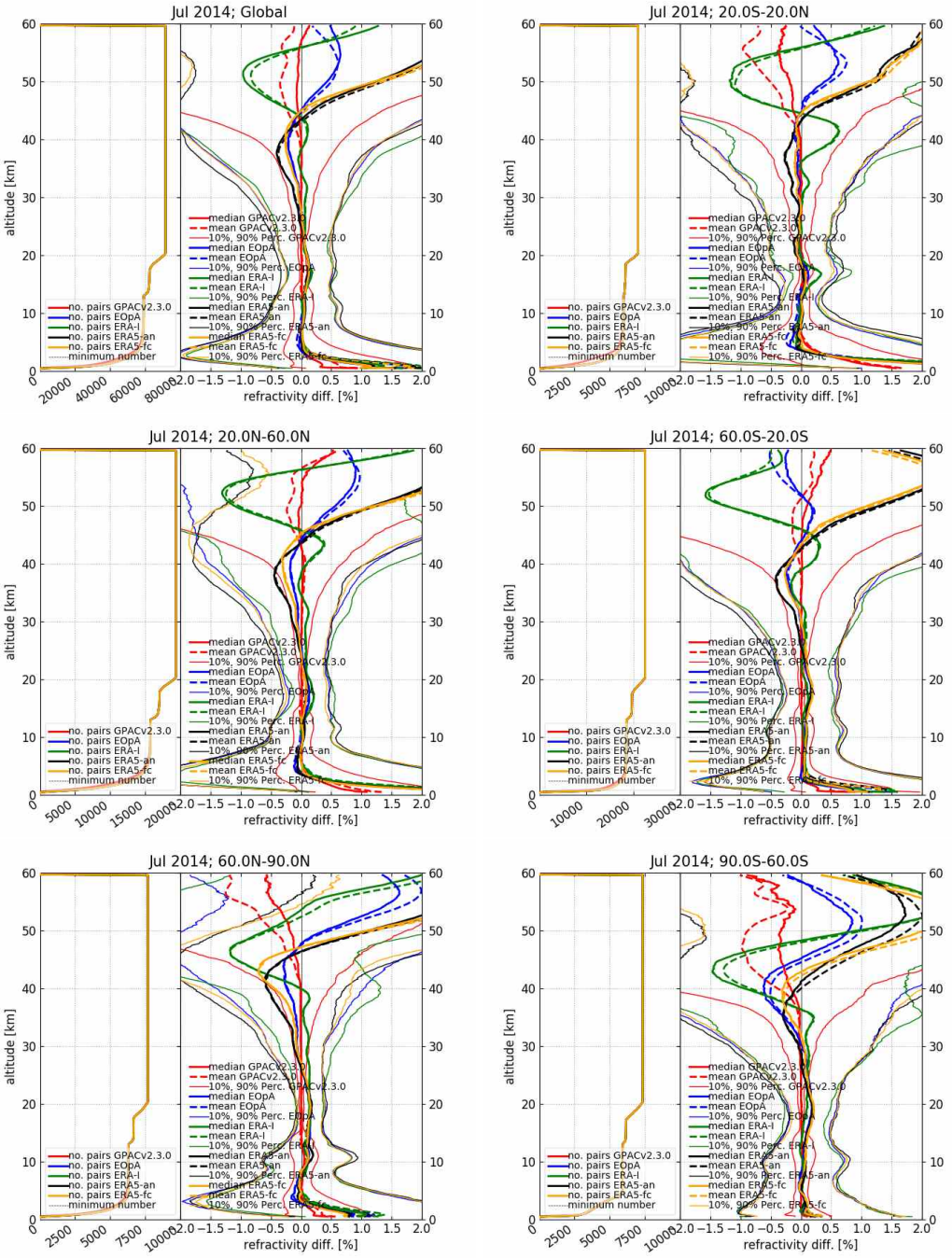

Figure B.11: *Refractivity comparison for July 2014; top left panel: global; top right: tropics (20°S to 20°N); middle left: northern hemisphere mid-latitudes and subtropics (20°N to 60°N); middle right: southern hemisphere mid-latitudes and subtropics (20°S to 60°S); bottom left: northern hemisphere polar (60°N to 90°N); bottom right: southern hemisphere polar (60°S to 90°S)*

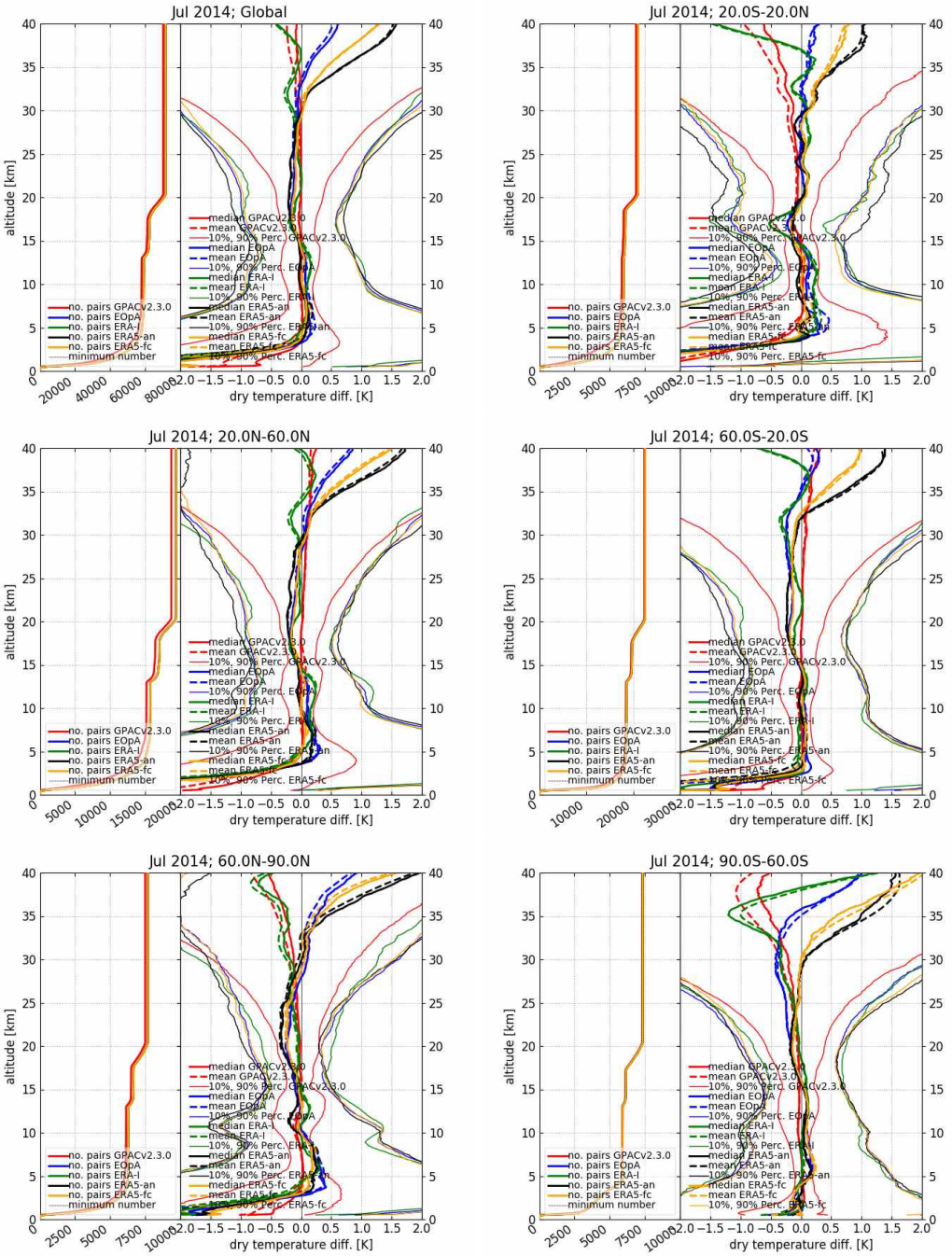

Figure B.12: *Dry temperature comparison for July 2014; top left panel: global; top right: tropics (20°S to 20°N); middle left: northern hemisphere mid-latitudes and subtropics (20°N to 60°N); middle right: southern hemisphere mid-latitudes and subtropics (20°S to 60°S); bottom left: northern hemisphere polar (60°N to 90°N); bottom right: southern hemisphere polar (60°S to 90°S)*

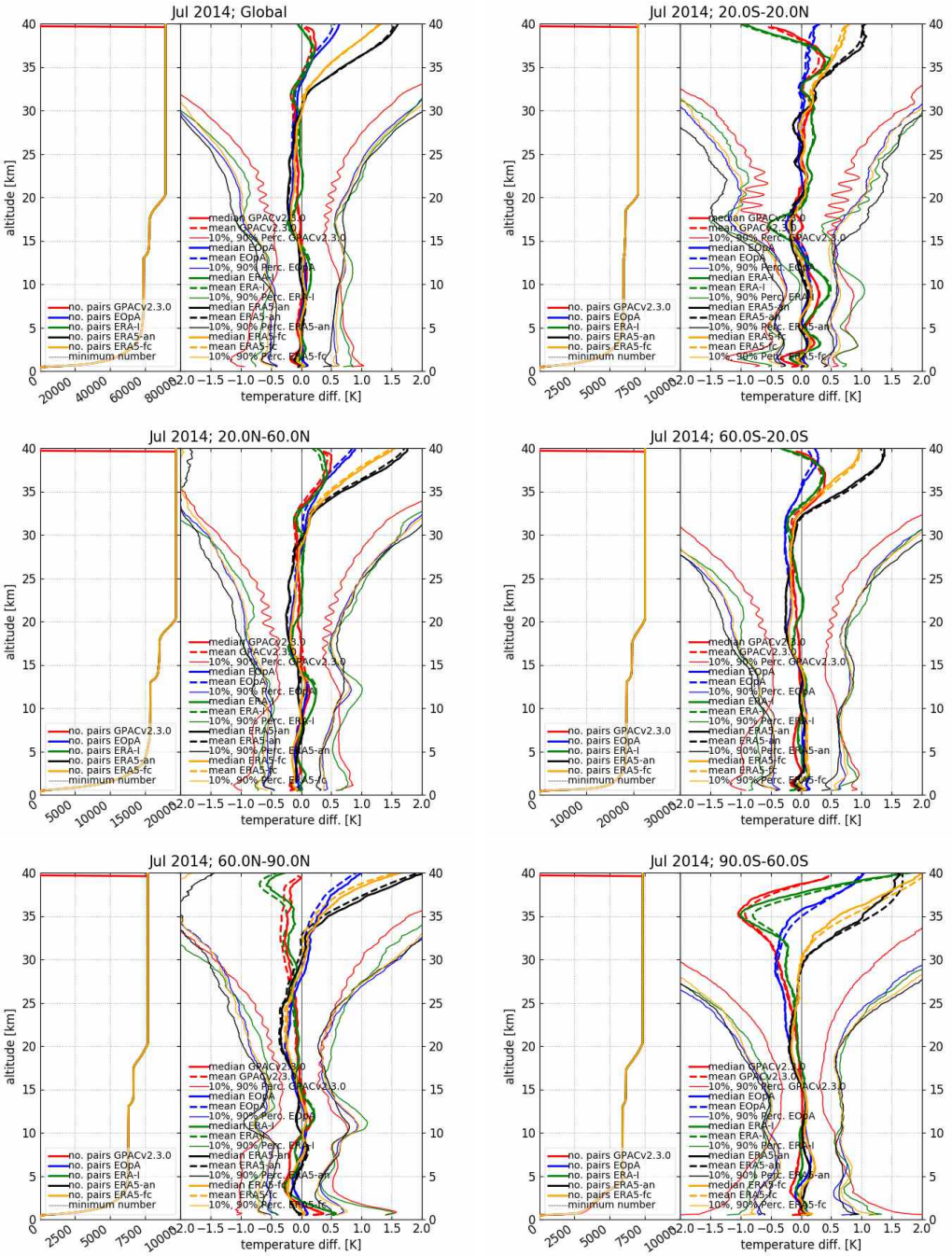

Figure B.13: *Temperature comparison for July 2014; top left panel: global; top right: tropics (20°S to 20°N); middle left: northern hemisphere mid-latitudes and subtropics (20°N to 60°N); middle right: southern hemisphere mid-latitudes and subtropics (20°S to 60°S); bottom left: northern hemisphere polar (60°N to 90°N); bottom right: southern hemisphere polar (60°S to 90°S)*

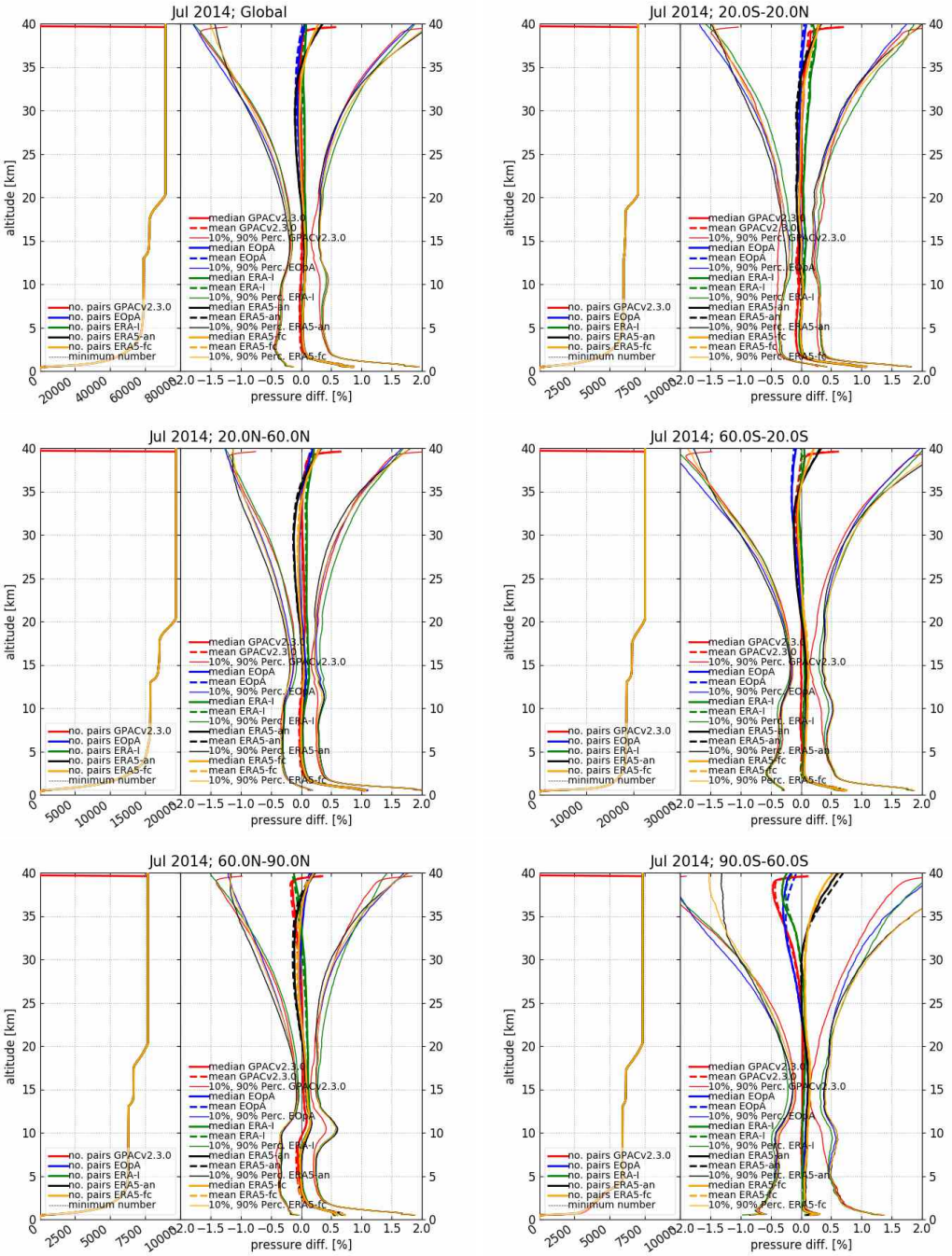

Figure B.14: *Pressure comparison for July 2014; top left panel: global; top right: tropics (20°S to 20°N); middle left: northern hemisphere mid-latitudes and subtropics (20°N to 60°N); middle right: southern hemisphere mid-latitudes and subtropics (20°S to 60°S); bottom left: northern hemisphere polar (60°N to 90°N); bottom right: southern hemisphere polar (60°S to 90°S)*

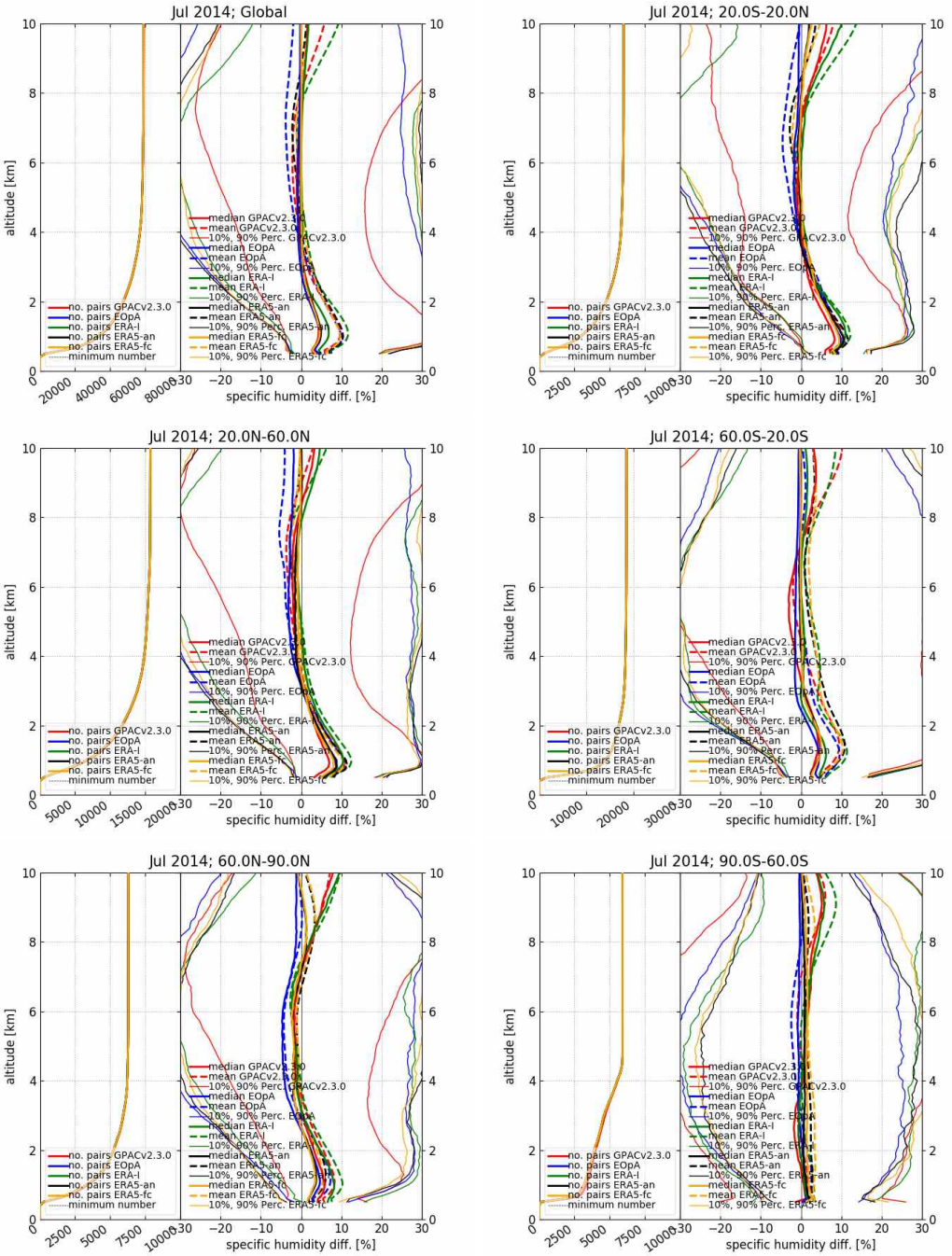

Figure B.15: *Specific humidity comparison for July 2014; top left panel: global; top right: tropics (20°S to 20°N); middle left: northern hemisphere mid-latitudes and subtropics (20°N to 60°N); middle right: southern hemisphere mid-latitudes and subtropics (20°S to 60°S); bottom left: northern hemisphere polar (60°N to 90°N); bottom right: southern hemisphere polar (60°S to 90°S)*

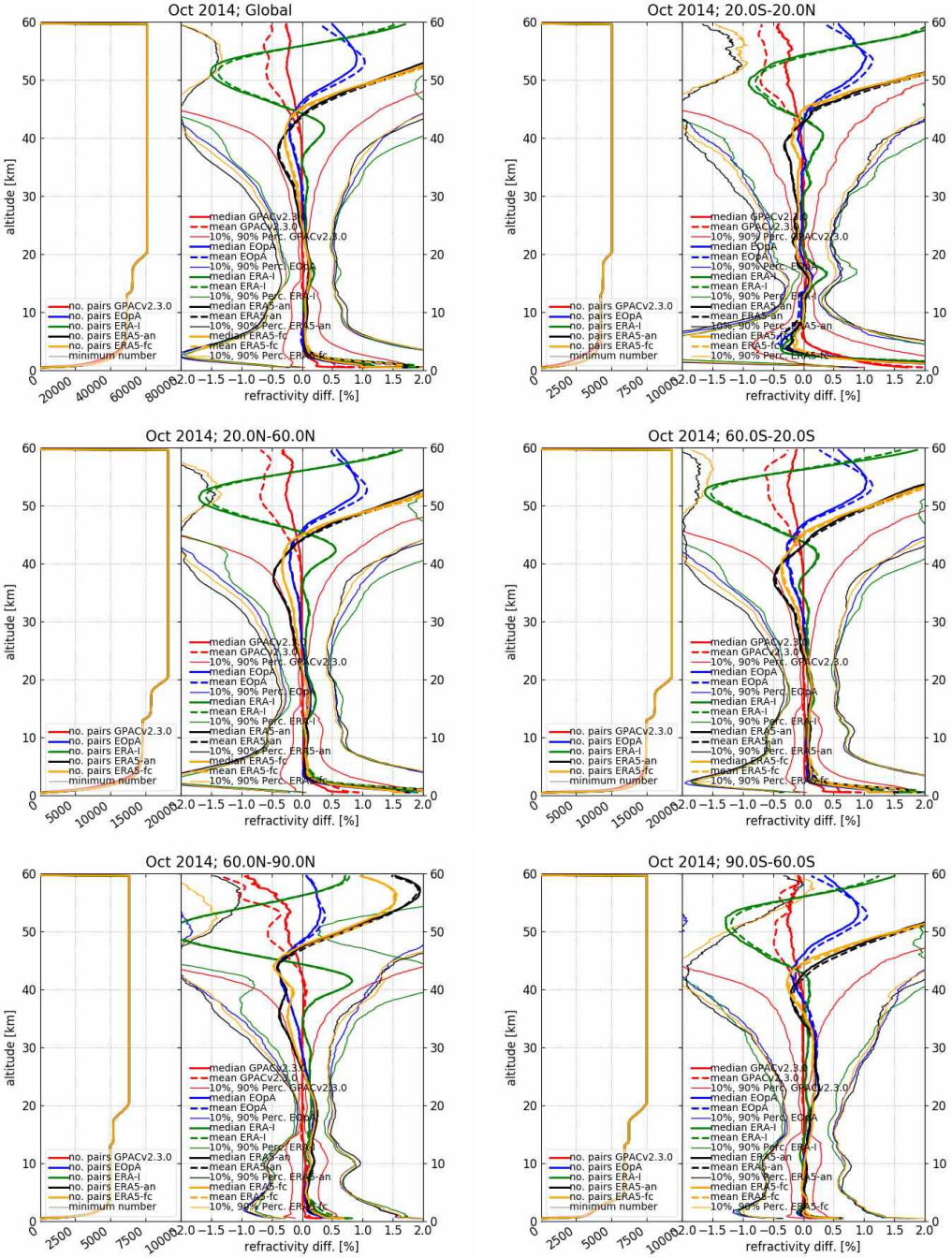

Figure B.16: *Refractivity comparison for October 2014; top left panel: global; top right: tropics (20°S to 20°N); middle left: northern hemisphere mid-latitudes and subtropics (20°N to 60°N); middle right: southern hemisphere mid-latitudes and subtropics (20°S to 60°S); bottom left: northern hemisphere polar (60°N to 90°N); bottom right: southern hemisphere polar (60°S to 90°S)*

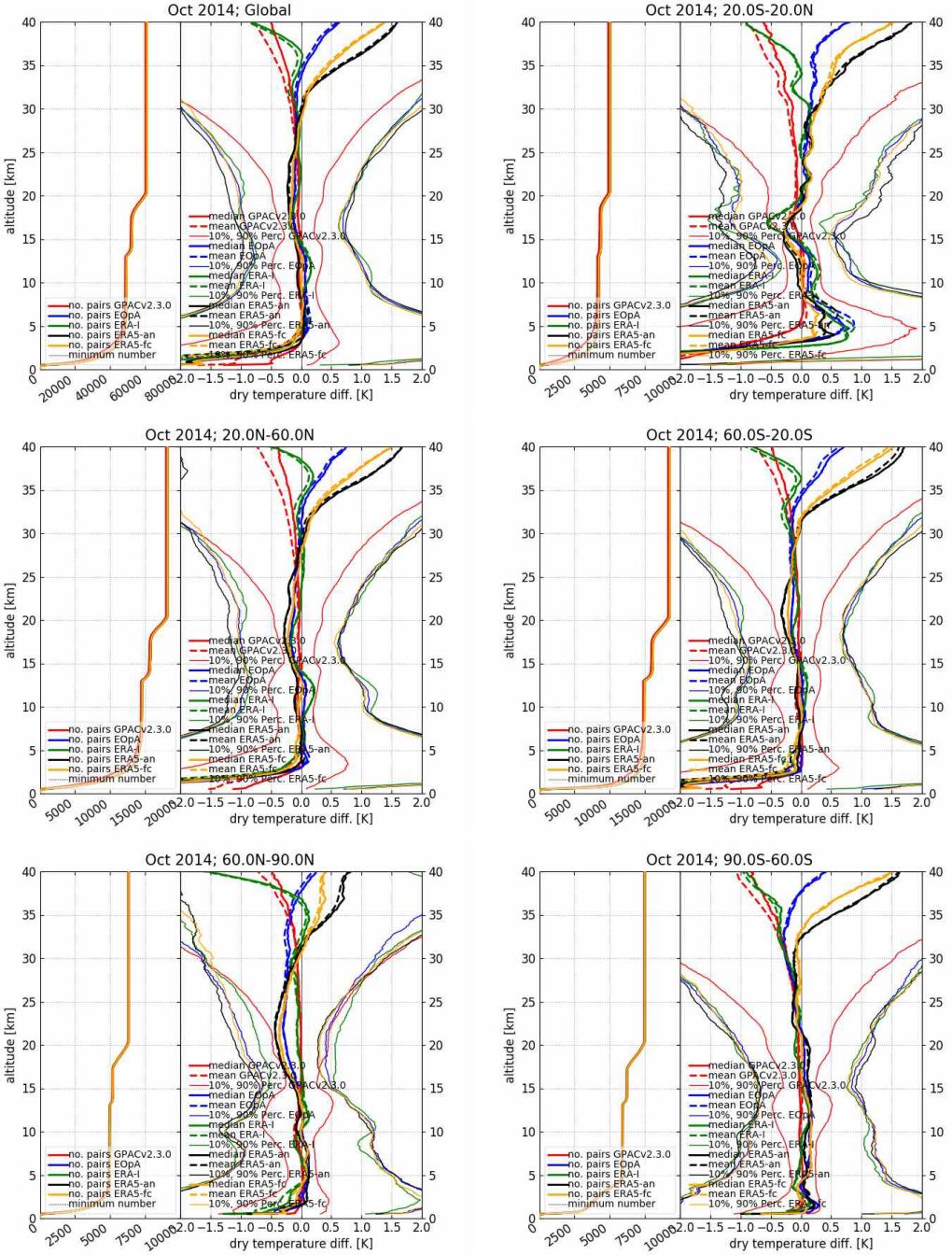

Figure B.17: *Dry temperature comparison for October 2014; top left panel: global; top right: tropics (20°S to 20°N); middle left: northern hemisphere mid-latitudes and subtropics (20°N to 60°N); middle right: southern hemisphere mid-latitudes and subtropics (20°S to 60°S); bottom left: northern hemisphere polar (60°N to 90°N); bottom right: southern hemisphere polar (60°S to 90°S)*

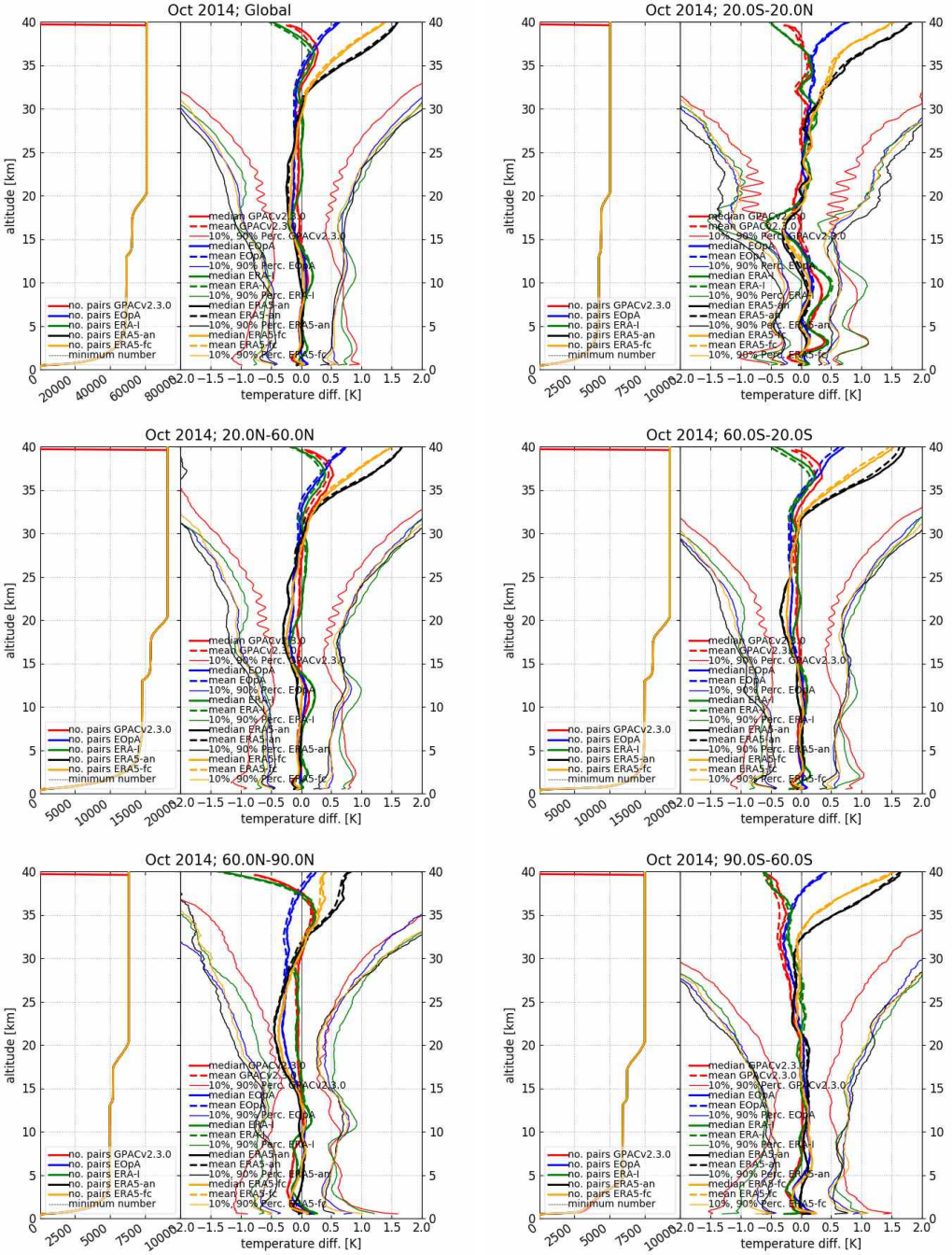

Figure B.18: *Temperature comparison for October 2014; top left panel: global; top right: tropics (20°S to 20°N); middle left: northern hemisphere mid-latitudes and subtropics (20°N to 60°N); middle right: southern hemisphere mid-latitudes and subtropics (20°S to 60°S); bottom left: northern hemisphere polar (60°N to 90°N); bottom right: southern hemisphere polar (60°S to 90°S)*

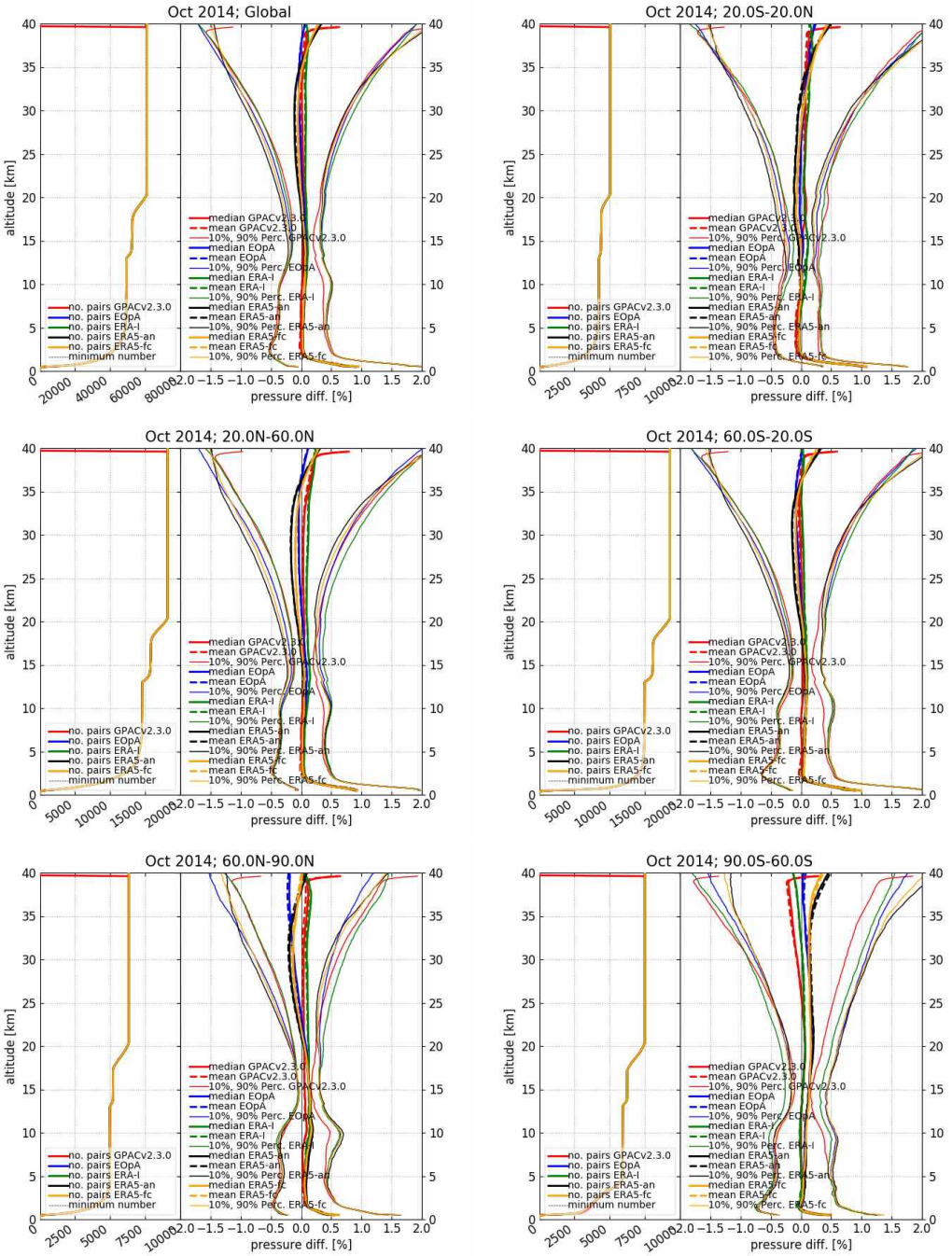

Figure B.19: *Pressure comparison for October 2014; top left panel: global; top right: tropics (20°S to 20°N); middle left: northern hemisphere mid-latitudes and subtropics (20°N to 60°N); middle right: southern hemisphere mid-latitudes and subtropics (20°S to 60°S); bottom left: northern hemisphere polar (60°N to 90°N); bottom right: southern hemisphere polar (60°S to 90°S)*

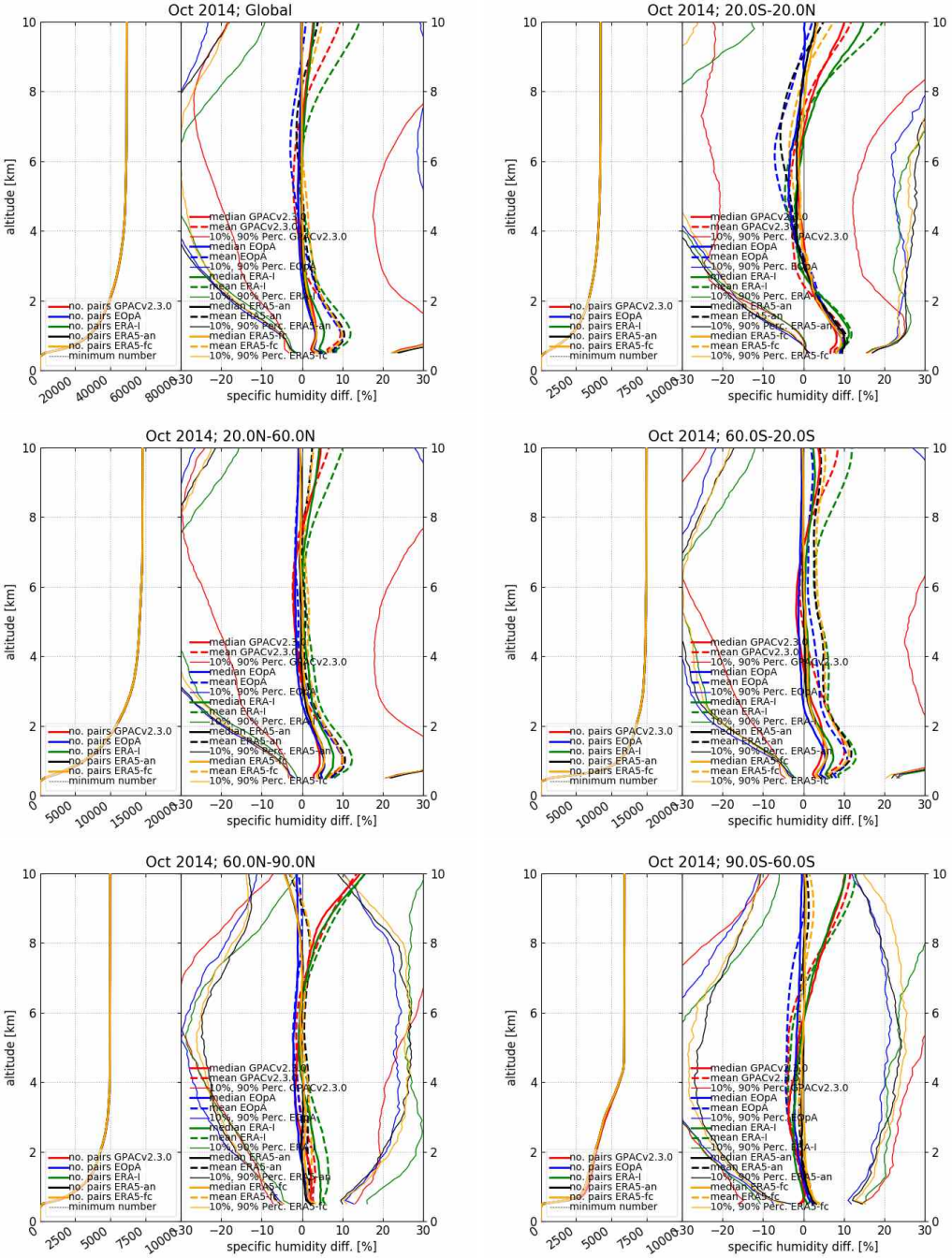

Figure B.20: *Specific humidity comparison for October 2014; top left panel: global; top right: tropics (20°S to 20°N); middle left: northern hemisphere mid-latitudes and subtropics (20°N to 60°N); middle right: southern hemisphere mid-latitudes and subtropics (20°S to 60°S); bottom left: northern hemisphere polar (60°N to 90°N); bottom right: southern hemisphere polar (60°S to 90°S)*